On the development of SuperSpec; a Fully Integrated On-chip Spectrometer for Far-infrared Astronomy

by

Peter Stuart Barry

A thesis submitted to Cardiff University
in Partial Fulfilment of the Requirements for the degree of
Doctor of Philosophy

2014
(Defended 16th Dec. 2014)

Declaration

This work has not been submitted in substance for any other degree or award at this or any other university or place of learning, nor is being submitted concurrently in candidature for any degree or other award.

Signature (candidate) *Date*

Statement One

This thesis is being submitted in partial fulfilment of the requirements for the degree of Ph.D.

Signature (candidate) *Date*

Statement Two

This thesis is the result of my own independent work/investigation, except where otherwise stated. Other sources are acknowledged by explicit references. The views expressed are my own.

Signature (candidate) *Date*

Statement Three

I hereby give consent for my thesis, if accepted, to be available online in the University's Open Access repository and for inter-library loan, and for the title and summary to be made available to outside organisations.

Signature (candidate) *Date*

Abstract

SuperSpec is an innovative, fully planar, compact spectrograph for mm/sub-mm astronomy. Its very small size, wide spectral bandwidth, and highly multiplexed detector readout will enable construction of powerful multi-object spectrometers for observations of galaxies at high redshift. SuperSpec is based on a superconducting filterbank consisting of a series of planar half-wavelength filters to divide up the incoming, broadband radiation. The power in each filter is coupled into a titanium nitride (TiN) lumped element Kinetic Inductance Detector (KID), facilitating the read out of a large number of filter elements with minimal cryogenic electronics. We present electromagnetic simulations of the various components that make up the first generation prototype device. We then present a characterisation of the performance of the TiN detectors and compare these to the standard Mattis-Bardeen prediction. We then demonstrate the operation of the filterbank at 250 GHz through a spectral characterisation made using a Martin-Puplett interferometer measuring a minimum filter bandwidth that corresponds to a spectral resolution of $\mathcal{R} = 700$. From blackbody measurements of the most responsive filter channels, we estimate a system noise equivalent power of $2 \times 10^{-15}\,\mathrm{WHz}^{-1/2}$.

Contents

List of Acronyms

KID - Kinetic inductance detector
LEKID - Lumped element KID
FIR - Far-infrared
CPW - Coplanar waveguide
RF - Radio frequency
IF - Intermediate frequency
HEB - Hot electron bolometer
SIS - Superconductor-insulator-superconductor
TES - Transition edge sensor
FTS - Fourier transform spectrometer
TLS - Two-level system
G-R - Generation-recombination
NEP - Noise equivalent power

Chapter 1

Introduction and Background

SuperSpec is a prototype on-chip spectrometer that will pave the way for the next generation of direct detection spectrometers operating in the far-infrared (FIR)/submillimetre (sub-mm) wavebands for both astronomy and terrestrial applications. In principle, the wavelength range accessible by a SuperSpec-type instrument spans the entire FIR/sub-mm spectral region. Situated within this range are a number of important spectral emission lines that provide one of the main probes into the physical processes and properties of the cold dusty regions of galaxies which are almost invisible at optical/NIR wavelengths. For local galactic studies, observations of the fine-structure cooling lines (e.g. CII, OI, NII) of various molecular and atomic species allows the study of the conditions in the large molecular clouds and reveal the earliest stages of star formation. For distant galaxies, identification of specific emission spectra provides a probe of how the earliest galaxies evolve into the local galaxies we see today.

As well as being a tool for studying the physical conditions of astronomical objects, spectroscopy is one of the most accurate methods of determining the redshift of an object. For example, a common technique in the FIR/sub-mm is to measure the low-medium J rotational transitions of carbon monoxide, for which $J = 1 \rightarrow 0$ corresponds to $\nu = 115$ GHz. By matching up the shifted measured spectra with the known spectra, an unambiguous value of the redshift can be determined. A fast and efficient method of determining redshift of the, now, thousands of galaxies that have been detected by the continuum survey instruments such as Herschel (Griffin et al. 2006; Eales et al. 2009) and BLAST (Devlin et al. 2004; Pascale et al. 2008), is required to build a picture of galaxy evolution throughout the history of the Universe.

The design of SuperSpec is based on a high-frequency superconducting integrated-filterbank. The lithographically patterned on-chip circuitry disperses the incoming radiation on a device size that is comparable to the observation wavelength, resulting

in a significant reduction in instrument size, complexity, and ultimately cost, when compared to the current state-of-the-art. Furthermore, the power in each spectral channel is coupled into a kinetic inductance detector (KID), owing to its simplistic design, complimentary planar architecture and multiplexing capabilities. The emergence and rapid improvement in performance of the KID for use in photon detection applications across a wide range of frequencies demonstrates the versatility and robustness of the technology.

Owing to the small size and relative ease of fabrication of a SuperSpec pixel, it is easy to imagine an instrument that consists of hundreds of spectrometer pixels filling the focal plane of a sub-mm telescope with the ability to map in both spatial and spectral domains simultaneously. The power of such an instrument for rapid blind redshift surveys is evident, and is now a realistic possibility given the numerous technological advancements over the past decade in areas such as high frequency superconducting circuits, electronic readout systems and fabrication processing and techniques. Most of the technology required to realise a SuperSpec type pixel can be borrowed from the increasingly prolific fields associated with superconducting microresonators. Since their advent in 2002 (Mazin et al. 2002; Day et al. 2003) for use as ultra-sensitive sub-mm photon detectors, planar superconducting microresonators have found use in a variety of applications including quantum information processing (Göppl et al. 2008; Graaf 2014), microwave characterisation of dielectric materials (Gao et al. 2009) and parametric amplification of RF signals (Eom et al. 2012; Mutus et al. 2013).

1.1 Sub-mm astronomy

Over the past decade, the study of the FIR/sub-mm spectral regions has undergone rapid expansion driven by the notable advances in the available instrumentation. With the wealth of data coming from the Herschel Space Observatory (HSO), regular observations with the Atacama Large mm/sub-mm Array (ALMA), along with numerous future observatories in the various stages of planning, the FIR/sub-mm is now set to play a key role in advancing the understanding of numerous astrophysical phenomena throughout the history of the Universe. The relative lack of progress of the field up to now can, in part, be attributed to a number of technological hurdles that need to be overcome when observing the sky at FIR/sub-mm wavelengths.

The most notable is the difficulty of ground-based observations. Water contained in the various layers of the Earth's atmosphere absorbs a prohibitive amount of the incoming signal. Observatories located at high altitude can overcome this to a certain

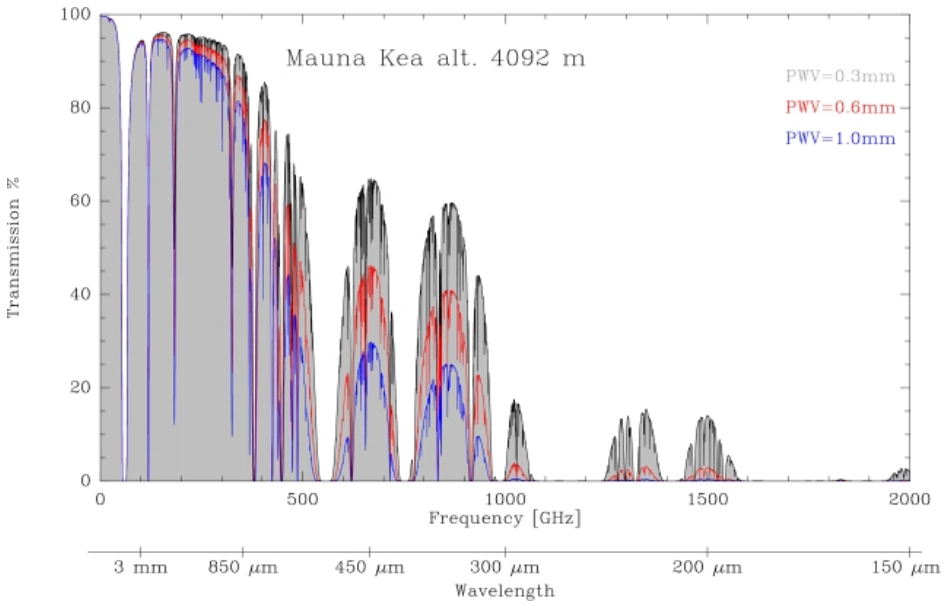

Figure 1.1: Atmospheric transmission measured at the Mauna Kea observatory in Hawaii.

extent, but even then, observations are restricted to only a small number of atmospheric windows (cf. Fig. 1.1). Even with the best (5-15% of the time depending on the time of year) weather at the best terrestrial locations, 30-40% of the signal is attenuated within the 350/450 μm windows. Clearly, astronomical observations of water, and other useful atomic or molecular species that fall outside of these windows, are completely inaccessible from the ground, necessitating stratospheric or space-based observatories.

Aside from the vast cost and complexity, space-based observatories suffer from limited angular resolution due to the practical constraints imposed on the instrument dimensions. The minimum resolvable angle of an optical system with an entrance aperture D is given by $\theta \sim \lambda/D$. Therefore, to obtain the detail seen in the Hubble images ($\lambda \sim 0.3$ μm, $D = 2.4$ m) at 350 μm would require a primary mirror diameter of ~ 3 km! This is clearly not feasible in a single-dish, with current ground-based and space-based observatories reaching 30 m (e.g. LMT, IRAM, CCAT) and 3.5 m (Herschel), respectively. However, interferometers employing aperture synthesis techniques are capable of such large baselines and are the only way to carry out high-resolution imaging at mm/sub-mm wavelengths. The most pertinent example is the ALMA interferometer, which has a maximum baseline of 16 km and operates across the entire sub-mm waveband.

Only relatively recently has the detector technology started to become competitive with other wavebands. The FIR/sub-mm lies in between the radio region, where co-

herent heterodyne technology is well established, and the optical wavebands, where incoherent direct detection has provided many of the remarkable images taken with the Hubble Space Telescope. This has resulted in the FIR/sub-mm adopting technology from both sides. However, the low sub-mm photon energy renders the incoherent semiconductor pair-breaking detectors ineffective, and the requirement on the low-noise mixers for coherent detection has only recently been achieved (Zmuidzinas et al. 1998). Heterodyne instruments are the standard choice for high-resolution spectroscopy and provide a compliment to the semiconductor bolometer for continuum imaging (Mauskopf et al. 1997), which has been the workhorse of sub-mm continuum observations for the past 20 years. However, while semiconductor bolometers are still in use today, the use of superconducting materials with the promise of increased sensitivities, are now forming the basis for most modern ultra-sensitive detector arrays for FIR/sub-mm astronomy.

Proof of how far detector technology has progressed is evidenced by the fact that detectors now reaching the stage where the sensitivity is limited by the FIR/sub-mm blackbody emission arising from the finite temperature of the telescope. Typical ambient temperatures of ground based telescopes are around 260 K whereas current space telescopes are usually passively cooled to about 90 K, but both generally overpower the astronomical signal. While there are a number of clever techniques to detect the weak signal in the presence of an overwhelming background, the additional inherent noise contribution bestows a limit on the attainable sensitivity of the telescope. For this reason, the next generation of space observatories will employ actively cooled (~ 5 K) primary apertures that will enable observations of the faintest sources.

1.2 Spectrograph Technology

1.2.1 Heterodyne Receivers

Heterodyne detection relies on the down-conversion of a high frequency (RF) sky signal to an intermediate frequency (IF) signal, whilst preserving both the amplitude and phase. Being at a significantly lower frequency, the IF signal is much more manageable enabling amplification and further processing. However, there is a penalty in the form of an unavoidable 'quantum noise' imposed by the uncertainty principle. This presents a fundamental limit on the sensitivity attainable by coherent receivers which is not present in direct detection architectures.

THz mixers have gradually improved over the past 25 years, with SIS technology

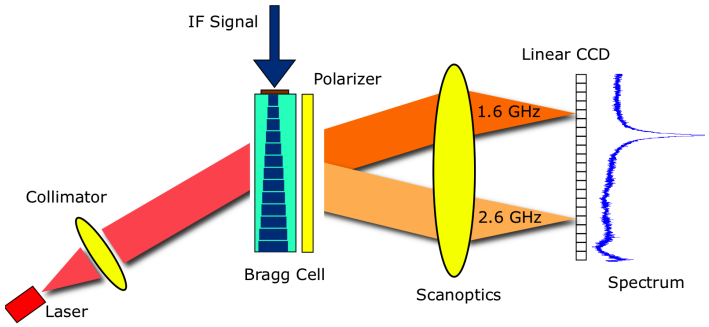

Figure 1.2: Schematic diagram of an acousto-optical spectrometer.

preferred for frequencies below 1 THz with noise temperatures only a few Kelvin above the quantum limit. Above 1 THz, HEB mixers are preferred due to the decrease in sensitivity in SIS devices above the gap frequency of the superconductor. For a detailed review of SIS and HEB mixer technology see Gundlach and Schicke (2000) and the references therein.

The main benefit of a heterodyne instrument is the ability to obtain high sensitivity, high spectral resolution (10^6) measurements. This powerful capability derives from the spectral information being extracted from the low frequency, amplified IF signal where there exists a number of techniques to analyse the data with the three most common being filterbank backbends, acousto-optical spectrometers (AOS) and autocorrelation spectrometers (AS).

A schematic of an AOS is shown in Fig. 1.2. A piezoelectric transducer converts the IF microwave signal into pressure waves in an optically active crystal (e.g. Bragg cell). The induced pressure waves modulate the refractive index throughout the cell effectively creating a diffraction grating that depends on the applied IF signal. A monochromatic optical laser incident on the Bragg cell passes through the crystal and is re-imaged onto a CCD or other photosensitive detector array. The AOS can be configured to have a relatively wide bandwidth but the attenuation of the Bragg cell limits the spectral resolution, $\mathcal{R}$, to a few 10^3 and so aren't appropriate for high spectral resolution measurements.

Whereas the AOS can be viewed as operating in the frequency domain, autocorrelation backends operate in the time, or lag domain, and the spectrum is retrieved using the well known Weiner-Khinchin theorem;

$$S_{xx}(f) = \int_{-\infty}^{\infty} R_{xx}(\tau) \cdot e^{-j2\pi f\tau} d\tau, \tag{1.1}$$

where R_{xx} is the auto-correlation function of the IF signal given by

$$R_{xx}(\tau) = \int_{-\infty}^{\infty} V(t+\tau) \cdot V^*(t). \tag{1.2}$$

Digital auto-correlation spectrometers implement this calculation on a digitized version the IF signal by passing multiple copies through a series of shift registers for the delay and digital logic multipliers and accumulators for the integrals. Analogue versions utilise finite length transmission lines to introduce the delay (Isaak et al. 1998) and are able to achieve higher bandwidths than their digital counterparts for the same power consumption.

Filterbank spectrometers are conceptually the most straightforward spectrometer back-end and consist of a number of discrete band-pass filters each tuned to different centre frequency (Tauber and Erickson 1991). The output of each filter is coupled to a power detector to obtain the intensity in each spectral bin. An advantage of the filterbank architecture is that the frequency sampling can be customised by manufacturing the band-pass filters to user-defined criteria. However, to obtain high spectral resolutions requires a large number of narrow-band filters. This increase in both size, complexity and cost meant that filter-bank backends were quickly succeeded by the alternatives mentioned above for most applications. However, contrary to operating at IF frequencies where the filter elements become fairly sizeable, SUPERSPEC proposes to implement a filterbank architecture at the signal frequency resulting in a significant reduction in size.

1.2.2 Direct Detection

In contrast to the coherent techniques that are sensitive to both the amplitude and phase of the incident photons, direct detection spectrometers are only sensitive to the signal intensity. Immediately, this gives the direct detection instruments a fundamental sensitivity advantage by not being susceptible to the quantum noise that appears in coherent receivers and therefore in principle, can operate at a sensitivity limited by the inherent fluctuations of the incident photons.

Generally, incoherent instruments consist of a dispersive element that divides up the incident radiation and a detector array to record the intensity in each spectral bin. The three examples discussed here are the diffraction grating, Fourier transform spectrometer (FTS) and Fabry-Perot interferometer. In the words of Zmuidzinas and Richards (2004), '*there is only one optimal approach that gives the best sensitivity: grating spectrometers or their equivalent*'. The reason being that for every photon absorbed its

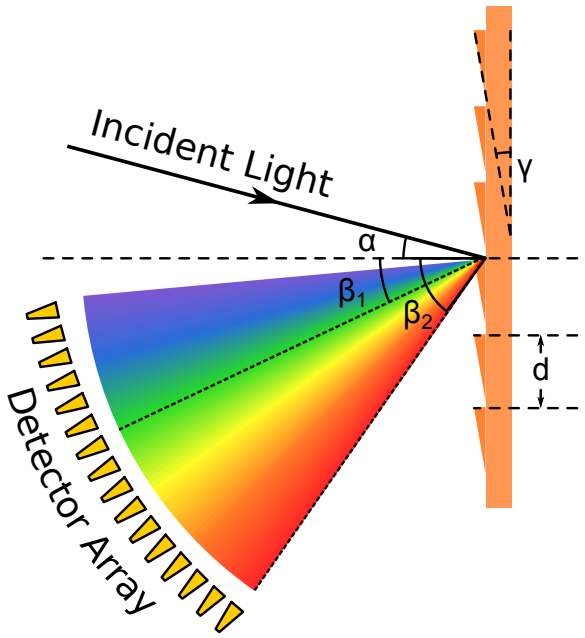

Figure 1.3: Schematic of a blazed reflective diffraction grating.

wavelength is also measured. This is not the case for a Fabry-Pérot, for example, where only photons that interfere constructively are detected. This degradation in sensitivity manifests itself in the increased scanning time required to obtain the spectrum. In principle therefore, gratings can provide exceptional sensitivity. However, considerations such as the size of the grating impose practical limits on the performance.

A schematic of a grating spectrometer is shown in Fig. 1.3. Simple geometric arguments lead to the well known grating equation for order m is given by,

$$m\lambda = d(\sin\alpha - \sin\beta), \tag{1.3}$$

where d is the groove or slit spacing. Eq. 1.3 applies to both transmission and reflection configurations, however for reflection β is taken as a negative. The angular dispersion of the grating is given by the derivative of Eq. 1.3,

$$\frac{d\beta}{d\lambda} = \frac{m}{d\cos\beta}, \tag{1.4}$$

and shows that the benefit of working in a high diffraction order. The chromatic resolving power can be calculated from

$$\mathcal{R} = \frac{\lambda}{\Delta\lambda}. \tag{1.5}$$

The efficiency of the grating is defined as the ratio of the incident power to the power

contained in the chosen order. To first order, the grating acts as a mirror, reflecting the incoming beam according to Snell's Law, resulting in a significant portion of the light is contained in the central $m = 0$ maximum which contains no spectroscopic value. In an attempt to increase the grating efficiency, it was suggested that a modification of diffraction element shape (e.g. angle) could lead to a shift the power from the central maximum into one of the diffraction orders. A grating of this type is known as a *blazed* grating and is characterised by the *blazing angle*, γ. The diffraction angle β depends only on d and λ, whereas the position of the diffraction envelope is determined by the blazing angle γ. By appropriate choice of the blazing angle, a significant amount of radiation can be concentrated in a given diffraction order, dramatically increasing the grating efficiency.

For a given blazing angle, the maximum resolution is obtained when $\alpha = \beta$, i.e. when the diffracted wave is retro-reflected back. This is known as the Littrow configuration as is used by most practical spectrometers. Echelle gratings are a sub-class of gratings that were designed to be achieve high spectral resolving power whilst remaining compact (Harrison 1949) by illuminating the grating at large angle of incidence. The blazing angle of an Echelle is relatively large and is characterised by its $R_{\#}$ value, where $R_{\#} = \tan\gamma$.

As an example, ZEUS (the redshift (**z**) and **E**arly **U**niverse **S**pectrometer) (Nikola et al. 2003; Stacey et al. 2007) was designed to study star formation at different redshift by measuring the relative abundances of the important spectral emission lines that fall within the 350 and 450 μm atmospheric windows. By using a 35 cm cryogenic cooled R-2 Echelle[1] grating operated in a near-Littrow configuration, the overlapping diffraction orders of $m = 4$ and $m = 5$ provide simultaneous coverage at 450 μm and 350 μm, respectively, with $\mathcal{R} = 550 - 1600$. The diffracted beams are then coupled to a 32 pixel linear array of neutron-transmutation doped (NTD) silicon bolometers with half the pixels tuned to each band. The grating is then rotated to cover the full 15% bandwidth of each atmospheric window (Hailey-Dunsheath 2009). ZEUS has undergone a number successful observing runs at the Caltech Sub-millimetre Observatory (CSO), providing the first observations of a number of spectral line from both nearby and distant galaxies. Most notably, the first detection of the ^{13}CO($6 \rightarrow 5$) line in a galaxy outside of the local group (Hailey-Dunsheath et al. 2008) and the observation of the 158 μm CII line from galaxies at $z = 1 - 2$.

Following on from the success of ZEUS, its successor ZEUS-II was commissioned and is expected to feature a guest instrument at the CSO. While ZEUS-II uses the same grating as ZEUS, the cryogenic, optical and detector architectures have all been upgraded

[1] R-2 corresponds to $\gamma = \arctan(2) = 63.43°$

to provide four-colour imaging capabilities by replacing the linear detector array with a number of TESs bolometer arrays, and operating the grating in additional diffraction orders (Ferkinhoff et al. 2010).

At longer wavelengths Z-Spec (Bradford et al. 2004), designed to cover the 1 mm (190-310 GHz) atmospheric window. Z-Spec uses a novel waveguide coupled Rowland grating (Bradford et al. 2002), operated in first order to obtain a large instantaneous bandwidth. Corrugated feed-horns couple light into a rectangular waveguide which serves as the input to the curved diffraction grating (WaFIRS[2]). As the light is confined to a 2D field distribution, the volume of the grating can be greatly reduced and naturally leads to the possibility of stacking WaFIRS modules to cover multiple spectral bands. The Z-Spec detector array consists of 160 individually mounted horn-coupled, SiN bolometers with NTD germanium thermistors with tuned back-shorts. With an operating temperature of 60 mK, the instrument achieves back-ground limited performance at the telescope. The scientific output from Z-Spec has been considerable with studies of local (Naylor 2008) and distant (Bradford et al. 2009) galaxies, and follow-up red-shift measurements of a number of gravitationally lensed Herschel sources (Lupu et al. 2012).

This practical limitation provides the motivation for other architectures such as the Fourier transform spectrometer (FTS). As discussed above, these are limited in their achievable sensitivity but do have significant practical advantages. The term FTS encompasses a number of different instrument configurations that all measure the interference pattern (interferogram) of the incoming light as a function of a delay introduced by translation mirror stage and the spectrum is obtained by a Fourier transform of the interferogram. An FTS in a Mach-Zender (Ade et al. 1999) configuration in the SPIRE instrument on the Herschel Space Observatory. The spectral resolution of an FTS is determined by the maximum optical path difference introduced by the mirror, and in Mach-Zender configuration allows for a factor of four higher resolution for a given mirror step. However, the attainable resolution is limited to ≈ 1000 for most practical configurations.

All spectrometers require some method of introducing a delay in time to the incident signal (Zmuidzinas and Richards 2004), and the larger the delay when compared to a wavelength, the higher the spectral resolution. For gratings, the limit on the spectral resolution is of order ~ 1000 determined by the physical size of the grating. For an FTS, the limitation is governed by the maximum attainable mirror retardation, which is usually limited by the mirror drive. For SuperSpec, the practical limitation on the spectral resolution will be governed by the number of detectors required to

[2]Waveguide Far InfraRed Spectrometer

sample the spectrum. For this reason, the baseline spectral resolution for the prototype device will be aimed toward reproducing similar performance as a typical grating spectrometer.

1.3 Thesis Outline

The aim of this thesis is provide a description of the evolution of SUPERSPEC from a conceptual designs to a demonstration of an operational filter-bank circuit. The outline of this thesis follows:

- Chapter 2 introduces the physics of superconducting microresonators, and outlines the current model that is used to understand and characterise the SUPERSPEC detectors.
- Chapter 3 presents a description of the development of the first generation prototype device, including initial simulation work that shaped the design of the filterbank, an inclusive description of the mask devices, finishing with details on the fabrication process.
- The discussion in Chapter 4 deals with the dark characterisation of the SUPERSPEC detectors, and compares them to the model outlined in Chapter 2.
- Chapter 5 presents the main result of this thesis; the demonstration and optical characterisation of the first operational filterbank operating at 190-310 GHz.
- Chapter 6 concludes the thesis with a discussion of on-going work and future plans.

1.4 Literature Contributions

A list of contributions to the literature that were written in the context of the work presented in this thesis.

P. S. Barry et al. (2012). "Electromagnetic design for SuperSpec: a lithographically-patterned millimetre-wave spectrograph". *Proceedings of SPIE* 8452. DOI: 10.1117/12.927089

E. Shirokoff et al. (2012). "MKID development for SuperSpec: an on-chip, mm-wave, filter-bank spectrometer". *Proceedings of SPIE* 8452. DOI: 10.1117/12.927070

E. Shirokoff et al. (2014). "Design and Performance of SuperSpec: An On-Chip, KID-Based, mm-Wavelength Spectrometer". *Journal of Low Temperature Physics*, p. 96. DOI: 10.1007/s10909-014-1122-8

S. Hailey-Dunsheath et al. (2014). "Optical Measurements of SuperSpec: A Millimeter-Wave On-Chip Spectrometer". *Journal of Low Temperature Physics*, p. 80. DOI: 10.1007/s10909-013-1068-2

Chapter 2

Physics of Kinetic Inductance Detectors

Over the past decade kinetic inductance detectors (KIDs) have emerged as an extremely promising candidate that fulfil many of the requirements of the next generation large format astronomical sub-mm cameras.

Fundamentally, a KID is a superconducting pair breaking detector and the principle of detection relies on the modification of the surface impedance of a superconducting film upon absorption of a photon with energy $h\nu > 2\Delta$. If the film is patterned into a high-Q resonator with resonant frequency ω_0 and quality factor Q_r, the change in surface impedance will modify both Q_r and ω_0, which can be sensed by monitoring the transmission of a microwave probe signal set to the resonant frequency. From a readout point of view, the resonator acts as a simple notch filter and only interacts with probe signal close the resonant frequency. A number of resonators, each with slightly different resonant frequency, can be patterned on the same film and probed with a comb of frequencies each set to a different resonant frequency. This inherent frequency domain multiplexing enables large pixel numbers to all be read out on a single set of coaxial cables providing a simple and cost effective solution to large format arrays.

KIDs can be classified into one of two categories determined by RF architecture; distributed or lumped element resonators (c.f. Fig. 2.1). A distributed resonator is the planar analogue of a microwave cavity and consists of a length of transmission line. The electric and magnetic field vary along the length of the resonator with the field pattern constrained by boundary conditions. The detector response is largest in regions of high current density, and consequently, a detector based on a distributed resonator requires an antenna to guide the radiation to the region of maximum re-

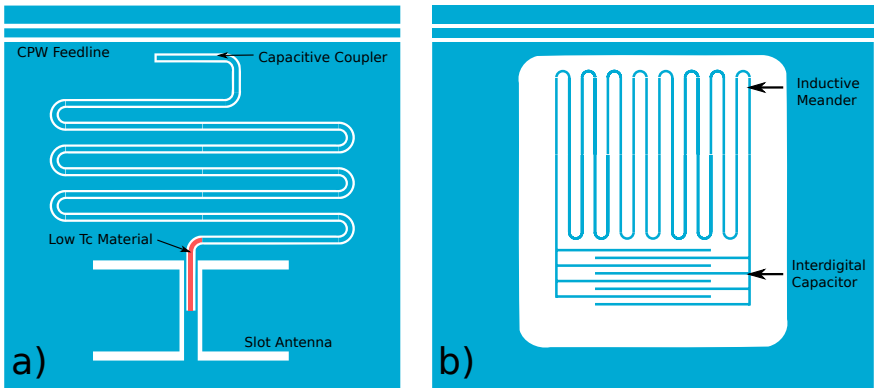

Figure 2.1: Schematic layout of a) a quarter wave distributed resonator coupled to a twin-slot antenna, and b) the conventional, inductively coupled LEKID design. Note for the distributed resonator usually requires a second, lower T_c material to form a quasiparticle trap.

sponse. Lumped element resonators on the other hand, consist of discrete circuit elements over which the fields are approximately constant, and instead of an antenna, the meandered inductor is usually designed into an efficient free-space absorber (Doyle 2008; McKenney et al. 2012). The lumped element resonator in its original form was conceived in 2008 (Doyle et al. 2008), and has since been iterated and optimised (e.g. Noroozian et al. (2012)) and is now used in a number of experiments and instruments (Monfardini et al. 2010; Swenson et al. 2012). A lumped element design is adopted for the SuperSpec detectors owing the simplicity and versatility of the lumped element resonator.

Traditionally, KIDs have been designed with a resonant frequency of 1-5 GHz. Working above 1 GHz requires the use of mixing stages that add a layer of complexity to the readout. The development of superconducting nitride materials such as titanium nitride (TiN) with large kinetic inductance has enabled the resonant frequency to be reduced down to the RF band (100 MHz) ($\omega_0 \propto L^{-1/2}$). Operating at this frequency alleviates the need for mixing stages and significantly reduces the complexity and per-pixel cost, crucial for the development of large format arrays (Swenson et al. 2012).

This goal of this chapter is to present an overview of the current theory of a lumped-element KID, and relies heavily on the pioneering work of a number of doctoral theses (Doyle 2008; Gao 2008; Mazin 2004) as well as the comprehensive review article by Zmuidzinas (2012).

2.1 Superconductivity and the Two Fluid Model

The two fluid model provides an intuitive way of understanding the electrodynamics of a superconductor. The main idea is that there are two parallel paths of charge carriers; one that carries current without dissipation and another that behaves like normal electrons in a metal. The former gives rise to the hallmark characteristic of zero dissipation at DC. The theory of Bardeen et al. (1957) showed that this population was made up of a bound state between two electrons mediated by the electron-phonon interaction, named Cooper pairs. The finite inertia of the Cooper pairs manifests itself as an internal inductance that results in a finite impedance at non-zero frequency. This effect is known as the kinetic inductance and is the principal mechanism behind a KID. The latter population are quasiparticle excitations from the Cooper pair condensate, and are characterised by number density n_{qp} and give rise to a non-zero dissipation at AC frequency.

The total current density can then be written as the sum of the currents in each path

$$\mathbf{j} = \mathbf{j}_n + \mathbf{j}_s, \tag{2.1}$$

where $\mathbf{j}_n$ can be derived using the classical Drude model for normal metals with

$$\sigma_n(\omega) = \frac{\sigma_0}{1 + j\omega\tau} \quad \sigma_0 = \frac{n_e q_e^2 \tau}{m_e}, \tag{2.2}$$

where τ is the characteristic scattering time. It is worth noting that the concept of kinetic inductance arises naturally in the Drude model as the imaginary term in Eq. 2.2. However, in most metals at room temperature and low frequency $\omega\tau \ll 1$ and the imaginary term can be ignored. It then follows that Eq. 2.2 results in Ohm's law. However, in clean samples at low temperatures τ can increase significantly and when working at high frequency, the imaginary part of the conductivity may become appreciable.

One of the first formulations of an expression for $\mathbf{j}_s$ is given by the phenomenological London model. The London equations can be written as,

$$\mathbf{j}_s(\mathbf{r}) = -\frac{1}{\mu_0 \lambda_L^2}\mathbf{A}(\mathbf{r}); \quad \lambda_L^2 = \frac{m_e}{\mu_0 n_s q_e^2}. \tag{2.3}$$

where λ_L is the London penetration depth, defined as the e^{-1} magnetic field decay length from the surface.

By writing the equations in this form and including the positional dependence, the

limitations of the London equations become apparent. Explicitly, at a given position the current density depends only on the vector potential at that same position. This implies that the fields are approximately constant over a characteristic distance of a Cooper pair. However, if the situation arises where the electric field varies appreciably over some defined length scale, then Eq. 2.3 should be replaced by an expression that takes into account the variation. Extending the theoretical work by Reuter and Sondheimer (1948) and experimentally by Chambers (1952) on the anomalous skin effect in normal metals, Pippard (1953) proposed a generalised expression for the current density,

$$\mathbf{j}_s(\mathbf{r}) = -\frac{3}{4\pi\mu_0\lambda_L^2\xi_0}\int \frac{\mathbf{r}[\mathbf{r}\cdot\mathbf{A}(\mathbf{r}')]e^{\frac{-r}{\xi}}}{r^4}d\mathbf{r}', \tag{2.4}$$

where ξ_0 is the material dependent Pippard coherence length and $\xi^{-1} = \xi_0^{-1} + \ell^{-1}$ is the effective coherence length which depends on impurity content. An expression for ξ_0 initially based upon an uncertainty principle argument was given as

$$\xi_0 = \gamma\frac{\hbar v_F}{k_B T_c}, \tag{2.5}$$

with γ being a constant of order unity. Guided by experimental data, Pippard found that $\gamma = 0.15$ resulted in a good fit, and later this form was confirmed using BCS theory with the theoretical value $\gamma = 0.18$.

It is instructive to determine the effect of Eq. 2.4 on the measured penetration depth λ, by examining the limiting cases of the local limit, $\xi \ll \lambda_L$ and the anomalous limit $\xi \gg \lambda_L$. The first case implies that $\mathbf{A}(\mathbf{r})$ is approximately constant within a region ξ, from which it can be shown that Eq. 2.4 reduces to,

$$\mathbf{j}_s = -\frac{1}{\mu_0\lambda^2}\mathbf{A}, \tag{2.6}$$

where

$$\lambda = \lambda_L\sqrt{\frac{\xi_0}{\xi}} = \lambda_L\sqrt{1+\frac{\xi_0}{\ell}}. \tag{2.7}$$

We can establish two further limiting cases given by Eq. 2.7 that are determined by the ratio ξ_0/ℓ. In the case of a high purity metal, $\ell \gg \xi_0$ and $\lambda \to \lambda_L$ we retrieve the London limit. If however $\ell \ll \xi_0$ caused by the presence of impurities then there is a factor of $\sqrt{\xi_0/\ell}$ increase in the measured penetration depth. This is known as the 'dirty' limit and is typically relevant for TiN films (Diener et al. 2012).

In the anomalous limit Faber and Pippard (1955) derived the relation

$$\lambda = \left[\frac{\sqrt{3}}{2\pi}\lambda_L^2\xi_0\right]^{\frac{1}{3}}, \tag{2.8}$$

for the measured penetration depth.

It should be noted that at the time of the inception both the local theory of London and the non-local extension of Pippard, a rigorous microscopic theory of superconductivity had not yet been formulated, and were purely based on observations. It wasn't until Bardeen et al. (1957) published their microscopic theory of superconductivity that a thorough understanding of the underlying physics began to emerge. That being said, many of the ideas put forward by Pippard on a phenomenological basis were theoretically verified within the BCS framework.

2.2 The Mattis-Bardeen Conductivity

Mattis and Bardeen (1958) were the first to develop a rigorous theory of high frequency superconducting electrodynamics that was consistent the microscopic theory of BCS. While the full theory is rather complex, in certain limits it can be simplified into a tractable form which has been shown to accurately model the behaviour of various superconducting materials over a wide range of temperatures and frequencies. The expression for the Mattis-Bardeen conductivity $\sigma = \sigma_1 - j\sigma_2$ that is valid in both the dirty and extreme anomalous limit are given by

$$\begin{aligned}\frac{\sigma_1}{\sigma_n} = &\frac{2}{\hbar\omega}\int_{\Delta}^{\infty}[f(E) - f(E+\hbar\omega)]\cdot g_1(E,\hbar\omega)dE \\ &+ \frac{1}{\hbar\omega}\int_{\min(\Delta-\hbar\omega,-\Delta)}^{-\Delta}[1-2f(E+\hbar\omega)]\cdot g_1(E,\hbar\omega)dE\end{aligned} \tag{2.9}$$

$$\frac{\sigma_2}{\sigma_n} = \frac{1}{\hbar\omega}\int_{\max(\Delta-\hbar\omega,-\Delta)}^{-\Delta}[1-2f(E+\hbar\omega)]\cdot g_2(E,\hbar\omega)dE, \tag{2.10}$$

where

$$\begin{aligned}g_1(E,\hbar\omega) &= \frac{E^2+\Delta^2+\hbar\omega E}{\sqrt{E^2-\Delta^2}\sqrt{(E+\hbar\omega)^2-\Delta^2}} \\ g_2(E,\hbar\omega) &= \frac{E^2+\Delta^2+\hbar\omega E}{\sqrt{\Delta^2-E^2}\sqrt{(E+\hbar\omega)^2-\Delta^2}}.\end{aligned}$$

The second integral in σ_1 is zero for $\hbar\omega < 2\Delta$. In the limit of $k_\mathrm{B}T, \hbar\omega \ll \Delta(T)$, Eqs. 2.9 and 2.10 take the analytical form (Barends 2009; Gao 2008)

$$\frac{\sigma_1}{\sigma_n} \approx \frac{4\Delta}{\hbar\omega} \exp\left(-\frac{\Delta}{k_\mathrm{B}T}\right) \sinh(\xi) K_0(\xi) \tag{2.11a}$$

$$\frac{\sigma_2}{\sigma_n} \approx \frac{\pi\Delta}{\hbar\omega} \left[1 - 2\exp\left(-\frac{\Delta}{k_\mathrm{B}T}\right) \exp(-\xi) I_0(\xi)\right], \tag{2.11b}$$

where $\xi = \hbar\omega/2k_\mathrm{B}T$. The validity of the approximation can be verified by taking aluminium as an example. At a typical operating temperature 250 mK and readout frequency of 1 GHz, $\Delta_\mathrm{Al} \sim 180\,\mu\mathrm{eV}$, $k_\mathrm{B}T \sim 21\,\mu\mathrm{eV}$ and $\hbar\omega \sim 0.7\,\mu\mathrm{eV}$.

The quasiparticle density can be calculated by integrating the product of the quasiparticle distribution function with the superconducting density of states,

$$n_{qp} = 4N_0 \int_0^\infty \frac{f(E)E}{\sqrt{E^2 - \Delta^2}} dE \approx 2N_0 \sqrt{2\pi k_\mathrm{B}T\Delta} \exp\left(-\frac{\Delta}{k_\mathrm{B}T}\right), \tag{2.12}$$

where the approximation is valid for a thermal distribution function $f(E)^{-1} = 1 + \exp(E/k_\mathrm{B}T)$ in the limit $k_\mathrm{B}T \ll \Delta$. By making the further approximation of

$$\Delta(T) \approx \Delta_0 \left[1 - \frac{n_{qp}}{2N_0\Delta(T)}\right], \tag{2.13}$$

where Δ_0 is the low temperature value, Gao et al. (2008a) show that the change in conductivity due to a change in quasiparticle density arising from a temperature change or external pair breaking are equivalent to within a factor of unity, and are given by

$$\frac{d\sigma_1}{dn_{qp}} = \sigma_N \frac{1}{N_0\hbar\omega} \sqrt{\frac{2\Delta_0}{\pi k_\mathrm{B}T}} \sinh(\xi) K_0(\xi) \tag{2.14a}$$

$$\frac{d\sigma_2}{dn_{qp}} = \sigma_N \frac{-\pi}{2N_0\hbar\omega} \left[1 + 2\sqrt{\frac{2\Delta_0}{\pi k_\mathrm{B}T}} \exp(-\xi) I_0(\xi)\right]. \tag{2.14b}$$

The equivalence between the response to thermal and external quasiparticles allows the responsivity to be estimated from a sweep of the bath temperature. Eqs. 2.14a and 2.14b are plotted in Fig. 2.2 for aluminium as a function of temperature and show that both expressions are a slowly varying function of temperature indicating that the complex conductivity is approximately linear with quasiparticle density - as it will be shown later $\delta f_r \propto \delta\sigma_2 \propto \delta n_{qp}$ - a useful relationship to remember.

From Fig. 2.2b it can be seen that there is a significant advantage to be had by operating at low readout frequency. The quasiparticle responsivity in the imaginary

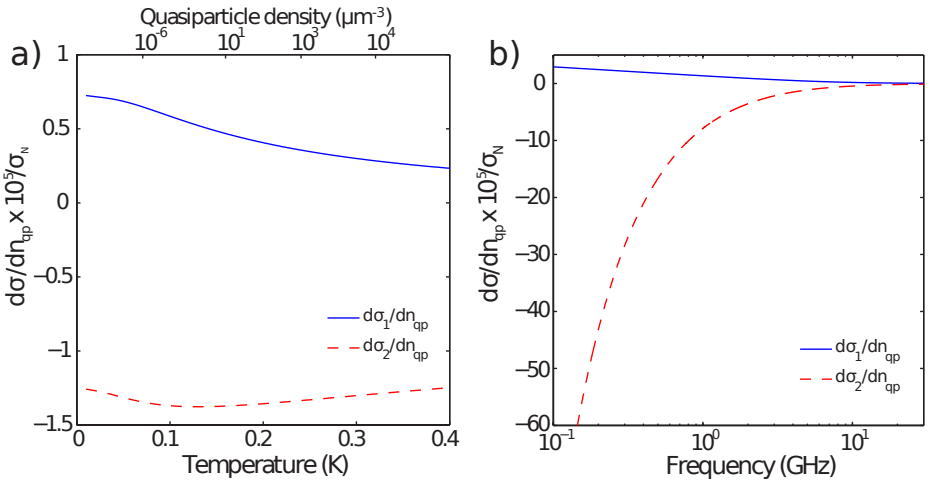

Figure 2.2: a) The response of the complex conductivity to a change in the thermal quasiparticle density, b) The response to a change in the quasiparticle density as a function of frequency. Figure adapted from Visser (2014).

component of the complex conductivity rapidly increases as the readout frequency is reduced. This is one of the main motives of the design of the SUPERSPEC detectors which is discussed in detail later.

2.3 Surface Impedance of a Superconducing Film

In most experiments it is not the complex conductivity that is directly observed but rather a measurement of the surface impedance of the superconducting film. Having derived expressions for the complex conductivity that is valid in both the local and anomalous limits, we now need to derive a relationship between the conductivity to the experimentally observable surface impedance. Generally the surface impedance of a material is complex and can be written as

$$Z_s = R_s + j\omega L_s = R_s + j\omega\mu_0\lambda_{\text{eff}}. \tag{2.15}$$

Thin Film

When the film thickness becomes comparable to the penetration depth, the current distribution within the film becomes approximately constant. In this case, the length scales of the superconductor can be constrained. Assuming diffuse reflection at the surface, an upper limit on the electronic mean free path becomes equal to the film thickness, and the coherence length is limited by the film thickness also. Therefore

given the above considerations, $\xi = \ell_{\text{mfp}} = t \ll \lambda$, the expressions derived assuming local electrodynamics are appropriate for thin films.

In the local limit, Matick (2000) shows that the surface impedance of a conductor with finite thickness can be expressed as

$$Z_s = \sqrt{\frac{j\omega\mu_0}{\sigma}} \coth t\sqrt{j\omega\mu_0\sigma} = \sqrt{\frac{j\omega\mu_0}{\sigma}} \coth \frac{t}{\lambda}\sqrt{1 + j\sigma_1/\sigma_2}, \tag{2.16}$$

with $\sigma = \sigma_1 - j\sigma_2$. The coth term is a correction factor that accounts for the ratio of the film thickness to the penetration depth. For a film thickness much smaller than λ, $\coth x \approx 1/x$ for small x, resulting in the simple relation,

$$Z_s = \frac{1}{(\sigma_1 - j\sigma_2)t} \rightarrow \boxed{\frac{\delta Z_s}{Z_s} = -\gamma\frac{\delta\sigma}{\sigma}}, \tag{2.17}$$

where $\gamma = 1$ for the thin-film case presented here. For thick films, it can be shown that $\gamma = 1/2, 1/3$ for the local and extreme anomalous limits, respectively (Zmuidzinas 2012). At temperature well below T_c, $\sigma_1 \ll \sigma_2$ and an expression for the surface resistance and inductance can be written from Eq. 2.15 as

$$R_s = \frac{\sigma_1}{(\sigma_1^2 + \sigma_2^2)t} \approx \frac{\sigma_1}{\sigma_2^2\, t}; \qquad L_s \approx \frac{1}{\omega\sigma_2 t} = \mu_0\lambda_{\text{eff}} \tag{2.18}$$

$$\rightarrow R_s = \omega L_s \frac{\sigma_1}{\sigma_2}. \tag{2.19}$$

Eq. 2.17 can be expanded about its zero temperature value where $Z_s(\omega, 0) = jX_s(\omega, 0)$ and $\sigma(\omega, 0) = -j\sigma_2(\omega, 0)$. To first order, the fractional perturbation in the real and imaginary parts of the surface impedance at low temperatures is given by

$$\frac{\delta R_s}{X_s(\omega, 0)} = \frac{\delta\sigma_1}{\sigma_2(\omega, 0)} \tag{2.20a}$$

$$\frac{\delta X_s}{X_s(\omega, 0)} = -\frac{\delta\sigma_2}{\sigma_2(\omega, 0)}. \tag{2.20b}$$

where $\delta Z_s(\omega, T) = Z_s(\omega, T) - Z_s(\omega, 0)$. To make the final step, Eqs. 2.20 can be related to a change in quasiparticle density by applying the expressions for the perturbation in the Mattis-Bardeen conductivity (Eqs. 2.14), leading to

$$\frac{\delta R_s}{X_s(\omega, 0)} = \frac{S_1(\omega)}{2\Delta_0 N_0}\delta n_{qp} \tag{2.21a}$$

$$\frac{\delta X_s}{X_s(\omega, 0)} = \frac{S_2(\omega)}{2\Delta_0 N_0}\delta n_{qp} \tag{2.21b}$$

$$S_1(\omega) = \frac{2}{\pi}\sqrt{\frac{2\Delta_0}{\pi k_B T}}\sinh(-\xi)K_0(\xi); \quad S_2(\omega) = 1 + \sqrt{\frac{2\Delta_0}{\pi k_B T}}\exp(-\xi)I_0(\xi). \tag{2.21c}$$

As is shown later, these expressions are directly related to the fractional change in the resonant frequency and dissipation in the resonator, and so are useful when analysing the data taken from a sweep in bath temperature to extract material properties. The ratio of the response in frequency direction to the dissipation response is given by

$$\beta(\omega) \triangleq \frac{\delta\sigma_2}{\delta\sigma_1} = \frac{|\delta X_s|}{\delta R_s} = \frac{S_2(\omega)}{S_1(\omega)}, \tag{2.22}$$

and as discussed previously (cf. Fig. 2.2b), increases rapidly at low readout frequency.

2.4 Quasiparticle Dynamics

The quasiparticle density defined in Eq. 2.12 is the statistical mean number at a given temperature. However, at finite temperature lattice vibrations are able to break Cooper pairs and cause the quasiparticle density to continuously fluctuate about that mean value. If a Cooper pair is broken in steady state, on average the quasiparticles recombine back into the ground state after a time τ_{qp}, known as the quasiparticle lifetime. The continuous generation and recombination of quasiparticles is the fundamental sensitivity limit for a KID.

In general, the rate equation for the quasiparticle number can be written in terms of a generation Γ_g rate and a recombination Γ_r rate,

$$\begin{aligned}\frac{dN_{qp}}{dt} &= 2\left(\Gamma_g - \Gamma_r\right) \\ &= 2\left(\Gamma_{th} + \Gamma_{ex}\right) - 2\Gamma_r,\end{aligned} \tag{2.23}$$

where Γ_{th} is the thermal generation rate and $\Gamma_{ex} = \Gamma_a + \Gamma_{opt}$ is the external generation rate and is made up of a terms originating from quasiparticle generation from the readout power and optical signal, respectively. The factor of two arises because quasiparticles are generated and recombine in pairs.

To relate the recombination rate with the quasiparticle lifetime, we use the expression derived by Kaplan et al. (1976) for the quasiparticle lifetime assuming a thermal

distribution function at low temperature, namely,

$$\begin{aligned}\tau_{qp} &= \frac{\tau_0}{\sqrt{\pi}}\left(\frac{k_\mathrm{B}T_c}{2\Delta}\right)^{5/2}\sqrt{\frac{T_c}{T}}\exp\left(\frac{\Delta}{k_\mathrm{B}T}\right) \\ &= \frac{\tau_0}{n_{qp}}\frac{N_0\left(k_\mathrm{B}T_c\right)^3}{2\Delta^2} \equiv R^{-1}n_{qp}^{-1},\end{aligned} \tag{2.24}$$

where $N_{qp} = n_{qp}V$ and R is the recombination constant with units of $\mathrm{m^3s^{-1}}$. While the inverse relationship between quasiparticle density and lifetime is derived assuming a thermal distribution, Visser et al. (2013) show that it the relation also holds for non-equilibrium distribution functions. The recombination rate is proportional to the number of combinations a Cooper pair can be formed from N_{qp}, which is given by[1] (Wilson and Prober 2004)

$$\Gamma_r = \frac{RVn_{qp}^2}{2}, \tag{2.25}$$

where R is the constant of proportionality.

The generation rate of thermal quasiparticles can be deduced by noting that in thermal equilibrium, the generation and recombination rates are equal, i.e., $\Gamma_{g,th} = \Gamma_r\left(n_{th}\right)$, where $n_{th}(T)$ can be calculated from Eq. 2.12. Inserting this condition into the rate equation (2.23) steady-state yields

$$\begin{aligned}n_{qp} &= \sqrt{n_{th}^2 + 2\Gamma_{g,ex}/RV} = \sqrt{n_{th}^2 + n_{opt}^2} \\ n_{opt}^2 &= \frac{N_0\tau_0\left(k_\mathrm{B}T_c\right)^3}{\Delta^3 V_L}\eta_e P_{opt},\end{aligned} \tag{2.26}$$

where $\Gamma_{g,ex} = \eta_e P_{opt}/\Delta$ has been used to derive the expression for n_{opt}. In the limit that $n_{opt} \gg n_{th}$ then the number of quasiparticles is determined by the radiation power and has a $P_{opt}^{1/2}$ dependence. It follows that a perturbation in the optical power δP_{opt} results in a quasiparticle responsivity that can be written as

$$\frac{\delta n_{qp}}{\delta P_{opt}} = \frac{\eta_e N_0\tau_0\left(k_\mathrm{B}T_c\right)^3}{4\Delta^3 V_L}P_{opt}^{-1/2} = \frac{\eta_e\tau_{qp}}{\Delta V_L}, \tag{2.27}$$

where Eq. 2.24 has been used to obtain the final equality. The power dependence in Eq. 2.27 has been experimentally verified in aluminium detectors (Janssen et al. 2013; Mauskopf et al. 2014), however, recently it has been shown that TiN resonators do not appear to follow the $P_{opt}^{-1/2}$ dependence and it has been suggested that the responsivity increases with loading (Bueno et al. 2014).

[1] Recall that ${}^nC_{r=2} = \frac{n!}{2!(n-2)!} = \frac{n(n-1)(n-2)(n-3)\ldots}{2(n-2)(n-3)\ldots} = \frac{n(n-1)}{2} \approx \frac{n^2}{2}$ for $n \gg 1$

As the temperature is decreased, the thermal quasiparticle population is expected to decrease exponentially with a corresponding increase in quasiparticle lifetime. It has been shown in a number of experiments on resonators made from various materials that there is a maximum limit on the measured quasiparticle lifetime, suggesting a residual non-thermal quasiparticle density. To account for this, Zmuidzinas (2012) suggests an empirical modification to Eq. 2.24, $\tau_{qp}^{-1} = \tau_{max}^{-1} + Rn_{qp}$.

It has been shown that proper control of stray light leaks into the detector package can have a significant effect on the residual quasiparticle density. For example, Baselmans et al. (2012) and Barends et al. (2011) demonstrated nearly an order of magnitude increase in quasiparticle lifetime by installing light-tight detector packaging and multi-stage filtering techniques.

2.5 Quasiparticle Number Fluctuations

The steady state condition assumed above was useful to calculate the average properties of the quasiparticle system. However, to calculate the contribution to the noise originating from the fluctuations in the quasiparticle density, a solution to the time dependent rate equation 2.23 is required. The rate expressions for recombination $\Gamma_r(t)$, thermal generation $\Gamma_g^{th}(t)$ along with generation from an external signal $\Gamma_{g_{ex}}(t)$ can be extended to include a time dependent perturbation as

$$\Gamma_r(t) = \langle \Gamma_r \rangle + \delta\Gamma_r(t) \tag{2.28a}$$

$$\Gamma_{g,th}(t) = \langle \Gamma_{th} \rangle + \delta\Gamma_g^{th}(t) \tag{2.28b}$$

$$\Gamma_{g,ex}(t) = \langle \Gamma_{ex} \rangle + \delta\Gamma_g^{ex}(t). \tag{2.28c}$$

If we make the assumptions that the perturbations for each process are independent and have a flat spectral density (white noise) that is governed by Poission statistics, then the spectral densities for the intrinsic perturbations are given by

$$S_r(f) = RVn_{qp}^2; \quad S_{g,th}(f) = RVn_{th}^2, \tag{2.29}$$

whereas it can be shown that the spectral density for the fluctuations in the incident photon stream that contribute to $\delta\Gamma_{g,ex}(t)$ are (Gao 2008)

$$S_{g,ex}(f) = \left(\frac{\eta_e}{\Delta V_L}\right)^2 \eta_{opt} P_{opt} h\nu \left(1 + \eta_{opt}\overline{n}_{ph}\right) \tag{2.30}$$

with $\overline{n}_{ph}^{-1} = [\exp(h\nu/k_{\mathrm{B}}T) - 1]$ is the mean photon occupation number and η_{opt} is the detector optical efficiency.

To convert the spectral density of the fluctuations in the rates into an equivalent number fluctuation we write the quasiparticle density as $n_{qp}(t) = \overline{n}_{qp} + \delta n_{qp}(t)$, where it can be shown that the rate equation for the time dependent fluctuations can be written as (Gao 2008; Zmuidzinas 2012)

$$\left(\frac{d}{dt} + R\overline{n}_{qp}\right)\delta n_{qp}(t) = \delta\Gamma_{th}(t) + \delta\Gamma_{ex}(t) - \delta\Gamma_{r}(t), \tag{2.31}$$

which can be solved in the Fourier domain as[2]

$$\delta n_{qp}(f) = \frac{\tau_{qp}}{1 + j2\pi f\tau_{qp}}\left[\delta\Gamma_{th}(f) + \delta\Gamma_{ex}(f) - \delta\Gamma_{r}(f)\right]. \tag{2.32}$$

The power spectral density for the fluctuations follows as

$$S_n(f) = |\delta n_{qp}(f)|^2 = \frac{\tau_{qp}^2}{1 + (2\pi f\tau_{qp})^2} S_{gr}(f) \tag{2.33}$$

where the cross terms vanish as the processes are assumed to be independent, and $S_{gr}(f) = S_{g,th}(f) + S_{g,ex}(f) + S_r(f)$.

If we assume that the film is not exposed to an external optical signal, then $S_{n,ex}(f) = 0$, $n_{qp} = n_{th}$ and we obtain for the single sided spectral density of the thermal generation and recombination of quasiparticles,

$$S_n(f) = \frac{4N_{qp}\tau_{qp}}{1 + (2\pi f\tau_{qp})^2}, \tag{2.34}$$

which is the same expression given by Wilson and Prober (2004). To calculate an equivalent NEP, Eq. 2.27 can be used to determine an equivalent optical power due to the fluctuations, which gives the standard result for the generation-recombination noise;

$$NEP_{gr} = \sqrt{S_n(f)}\left(\frac{dn_{qp}}{dP_{opt}}\right)^{-1} = \boxed{\frac{2\Delta}{\eta_e}\sqrt{\frac{N_{qp}}{\tau_{qp}}}\frac{1}{\sqrt{1 + (2\pi f\tau_{qp})^2}}}. \tag{2.35}$$

A similar analysis can be performed on the expression for the extrinsic fluctuation term (2.30) such that $S_{gr}(f) = S_{g,ex}(f)$, and we obtain

$$S_{ex}(f) = 2\left(\frac{\eta_e}{\Delta V_L}\right)^2 P_{opt}h\nu(1 + \overline{n}_{ph})\frac{\tau_{qp}^2}{1 + (2\pi f\tau_{qp})^2}, \tag{2.36}$$

[2]Recall the Fourier transform identities $\mathcal{F}(f(t) + g(t)) = F(f) + G(f)$ and $\mathcal{F}(f'(t)) = j2\pi fF(f)$

written as a single sided spectrum accounting for the factor of 2. The NEP is readily calculated with help from Eq. 2.35 as

$$NEP_{ph} = \boxed{\frac{2\eta_{opt} P_{opt} h\nu (1 + \eta_{opt} \overline{n}_{ph})}{\sqrt{1 + (2\pi f \tau_{qp})^2}}}, \tag{2.37}$$

which, for low readout frequency returns to the standard expression for inherent fluctuations from a thermal source (Boyd 1982).

The simplified approach is illustrative but does account for the physical situation. For example, quasiparticle recombination results in emission of phonon with energy $\Omega > 2\Delta$ that is able to break another Cooper pair. A more realistic situation is outlined by Wilson and Prober (2004) and uses the Rothwarf-Taylor (Rothwarf and Taylor 1967) equations to provide a more accurate description of the thin-film superconducting film. The result of their analysis is that the situation can arise where the spectrum can be described by two-time constants corresponding to the effective quasiparticle lifetime and the phonon lifetime within the film. For low temperature, where the recombination rate is slow compared to the characteristic phonon time-scales, the power spectral density of the fluctuations can be expressed by Eq. 2.34 with a modified lifetime τ_{eff} that depends on the phonon lifetime.

Recently, Visser et al. (2012b) made measurements of the noise power spectral density of Al half-wavelength resonators at 6 GHz that is well described with a two-term Lorentzian, rather than a single-term roll of as predicted in Eq. 2.34. They extend the RT model to account for an additional phonon bottle neck originating at the interface between the substrate and metallic sample holder, which results in an additional timescale. However, for the data in this thesis, the roll off in the spectral density is generally well described using a single-time constant Lorentzian.

2.6 Microwave Perspective

Having derived expressions for the response in surface impedance to a change in quasiparticle number, we are now in a position to relate that change to the observables accessible using a microwave resonator.

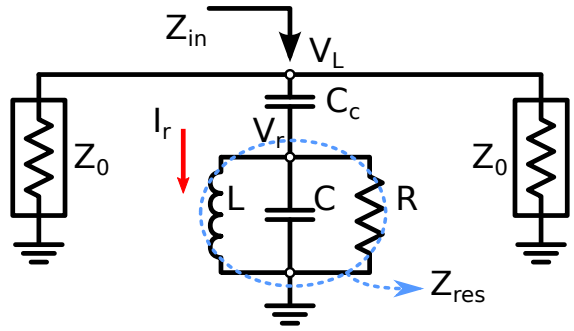

Figure 2.3: Circuit diagram of a parallel RLC circuit.

2.6.1 Resonator Impedance

The impedance of the parallel RLC circuit can be written as (Pozar 2011)

$$Z_{\text{res}} = \left[\frac{1}{R} + \frac{1}{j\omega L_r} + j\omega C_r\right]^{-1} \approx \frac{R}{1 + 2jQ_i x_0}, \tag{2.38}$$

where $x_0 = (\omega - \omega_0)/\omega_0$, $\omega_0^{-2} = L_r C_r$ and $Q_i = \omega_0 R C_r$. The addition of the coupling capacitor has the effect of loading the resonator and results in a shift in the resonant frequency to $\omega_r < \omega_0$. The impedance of the series combination is given by

$$\begin{aligned} Z_{\text{in}} &= Z_{cc} + Z_{\text{res}} \\ &= -\frac{j}{\omega C_c} + \frac{R}{1 + 2jQ_i x_0} \\ &= \frac{-\frac{j}{\omega C_c}(1 + 4Q_i^2 x_0^2) + R(1 - 2jQ_i x_0)}{1 + 4Q_i^2 x_0^2}. \end{aligned} \tag{2.39}$$

The definition of the resonant frequency is the frequency where $\Im(Z_{\text{in}}) = 0$, therefore

$$\begin{aligned} \Im\left(Z_{\text{in}}\right) &= -\frac{2Q_i R x_0(\omega_r) + \frac{1}{\omega_r C_c}(1 + 4Q_i^2 x_0^2(\omega_r))}{1 + 4Q_i^2 x_0^2(\omega_r)} = 0 \\ &\rightarrow 2Q_i R x_0(\omega_r) + \frac{1}{\omega_r C_c}(1 + 4Q_i^2 x_0^2(\omega_r)) = 0, \end{aligned} \tag{2.40}$$

which is of the form $ax^2 + bx + c$, with $a = 4Q_i^2/\omega_r C_c$, $b = 2Q_i R$ and $c = 1/\omega_r C_c$. The solution to the quadratic yields the fractional frequency shift at the loaded resonant

frequency ω_r,

$$x_0(\omega_r) = \frac{-2Q_iR \pm \sqrt{4Q_i^2R^2 - 16Q_i^2/\omega_r C_c}}{8Q_i^2/\omega_r C_c}$$
$$\approx \frac{-2Q_iR \pm 2Q_iR}{8Q_i^2/\omega_r C_c} = -\frac{R\omega_r C_c}{2Q_i} = -\frac{\omega_r C_c}{2\omega_0 C_r} \text{ or } 0 \tag{2.41}$$

where $Q_i = \omega_0 RC_r$ has been used. The approximation $R^2 \gg 4/(\omega C_c)^2$ has relative error of about 1 part in 10^6 for typical values. The second solution results in a very small shift from the natural resonant frequency, where the impedance of the RLC resonator is extremely large.

2.6.2 Coupling Quality Factor

As well as causing a shift in the resonant frequency, the addition of the coupling capacitor also acts as additional (but necessary) loss mechanism that reduces the overall quality factor of the system. An expression for the coupling quality factor at the resonant frequency ω_r can be derived from simple circuit theory and the general definition of the Q factor,

$$Q_c = \frac{\omega_r E_s}{P_{\text{diss}}}. \tag{2.42}$$

The total electrical energy in stored the resonator remains constant and transfers between the electric and magnetic field over an oscillation period. During the phase of oscillation where the energy is contained in the E field, the maximum energy can be written in terms of the peak voltage across the resonator capacitor as (Pozar 2011)

$$E_{\text{res}} = \frac{C_r|V_c|^2}{2}. \tag{2.43}$$

The power dissipated is the power that leaks out of the resonator and is absorbed in the terminations to be read out. The current through the series combination of the coupling capacitor and resonator impedance is simply $I = V_L/Z_{\text{in}} = V_c/Z_{\text{res}}$. From the standard definition of electric power dissipation,

$$P_{\text{diss}} = \frac{|I^2|}{2}\frac{Z_0}{2} = \left|\frac{V_c}{Z_{\text{res}}}\right|^2 \frac{Z_0}{4} = \frac{|V_c|^2\,\omega_r^2 C_c^2 Z_0}{4} \tag{2.44}$$

where $Z_{\text{res}}^{-1}(\omega_r) = \omega_r C_c$ has been used, and can be understood by recalling that the resonance condition states that reactance of the resonator must cancel with the reactance

of the coupling capacitor[3]. Combining the above equations results in

$$\boxed{Q_c = \frac{2C_r}{\omega_r Z_0 C_c^2}}, \tag{2.45}$$

which can be used to calculate the required coupling capacitance for a desired Q_c.

2.6.3 Resonator Transfer Function

Having determined the effect of the coupling capacitor, we can substitute $x_0 = x_r - \omega_r C_c/2\omega_0 C_r$ to obtain the forward transmission in terms of the modified resonant frequency and coupling quality factor. Recalling Eq. 2.39, for frequencies close to ω_r the resonator impedance becomes,

$$\begin{aligned} Z_{\text{in}} &= \frac{R + \frac{-j}{\omega C_c}\left(1 + 2jQ_i x_r - 2jQ_i/z_c Q_c\right)}{1 + 2jQ_i\left(x_r - \frac{1}{z_c Q_c}\right)} \\ &\approx \frac{\frac{1}{\omega C_c}\left(-j + 2Q_i x_r\right)}{1 + 2jQ_i\left(x_r - \frac{1}{z_c Q_c}\right)}, \end{aligned} \tag{2.46}$$

where $z_c = \omega_0 C_c Z_0$. The transfer function, $S_{21} = V_{\text{out}}/V_{\text{in}}$, can be calculated from (Pozar 2011)

$$S_{21}(\omega) = \frac{2}{2 + Z_0/Z_{\text{in}}}. \tag{2.47}$$

The expression for Z_0/Z_{in} can be simplified to

$$\begin{aligned} \frac{Z_0}{Z_{\text{in}}} &= \omega C_c Z_0 \cdot \frac{1 + 2jQ_i\left(x_r - \frac{1}{z_c Q_c}\right)}{2Q_i x_r - j} \\ &\approx \frac{2Q_i}{Q_c}\frac{1}{1 + 2Q_i x_r}, \end{aligned} \tag{2.48}$$

where the approximations $Q_i \gg 1$ and $Q_i x_r^2 \ll 1$ have been made. The first assumption is safe for all practical cases, whereas the second assumption holds at frequencies close to ω_r.

Finally, combining Eqs. 2.48 and 2.47, and recalling the definition of $Q_r^{-1} = Q_i^{-1} + Q_c^{-1}$

[3]Assuming that the loss in the resonator is small.

we arrive at the result,

$$\begin{aligned} S_{21}(\omega) &= \frac{Q_r/Q_i + 2Q_r x_r}{1 + 2Q_r x_r} \\ &= 1 - \frac{Q_r}{Q_c} \cdot \frac{1}{1 + 2jQ_r x_r}. \end{aligned} \tag{2.49}$$

which is the familiar Lorentzian lineshape centred around ω_r with half-width bandwidth $\omega_r/2Q_r$. This equation is used to fit resonator data to extract the resonator parameters.

2.6.4 Power Handling

The power dissipated in the resonator can be calculated by considering power conservation of a signal travelling along the feedline;

$$\frac{P_{\text{diss}}}{P_g} = 1 - |S_{21}|^2 - |S_{11}|^2. \tag{2.50}$$

For a shunt admittance to ground it is easily shown that $S_{11} = S_{21} - 1$. Recalling the expression for S_{21},

$$S_{21} = 1 - \frac{Q_r}{Q_c} \frac{1}{1 + 2jQ_r x}, \tag{2.51}$$

it is straightforward to derive the dissipated power as

$$P_{\text{diss}} = \frac{4Q_r^2}{Q_i Q_c} \frac{1}{1 + 4Q_r^2 x^2} \frac{P_g}{2}. \tag{2.52}$$

The first two terms on the right hand side of Eq. 2.52 are commonly termed the coupling efficiency χ_c and detuning efficiency χ_g. Both having a maximum value of unity, χ_c reaches a maximum for a critically coupled resonator with $Q_i = Q_c$ whereas χ_g is maximised at the resonant frequency. Under those conditions the power dissipation is simply $P_{\text{diss}} = P_g/2$. Recalling the definition of the quality factor $Q_i = \omega E/P_{\text{diss}}$, an expression for the energy stored within the resonator is given by

$$E_r = \frac{Q_i}{\omega} P_{\text{diss}} = \frac{2Q_r^2}{Q_c} \frac{1}{1 + 4Q_r^2 x^2} \frac{P_g}{\omega}, \tag{2.53}$$

which can be used to relate the internal power in the resonator to the power on the feedline,

$$P_{int} = \omega E_r = \frac{2Q_r^2}{Q_c} \frac{1}{1 + 4Q_r^2 x^2} P_g. \tag{2.54}$$

An estimate of the power handling of a resonator is important. Swenson et al. (2013) outline a set of equations that can be used to estimate the power handling of a resonator by assuming a current dependent kinetic inductance and expanding to second order. By assuming a kinetic inductance of the form $L_s(I) = L_s(0)[1 + I^2/I_*^2]$, where I_* is expected to be on the order of the critical current, an additional term in the resonator detuning arises and is related to the energy in the resonator by,

$$x_* = x_r - \delta x = x_r + \frac{E_r}{E_*}, \tag{2.55}$$

where E_* is expected to be on the order of the superconducting condensation energy of the inductor (Tinkham 2012),

$$E_c = \frac{N_0 \Delta^2 V_L}{2}. \tag{2.56}$$

Combining Eqs. 2.53 and 2.55,

$$x_* = x_r + \frac{2Q_r^2}{Q_c} \frac{1}{1 + 4Q_r^2 x^2} \frac{P_g}{\omega E_*}, \tag{2.57}$$

which can be parametrised as

$$y_* = y_r + \frac{a_c}{1 + 4y_*^2}; \quad a_c \equiv \frac{2Q_r^3}{Q_c} \frac{P_g}{\omega E_*}, \tag{2.58}$$

where a_c is defined as the non-linearity parameter and $y = xQ_r$ are the detuning measured in line-widths of the resonance[4]. The solution to Eq. 2.58 show that for values of $a_c > 0.77$, there are multiple solutions and the resonator exhibits the familiar switching behaviour at high powers (Visser et al. 2010).

It is useful to take rearrange Eq. 2.58 to solve the estimated bifurcation power on resonance,

$$P_g^c = \frac{a_c \omega N_0 \Delta^2 V_L Q_c}{4Q_r^3} \propto \omega\, T_c^2\, V_L\, Q_r^{-2} \tag{2.59}$$

with $a_c \approx 0.77$ and $Q_r = Q_c$ for the scaling relation. In Chapter 4 we compare this equation to experimental data and show it provides a good estimate the bifurcation power of the resonators for this thesis.

[4]Recall $Q_r = \omega_r/\Delta\omega$ where $\Delta\omega$ is the resonator line-width $\rightarrow Q_r x = (\omega - \omega_r)/\Delta\omega$ is the detuning in line-widths.

2.7 Resonator Response

As mentioned above, the detection mechanism of a KID relies on the modification of the complex surface impedance of a superconductor upon photon absorption. We derived an expression for the expected response of the superconducting film and in this section we relate the response to the observables, namely ω_r and Q_i.

$$\omega_r^2 = \frac{1}{L_t C_t} \tag{2.60}$$

where $L_t = L_k + L_g$ is the sum of the geometric and kinetic inductances[5], and C_t is the sum of the resonator and coupling capacitor. Assuming that only the kinetic inductance is modified upon photon absorption, the fractional change in the resonant frequency is given by,

$$x \equiv \frac{\delta\omega_r}{\omega_r} = -\frac{1}{2}\frac{\delta L_t}{L_t} = -\frac{\alpha_k}{2}\frac{\delta L_s}{L_s} = -\frac{\alpha_k}{2}\frac{\delta X_s}{X_s}, \tag{2.61}$$

where $X_s = \omega L_s$, and $\alpha_k = L_s/L_t$ is defined as the kinetic inductance fraction. Similar expressions can be derived for the response of the resonator in the dissipation/amplitude direction;

$$Q_i^{-1} = \frac{R}{\omega_r L} \rightarrow \delta Q_i^{-1} = \alpha_k \frac{\delta R}{X_s}. \tag{2.62}$$

Eqs. 2.61 and 2.62 relate the measured response of the resonator to a change in quasiparticle density through the Mattis-Bardeen expressions given in Eqs. 2.20, and result in

$$x = \frac{\delta\omega}{\omega_r} = -\alpha_k \frac{S_2(\omega)}{4\Delta_0 N_0}\delta n_{qp} \tag{2.63a}$$

$$Q_i^{-1} = \alpha_k \frac{S_1(\omega)}{2\Delta_0 N_0} n_{qp} \rightarrow \delta Q_i^{-1} = \alpha_k \frac{S_1(\omega)}{2\Delta_0 N_0}\delta n_{qp}. \tag{2.63b}$$

The above equations are routinely used to fit to temperature sweep data and extract a value for α and Δ. The quasiparticle responsivity to optical power (Eq. 2.27) can be used to calculate the resonator responsivity in both quadratures as

$$R_x \triangleq -\frac{dx}{dP_{opt}} = \frac{\alpha_k S_2(\omega)\eta_e}{4N_0\Delta_0^2 V_L}\tau_{qp} = \frac{\beta(\omega)\eta_e\tau_{qp}}{2\Delta_0 V_L n_{qp} Q_i} \tag{2.64a}$$

$$R_{Q_i^{-1}} = \frac{dQ_i^{-1}}{dP_{opt}} = \frac{\alpha_k S_1(\omega)\eta_e}{2N_0\Delta_0^2 V_L}\tau_{qp} = \frac{\eta_e\tau_{qp}}{\Delta_0 V_L n_{qp} Q_i}. \tag{2.64b}$$

[5]Note that there is also a magnetic inductance term that is usually negligible (Porch et al. 2005).

Note that the ratio of the responsivity in the frequency direction is a factor of $\beta(\omega)/2$ larger than in the dissipation direction. Assuming that the quasiparticle density is dominated by optically generated quasiparticles, we can substitute Eq. 2.24 for τ_{qp} as a function of optical power to obtain

$$R_x = \frac{\alpha_k S_2(\omega)\eta_e}{4N_0\Delta_0^2 V_L}\left[\frac{2R\eta_e P_{opt}}{\Delta_0 V_L}\right]^{-1/2}, \tag{2.65}$$

which upon inserting R from Eq. 2.24 and simplifying can be written as

$$R_x \approx \frac{\alpha_k S_2(\omega,T)}{4\Delta_0 V_L}\sqrt{\frac{\eta_e\tau_0}{32N_0}}\left(\frac{P_{opt}}{V_L}\right)^{-1/2} \propto T_c^{-1/2}V_L^{-1/2}T^{-1/2}. \tag{2.66}$$

As mentioned earlier, to account for the observed saturation in quasiparticle lifetime at low temperatures, Zmuidzinas (2012) proposes modifying the expression for the quasiparticle lifetime to

$$\tau_{qp} = \frac{\tau_{\max}}{1+n_{qp}/n^*} \approx \tau_{\max}\left[1+\frac{2\eta_e\tau_{\max}P_{opt}}{n^*\Delta_0 V_L}\right]^{-1/2}, \tag{2.67}$$

where the approximation assumes a negligible thermal quasiparticle contribution. Combining with Eq. 2.64b results in

$$R_x = \frac{\alpha_k S_2(\omega)\eta_e}{4N_0\Delta_0^2 V_L}\left[\frac{1}{\tau_{\max}^2}+\frac{2\eta_e P_{opt}}{\tau_{\max}n^*\Delta_0 V_L}\right]^{-1/2}, \tag{2.68}$$

which in the limit that $\tau_{\max}^{-1} \to 0$, returns to Eq. 2.65 as expected. Eq. 2.68 is plotted in Fig. 2.4 for typical parameters of aluminium (blue and green) and titanium nitride (red, purple). The plateau at low powers is set by the value of $\tau_{\max}$. Values of $\tau_{\max} \approx 1$ ms are typical for aluminium, and slightly lower for titanium nitride $\tau_{\max} \approx 100\,\mu$s. As the power increases, the number of optical quasiparticles dominates and the $P_{opt}^{-1/2}$ relationship is recovered.

Eq. 2.68 is used in Chapter 4 to estimate the power absorbed through the spectrometer from a blackbody measurement.

2.7.1 Noise Roll Off

To derive the observed roll off in the noise, it is necessary to include a model for the dynamic response of the resonator that includes the ring-down time of the resonator. Gao (2008) derives an expression for the dynamic response and shows that for zero detuning, the resonator behaves as a single-pole low pass filter with transfer function

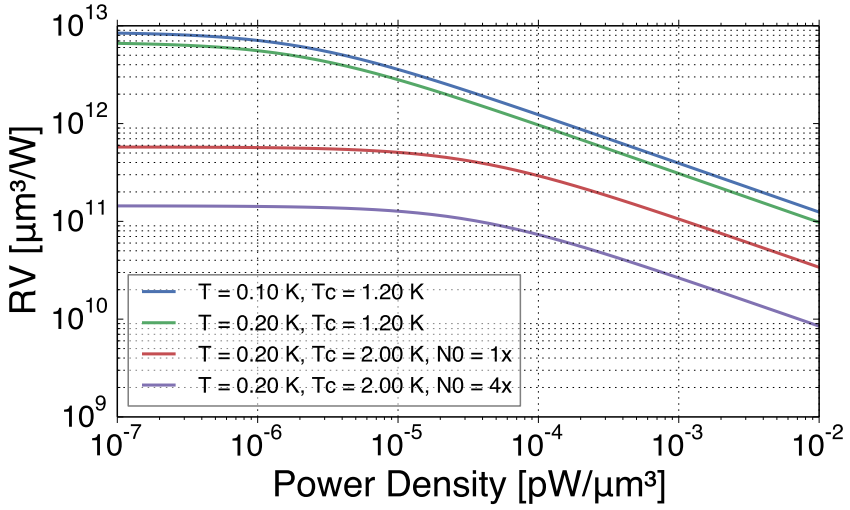

Figure 2.4: Eq. 2.68 plotted for parameters typical of aluminium and titanium nitride films. See text for details.

given by

$$\zeta = \frac{1}{1 + jf/\Delta f_{hw}}; \qquad \Delta f_{hw} = \frac{\omega_r}{4\pi Q_r}, \tag{2.69}$$

where Δf_{hw} is the half-width bandwidth of the resonator. This equation should be added to the expression for the resonator responsivity to account for the fact that the resonator can't respond to fluctuations that are faster that the ring-down time of the resonator which is defined as

$$|\zeta|^2 = \frac{1}{1 + \omega^2 \tau_{res}^2} \rightarrow \tau_{res} = \frac{Q_r}{\pi f_r}. \tag{2.70}$$

2.8 Sensitivity

2.8.1 Amplifier Noise

The power of the RF tone required to probe the resonances is usually somewhere between -70 - -130 dBm (100 pW - 1 fW). Comparing this to the thermal noise power generated at room temperature, $P_{300\mathrm{K}} \sim k_B T \Delta\nu \approx 1$ pW in a 1 GHz bandwidth, shows that measuring a resonator quickly becomes impractical. To overcome this, a low noise cryogenic amplifier located at 4 K boosts the RF signal to a level that, if necessary, can be further amplified by room temperature electronics. The total noise temperature of an amplifier chain can be calculated using the Friis formula,

$$T_{\mathrm{tot}} = T_{\mathrm{A1}} + \frac{T_{\mathrm{A2}}}{G_1} + \frac{T_{\mathrm{A2}} T_{\mathrm{A3}}}{G_1 G_2} + \ldots, \tag{2.71}$$

which highlights the requirement of a low noise, high gain amplifier as the first stage. The SiGe cryogenic LNAs (Weinreb et al. 2007) used in this thesis have a gain of 30-40 dB and quoted noise temperature of 5 K at an operating temperature of 20 K. At lower temperatures, the noise temperature is expected to decrease, so good heatsinking of the amplifier stage is essential.

To calculate the expected measured amplifier noise with a given T_a, we use the standard expression for the voltage noise originating from a resistor at temperature T_a,

$$e_V^2 = 4k_B T_a R \qquad \left[\mathrm{V}^2/\mathrm{Hz}\right]. \tag{2.72}$$

The equivalent fluctuation in the resonator detuning, $x = (f - f_r)/f_r$, can be expressed as

$$S_{x,\,\mathrm{amp}} = e_{V,\,\mathrm{amp}}^2 \cdot \left(\frac{dx}{dV_{\mathrm{out}}}\right)^2, \tag{2.73}$$

and along with the definition of the forward scattering parameter, $V_{\mathrm{out}} = S_{21} V_{\mathrm{in}}$ we have,

$$\frac{dV_{\mathrm{out}}}{dx} = V_{\mathrm{in}} \frac{dS_{21}}{dx}. \tag{2.74}$$

Recalling the definition of the transfer function,

$$S_{21} = 1 - \frac{Q_r}{Q_c} \cdot \frac{1}{1 + 2jQ_r x}, \tag{2.75}$$

it can be shown, using the notation of Zmuidzinas (2012), that the change in S_{21} in the frequency direction is

$$\frac{dS_{21}}{dx} = \frac{Q_i}{2} \chi_c \chi_g e^{-2j\phi_g} \overset{Q_r x \ll 1}{\approx} \frac{2Q_r^2}{Q_c}. \tag{2.76}$$

Recall that the product $Q_r x$ can be viewed as the detuning expressed as the number the resonator linewidths, so the approximation holds as long as the generator tone is close to the resonant frequency. Combining the above equations it is straightforward to derive,

$$S_{x,\,\mathrm{amp}} = e_{V,\,\mathrm{amp}}^2 \cdot \left(\frac{1}{V_{\mathrm{in}}} \frac{Q_c}{2Q_r^2}\right)^2 = 4k_{\mathrm{B}} T_{\mathrm{n}} Z_0 \cdot \frac{Q_c^2}{4Q_r^4 V_{\mathrm{in}}^2}$$

$$\overset{Q_r = Q_c}{=} \frac{k_{\mathrm{B}} T_{\mathrm{n}}}{Q_r^2 P_g} \tag{2.77}$$

$$\overset{Q_i = Q_c}{=} \frac{k_{\mathrm{B}} T_{\mathrm{n}}}{2Q_r P_g} \tag{2.78}$$

where $P_g = V_{\mathrm{in}}^2 / Z_0$. For a coupling-$Q$ limited resonator driven just below bifurcation

where $P_g^{\max} \propto Q_r^{-2}$ (Eq. 2.59), the amplifier noise should be independent of Q_r.

As before, we use Eq. 2.64b to convert the PSD of amplifier fluctuations to a noise equivalent power yielding,

$$NEP_{x,\mathrm{amp}} = \frac{\sqrt{S_{x,\mathrm{amp}}}}{R_x} = \frac{Q_c Q_i}{Q_r^2} \frac{2\Delta_0 N_{qp}}{\beta(\omega)\eta_e \tau_{qp}} \sqrt{\frac{k_\mathrm{B} T_a}{P_g}}. \tag{2.79}$$

A similar expression can be derived for the fluctuations in the dissipation direction; the result is equivalent except for the factor of β in the denominator. For most materials $\beta > 1$ suggesting an inherent advantage of frequency readout. However, excess frequency noise due to TLS fluctuations is routinely observed to limit the sensitivity in the frequency direction.

2.8.2 Two-Level Systems

Two level systems were identified very early in the development of KIDs as being a potential issue for KID performance. In basic terms, the effect of TLSs is a fluctuation of the complex dielectric constant of the material. TLSs arise due to the amorphous structure of dielectric materials. The random disorder in the dielectric gives rise to a complex potential energy distribution that allows groups of atoms or molecules to occupy and transition between multiple potential energy minima. The atomic electric dipole enables the atoms to couple to external fields and contribute to the dielectric constant of the material. The slight change in energy resulting from a transition from one minima to another leads to a corresponding change in the dielectric constant.

As the TLS couple to the electric field, the effect on a KID is to modify the capacitance and consequently, the resonant frequency of the resonator. Furthermore, coupling to an external field can induce transitions that extract energy from the external field. From the resonator point of view, this constitutes an additional inherent loss to which we can attribute a corresponding Q. In early measurements of resonators, it was found that the Q_i has a significant power dependence which is now understood as the saturation of the TLS into a single state. An expression for the TLS contribution to the loss is given by (Gao et al. 2008b)

$$Q_{i,\mathrm{TLS}}^{-1} = F_{\mathrm{TLS}} \delta_0 \tanh(\xi) \frac{1}{\sqrt{1 + |P_{\mathrm{int}}/P_c|^2}}, \tag{2.80}$$

where $\xi = \hbar\omega/2k_\mathrm{B}T$ as before, δ_0 is the intrinsic loss tangent and F_{TLS} is a geometric filling factor defined as the ratio of the electric contained with the TLS hosting material

to the total electric field. P_c is a characteristic power associated with saturation of the TLS.

Another distinctive feature that is regularly observed is the anomalous fractional frequency shift as a function of temperature. For resonators with a significant TLS contribution, the resonant frequency is observed to increase as the temperature increases, contrary to the prediction of Mattis-Bardeen. The expression for the fractional frequency shift due to TLS is given by

$$x_{\mathrm{TLS}} = \frac{F_{\mathrm{TLS}}\delta_0}{\pi}\left[\mathrm{Re}\Psi\left(0.5+\frac{\xi}{j\pi}\right)-\ln\left(2\xi\right)\right]\frac{1}{\sqrt{1+|P_{\mathrm{int}}/P_c|^2}}, \tag{2.81}$$

where Ψ is the complex digamma function and for typical measurement parameters for KIDs, is essentially constant.

TLS Noise

The contribution of TLS also impacts on the device sensitivity. Numerous experiments have reported an excess device noise that has been attributed to TLS. Ultimately, the fluctuation due to a change in capacitance is indistinguishable from a modification of the inductance upon photon absorption. However noise originating from TLS has been observed to have a number of characteristics that are contained in the semiempirical model of Gao et al. (2008b).

Firstly, the noise appears almost exclusively in the frequency direction, with very little contribution in the dissipation direction except when operating at single-photon readout powers (Neill et al. 2013). The shape of the noise generally is observed to have a $f^{-\alpha}$ slope where $\alpha = 0.5$. The low frequency slope indicates that there is a certain amount of correlation between the TLS which can be understood if the transition of one TLS modifies the energy landscape of neighbouring TLS.

The noise level is observed to decrease with increasing readout power due to the saturation of the TLSs. There is however a limit of the maximum readout power set by the onset of non-linearities in the resonator. The $P_{\mathrm{int}}^{-1/2}$ relation has been extensively measured in various experiments on a number of geometries. The temperature dependence is generally observed to follow T^{-t} with $t = 1.5 - 2$.

A general expression for the spectral density of the fractional frequency fluctuations that capture the observed dependencies is derived by Gao (2008). The specific form is

geometry and material dependent but a useful scaling relation can be derived as

$$S_{x,\mathrm{TLS}} \propto T^{-t} P_{\mathrm{int}}^{-1/2}. \tag{2.82}$$

The TLS contribution to the NEP can be written as

$$\mathrm{NEP}_{x,\mathrm{TLS}} = \frac{\sqrt{2S_{\mathrm{TLS}}}}{R_x} = \frac{2\sqrt{2}\Delta_0 N_{qp} Q_i}{\beta \eta_e \tau_{qp}} \sqrt{S_{\mathrm{TLS}}}. \tag{2.83}$$

There are a number of tactics that can be used to reduce the TLS contribution to the noise and loss. It has been shown that even on a crystalline substrate such as silicon or sapphire, there exists a population of TLSs located at the surfaces of the dielectric and metal layers and usually consist of an oxide layer. Under normal conditions stoichiometric titanium nitride has the advantage of not developing a natural oxide, whereas the surface of the substrate can be prepared to remove any native oxide before depositing the film.

Modifying the geometry of the capacitor to reduce F_{TLS}. For an interdigital capacitor, this could involve decreasing the size of the electrodes, increasing the electrode spacing or making the capacitor metal thicker. It has also been shown by Barends et al. (2009) that removal of the substrate layer in regions of high electric field produces a significant reduction in the TLS noise.

2.9 Summary

The goal of any detector is to reach the level sensitivity below which the detector noise is limited by inherent photon noise of the incoming signal. For ground-based/terrestrial instruments, this is usually fairly high and is determined background loading. For space-based applications, the requirements are more demanding as the background power is much less, usually around an ambient temperature between 50-90 K. For the next generation of space observatories, the primary mirror will be actively cooled placing further constraints on the detector performance. For a spectrometer, the demands are further increased, as there is $\mathcal{R}^{-1}$ times less power on the detector than for an imaging detector.

For a KID, the fundamental sensitivity limit is determined by the generation and recombination of quasiparticles in the superconducting film. This limit has been reached by a number of groups (Visser et al. 2012a; Mauskopf et al. 2014). Practically, excess noise attributed to the TLS fluctuations in the dielectric limits the sensitivity of a

KID. The shape of the TLS noise typically has an $1/f$ shape spectrum, resulting in a degradation in performance at low modulation frequency. This has a significant impact on astronomical instruments on telescopes that generally operate at low modulation frequency. For this reason, the understanding of TLS effects has been an intense area of research, with significant progress being made.

The main attraction of KIDs in place of other technologies, is the relative ease of expanding to large format arrays. This is particularly attractive for SUPERSPEC, as the long term goal is to field an instrument that contains a large number of spectrometer pixels filling the focal plane of a telescope. The number of detectors required for each pixel is of the same order as the required spectral resolution. For example, a 100-pixel array of $\mathcal{R} = 1000$ spectrometers, requires at least 100k pixels - a number that is predicted to be achievable using KID technology within the next decade (Zmuidzinas 2012).

Chapter 3

Evolution of SuperSpec

The concept of an on-chip spectrometer is shown schematically in Fig. 3.1. A broadband antenna at the spectrometer input couples incident radiation onto a superconducting planar transmission line. Placed along the feedline are a number of half-wavelength resonant filters that form the filterbank, with each filter extracting a narrow spectral band $\Delta\nu$ centred on the resonant frequency ν_0.

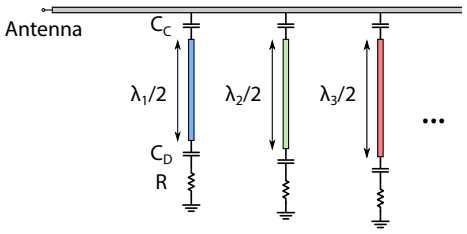

Figure 3.1: Simplified schematic of a filter bank spectrometer.

The power contained in each filter is then coupled into a detector. In this thesis we explore the possibility of detecting the absorbed power by directly measuring the change in kinetic inductance due to the change in quasiparticle density in the absorber material by monitoring the resonant frequency of a low frequency lumped element resonant circuit (Doyle et al. 2007) connected to the filter bank element.

The goal of this chapter is to provide a brief history and description of the development and realisation of the first prototype SuperSpec device.

3.1 Initial Filterbank Designs and Simulations

The filter circuit can either be implemented as a lumped element filter or as a distributed $\lambda/2$ resonator. For a lumped element implementation the dimensions of the components would have to be much smaller than λ in order to act as lumped elements and would be extremely sensitive to manufacturing tolerance error. Therefore we choose to pursue an implementation based on distributed resonators for the filterbank elements.

Initially there were two design concepts proposed. Both built in microstrip, the fundamental difference between them was the method for terminating the filterbank.

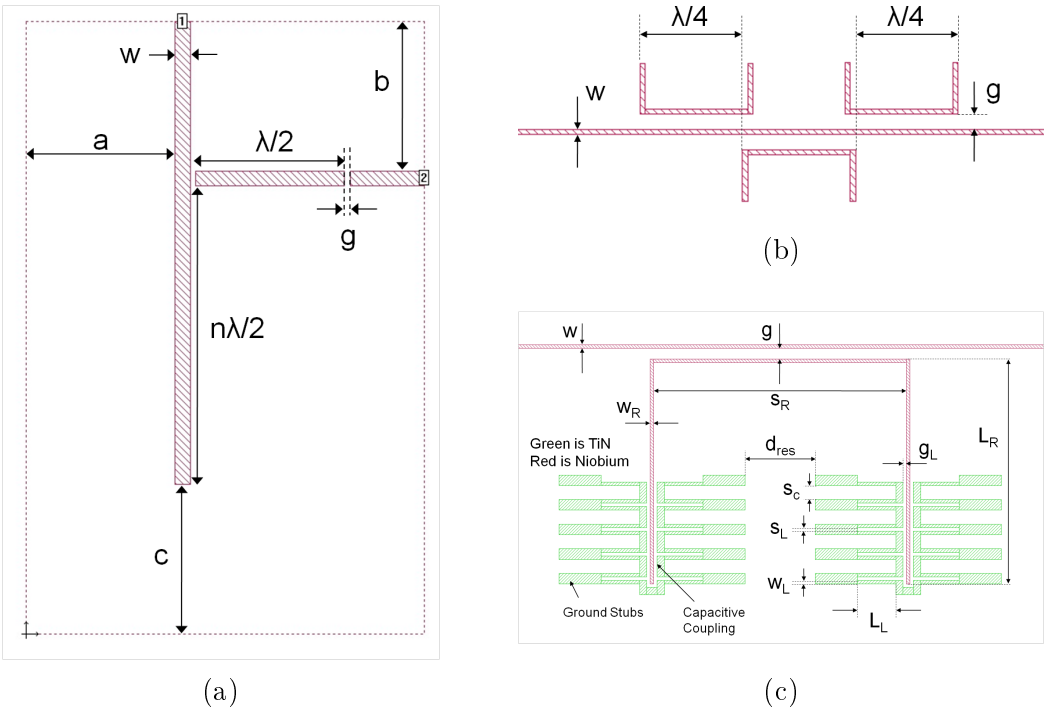

(a) (b) (c)

Figure 3.2: a) Schematic layout of the open-circuit, and b) the matched termination filterbank implementation. c) Proposed detector coupling scheme. The Nb filterbank components are in red and the TiN KID inductor in green.

Fig. 3.2a shows the proposed layout for the first implementation. Here, an antenna (modelled as port 1) couples radiation onto the main feedline which is terminated in an open circuit. Along the feedline are a series of capacitively coupled $\lambda/2$ filters that couple to a power detector that is matched to the characteristic impedance of the feedline (port 2). Each filter is situated an integer number of half-wavelengths from the open end of the transmission line, resulting in an infinite impedance at the resonant wavelength. One of the advantages of this design is that 100% of the in-band power is transmitted to the detector. However, a set of initial simulations found that this

geometry suffered from a number of issues including excessive radiation loss, extremely tight fabrication tolerances, and more fundamentally, the tendency of radiation to travel back toward the antenna and leave the spectrometer. Given the number of issues so early on, this design was discarded in favour of the design shown in Figs. 3.2b and 3.2c.

Similar to the open-circuit design, radiation is coupled onto the feedline and encounters a series of $\lambda/2$ resonators. However, the end of the feedline is terminated in a matched load resulting in very little power is reflected back toward the antenna. The filters are arranged monotonically in frequency and are spatially separated by $\lambda_i/4$, where λ_i is the central wavelength of the ith filter. A disadvantage of this design compared to the previous implementation is that an isolated filter can only absorb a maximum of 50% of the radiation on the feedline in a single-pass. The effect of the quarter wavelength spacing is to induce reflections off of neighbouring filter channels and ultimately increase the efficiency of the bank.

Fig. 3.2c shows the initial implementation of coupling power into the inductive portion of a KID. At the resonant frequency of a filter, the voltage distribution in the filter peaks at the open circuit end and enables efficient capacitive coupling into the detector. At frequencies above the gap frequency of the KID material (TiN) the inductor appears as a set of resistive strips. Fig. 3.3 shows the simulated current density of a single filter coupled to the inductive portion of a KID. Currents induced in the inductor decay over a length determined by the sheet resistivity of the TiN, and is typically in the region of 15 μm. The length of the filters are $\lambda_g/2 \approx 200$ μm, where λ_g is the wavelength on the microstrip line. The short decay length in the TiN enables the inductor to be wound around each filter to obtain a uniform current distribution within the inductor which, for a given volume, maximises the detector responsivity.

3.2 mm-Circuit Design Considerations

In this section we outline some of the basic design concepts for implementation of the first prototype Superspec devices. The choice of materials for each component of the spectrometer is constrained by a number of practical considerations. The main feedline must be made from a material with a superconducting energy gap above photon energy at the highest optical frequency of interest to avoid loss due to quasiparticle dissipation. The choice of material therefore sets an upper limit on the spectrometer operating frequency and corresponds to the gap frequency of the material. For submm astronomy, this restricts the choice of material to ones with $T_c > 4.5$ K. Niobium fulfils this

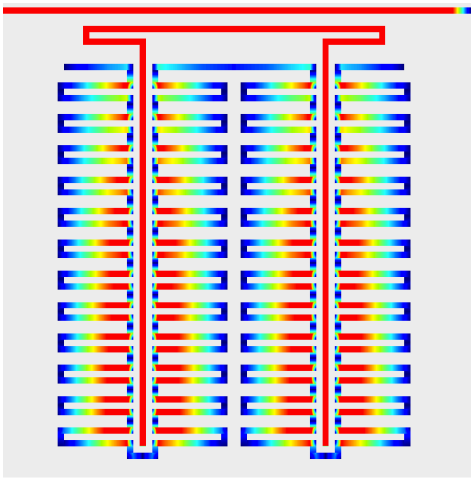

Figure 3.3: Simulated current density at the resonant frequency of a filter coupled to a KID inductor. The maximum response is at the ends of the filter where the electric field is highest. Currents induced in the inductor decay over a length determined the TiN resistivity.

requirement with a gap frequency of $\nu_g \sim 700$ GHz and has been chosen as a baseline for the initial test device. The use of nitride materials such as NbN, NbTiN would enable the frequency of operation to be increased above 1 THz and will be investigated in future design iterations.

For a constant fractional bandwidth filterbank design, the required number of filters to fully sample the bandwidth is given by

$$N_c = \Sigma \mathcal{R} \ln\left(f_u / f_l\right), \tag{3.1}$$

where f_u and f_l are the upper and lower frequencies of the band of interest, $\Sigma \geq 1$ is the spectral oversampling factor and determines the efficiency of the spectrometer. A higher Σ value will result in increased power absorption for a given frequency, but will require more detector channels to read out the increased number of filters. For a prototype, Nyquist-sampled ($\Sigma = 2$), $\mathcal{R} = 700$ device, the required number of detectors is $N_c \sim 1400$. Based on the expected multiplexing density achievable with KIDs, this suggests the possibility that an entire spectrometer chip can be read out using a single measurement line.

Initial designs employ a thin-film microstrip architecture for the filter-bank, which has several advantages over alternative layouts such as CPW. Primarily, the proximity of the ground plane provides a natural means of stray light control, shielding the KIDs from direct illumination. This is vital for spectrometer operation as any parasitic broadband power absorbed by the KID must remain negligible compared to the signal power admitted by the resonant filter. The main disadvantage is that the design

requires the deposition of a thin-film dielectric that has stringent requirements on the loss tangent to achieve the desired performance. For the initial design, we have used a 0.5 μm SiN layer as the dielectric which has been successfully demonstrated in test devices by several mm-wavelength instrument groups at JPL and Caltech.

A schematic of a single filter is shown in Fig. 3.3. The half wavelength filter is bent into the shape of a 'U' primarily to facilitate the coupling of power into the KID, but this design has also been shown to reduce the radiation loss from the resonator (Pauw 1977).

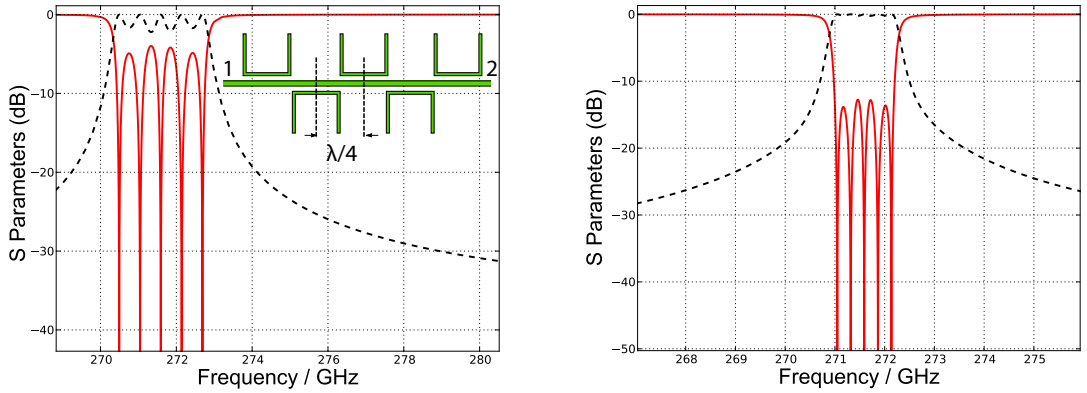

(a) $\Delta l_{res} = 0.4$ μm, $\Sigma = 1.9$ (b) $\Delta l_{res} = 0.2$ μm, $\Sigma = 3.1$.

Figure 3.4: Simulation of the scattering parameters (S_{21} - red solid line, S_{11} -black dashed line) of a signal past a five-element filter-bank to demonstrate the effect of increasing Σ.

A Sonnet simulation of a five-element filter-bank is shown in Fig. 3.4, where the difference in length of adjacent resonators is constant and given by Δl_{res}. The effect of two different values of $\Delta l_{res} (= 0.2, 0.4\,\mu\text{m})$ demonstrates how spacing the filters closer together in frequency decreases the frequency ripple of the pass band, increasing the overall efficiency of the filter-bank.

The spectrometer resolution $\mathcal{R}$ is determined by the quality factor of the filter elements and is given by

$$\frac{1}{Q_{\text{filt}}} = \frac{1}{Q_{\text{feed}}} + \frac{1}{Q_{\text{det}}} + \frac{1}{Q_{\text{loss}}} = \mathcal{R}^{-1}, \tag{3.2}$$

where Q_{feed} is the coupling quality factor which describes the strength of the coupling to external circuitry, Q_{loss} is the internal quality factor which accounts for the dissipative losses such as the conductor, dielectric or radiation losses, and Q_{det} is the quality factor associated with the absorption of mm-wave power in the detector (cf. Section 3.3). For efficient operation, we require $Q_{\text{loss}} >> Q_{\text{det}}$, in which case Eq. 3.2 reduces

to

$$\frac{1}{Q_{\text{filt}}} = \frac{1}{Q_{\text{feed}}} + \frac{1}{Q_{\text{det}}}. \tag{3.3}$$

An analytical expression for the coupling quality factor for the microstrip filters can be derived by modelling the coupling length l_c (cf. inset of Fig. 3.5) as a pair of proximately coupled microstrip lines (Abbosh 2009) and calculating the power leakage from the resonator into the feedline. The result is given by (Zmuidzinas 2011),

$$Q_{\text{feed}} = \frac{4l_{res}^2}{\pi l_c^2} \frac{1}{I(\theta_c)}, \tag{3.4}$$

where

$$I(\theta_c) = \left(\frac{L_\Delta}{L_\Sigma}\right)^2 (1 + \operatorname{sinc} 2\theta_c)^2 + \left(\frac{C_\Delta}{C_\Sigma}\right)^2 (1 - \operatorname{sinc} 2\theta_c)^2 + 2\frac{L_\Delta}{L_\Sigma}\frac{C_\Delta}{C_\Sigma}\left(1 - \operatorname{sinc}^2 2\theta_c\right) \tag{3.5}$$

$$\theta_c = \frac{\pi l_c}{2l_{res}} \tag{3.6}$$

where C_Σ and C_Δ are, respectively, the sum and difference of the even and odd mode per unit length capacitances, and L_Σ and L_Δ are the corresponding per unit length inductances. A comparison of Eq. 3.4 to a set of Sonnet simulations is shown in Fig. 3.5. At large gap distances the analytical formulae are in good agreement with the simulation data points. The discrepancy between the simulation and Eq. 3.4 at small gap sizes may be due to the relative decrease in simulation accuracy due to the cell size being kept constant for all the simulations.

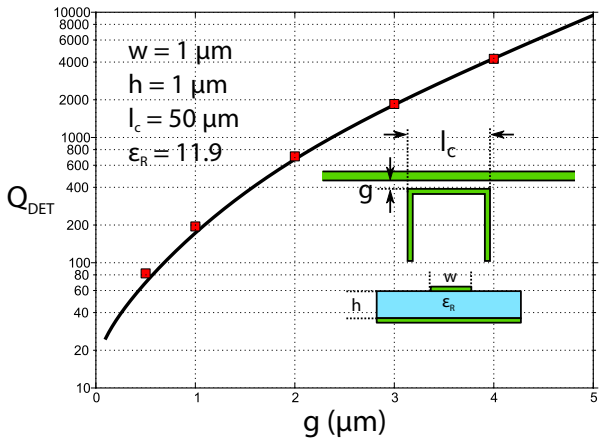

Figure 3.5: Plot of simulated (red squares) and theoretical (black line) values of Q_{feed} for a range of gap sizes for a resonator length $l_{res} = 200$ µm.

The equivalent circuit of the combination of the filter coupled to a detector is shown in Fig. 3.6a. The $\lambda/2$ filter is represented as an inductively coupled LC circuit and at mm-wave frequencies, the detector appears as an equivalent resistance R_d. At the resonant frequency of the filter, the input impedance of the LC resonator is zero resulting in a real input impedance $Z_{in} = R_d$ (cf. Fig. 3.6b). Maximum absorption of 50% occurs when $R_d = Z_0$, or equivalently, $Q_{\rm det} = Q_{\rm feed}$, which from Eqs. 3.2 and 3.3, leads to

$$Q_{\rm feed} = 2\mathcal{R}, \tag{3.7}$$

which determines the required value of $Q_{\rm feed}$ for the filters for a given spectral resolution.

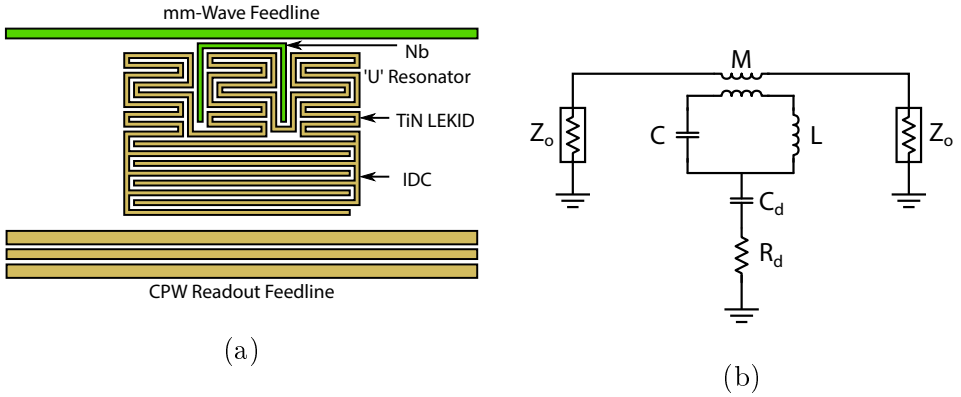

(a) (b)

Figure 3.6: a) Schematic layout of a single filter channel and TiN LEKID. b) Equivalent circuit diagram for a single filter channel. At mm-wave frequencies, the LEKID can be modelled as a lumped resistance.

3.3 Detector Design Considerations

In contrast with the mm-wave feedline and filters, the readout resonator must be dissipative at the signal frequencies of interest (hundreds of GHz) and superconducting at the readout frequencies (hundreds of MHz) in order to achieve efficient detection. This suggests an optimal transition temperature in the range $1 < T_c < 4$ K.

Recently the exploration of superconducting nitride materials has revealed some of the exciting properties of titanium nitride (TiN) for use in microresonator devices. TiN KIDs have achieved internal quality factors as high as 3×10^7, enabling extremely high detector sensitivities (Leduc et al. 2010). Moreover, the ability to tune the superconducting critical temperature of TiN by varying the nitrogen content during the film deposition allows fine control over the material performance. This makes TiN an

extremely attractive material for use as KIDs and for these reasons has been selected for the SuperSpec detectors.

To maximise the number of resonators in a given electronic bandwidth whilst accounting for a degree of non-ideal scatter in the resonant frequencies due to cross coupling, fabrication defects, etc., a targeted minimum internal quality factor of $Q_r = 10^5$ has been set for the SuperSpec TiN KIDs. This value is obtained from the result of a Monte-Carlo simulation that counts how many collisions arise for a given Q_r due to a random scatter in resonant frequency. Defining a collision as two resonators falling within 5 linewidths of each other, a value of $Q_r \geq 10^5$ results in a collision loss of less than 5% of the channels and was deemed acceptable.

To further increase the multiplexing density, the resonant frequency of the KIDs can be reduced down to the RF (100-500 MHz) range. This can be achieved by simply increasing the inductance and/or capacitance of the KID through modification of the geometry, as well as taking advantage of high kinetic inductance of TiN. Furthermore, reducing the operating frequency of the KIDs has the added advantages of reducing the two-level system noise (Zmuidzinas 2012) and reducing the cost and complexity of the readout electronics (McKenney et al. 2012; Swenson et al. 2012).

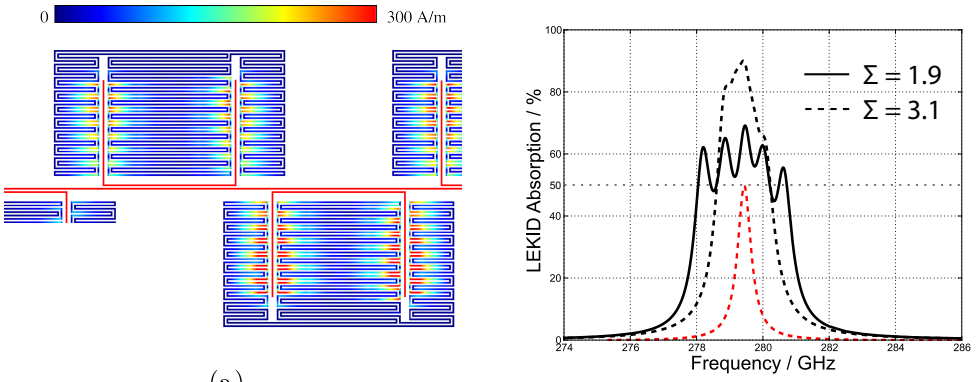

(a) (b)

Figure 3.7: a) Simulated current density at the resonant frequency of the centre filter. b) Simulated absorption for two different values of Σ demonstrating how the efficiency can be increased above 50% of a single isolated matched resonator (red dashed line)

Coupling from the filter to the LEKID, described by Q_{det}, is determined by the properties of the TiN and the geometry of the LE KID inductor. The TiN properties are constrained by the required sensitivity (e.g. T_c, V_{ind})(Zmuidzinas 2011). The inductor geometry (cf. Fig. 3.6a) consists of a double wrapped meander, which has been shown to reduce the effect of microwave cross coupling between resonators (Noroozian et al. 2012), a crucial design consideration in order to maintain uniformity between resonators.

From the mm-wave point of view, the inductive meander can be decomposed into a set of resistive strips each capacitively coupled to the filter tines separated by a gap g_A (cf. Fig. 3.10). The length of the strips is determined by the decay length of TiN such that the opposite end of the strip can be viewed as a virtual ground as the current will have decayed to zero. The lumped resistance in Fig. 3.6b is made up of the parallel combination of all the resistive strips and for a given value of g_A, the required number of strips to maximise the absorber coupling is set by the sheet resistance of the TiN.

These relations, with minor adjustments to account for the coupling between neighbouring resistive strips, should allow for the design of a fully optimised mm-wave circuit. In practice, the SuperSpec prototype design has been driven by the desire to maximise the TiN volume into which mm-wave energy is deposited in order to produce a pixel with suitably low readout frequencies and high absorption efficiency. We therefore choose the densest TiN meander possible for all devices, and then interpolate from a series of Sonnet simulations to choose appropriate values of f_0, Q_{feed}, and Q_{det} in order to achieve specific values of g, l_{res}, and g_A. Fig. 3.7 shows the results of a five-element filter-bank now coupled to a matched absorber.

Fig. 3.7a shows the simulated current density in the KID inductor at the resonant frequency of the bottom resonator. As discussed, power is capacitively coupled into the absorber and the current decays to zero on a characteristic length scale associated with the mm-wave loss in the TiN. Fig. 3.7b shows the a plot of the inferred absorption in the LE KID for two different values of Σ. Absorption of more than 50% of incoming power across the band can be achieved by spacing the resonant frequencies of the filters closer together than the width of an individual channel. With a higher value of the oversampling factor, Σ, one can achieve arbitrarily efficient total absorption at the cost of more readout channels. This effect can be seen in Fig. 3.7a, where incoming radiation at the centre frequency of the bottom resonator excites a (smaller) current in the neighbouring channel.

3.4 Optical Coupling Design

The mm-wave line is coupled to the external optics through a multiple-flare angle horn (Leech et al. 2011). Arrays of horn antennas are a popular choice for many mm-wave and sub-mm instruments. A popular choice is the corrugated horn owing to a number of attractive qualities including, high gain, highly Gaussian beams over a wide bandwidth with extremely low cross polarisation (Wylde 1984). However, the cost

and complexity of manufacture of these horns increases rapidly with frequency and can soon become prohibitive. An alternative approach that has received significant interest is the smooth-walled design that offers comparable performance to the corrugated horn but is much more simple to fabricate. One of the most promising designs that has received significant attention is the Potter horn (Potter 1963); a smooth-walled conical horn which a step discontinuity placed near the throat of the horn results in the excitation of the TM_{11} mode. The fundamental TE_{11} and excited TM_{11} then propagate along the length of the horn, which is designed such that the two modes arrive in phase at the horn aperture. The resulting aperture field distribution results in a highly symmetric beam with high side-lobe suppression.

The multiple- flare angle horn is an extension of the classic Potter horn antenna design and offers performance comparable with a corrugated horn whilst being simple to fabricate. The circular waveguide output of the antenna transitions into single mode oval waveguide to couple to a waveguide probe. The design of the waveguide to microstrip transition is based upon the work presented in Kooi et al. (2003). The probe is broadside mounted such that the substrate faces the direction of propagation in the waveguide, resulting in the probe being orientated parallel to the electric field of the dominant TE_{10} mode. Preceding the filterbank microstrip line is a three-element Chebyshev CPW impedance matching network (cf. inset of Fig 3.8a), designed and optimised to transition the fields from the suspended microstrip to the small buried microstrip line (T. Reck, private comm.). This probe is fabricated on the 25 μm thick device layer of the SOI wafer which supports the spectrometer chip. By careful design of the ground plane of the waveguide probe, coupling to higher order modes in the probe channel was suppressed without the need of wire-bonds or beamleads (Kooi et al. 2003). Simulation of this design shows a coupling efficiency above 90% from 190 to 310 GHz (cf. Fig. 3.8).

3.5 Prototype Device Description

For the prototype device, the mm-wave circuit includes 74 mm-wave filters, 3 in-line broad-band absorbers, and a terminating absorber. The 74 tuned filters span the $200 - 300\,\mathrm{GHz}$ band and include both isolated individual filters and groups of five which are placed close in groups with a range of oversampling factors (Σ). Expected values of Q_{det} and Q_{feed} independently sample the range from 600 to 2800, and include the design goal of $2\mathcal{R} = 1400$. The in-line broad-band detectors consist of a short ($< \lambda_{\mathrm{min}}/4$) feedline meander which is proximate to a TiN absorber, similar to that used in the tuned filters. Sonnet simulations predict roughly 0.5% absorption across

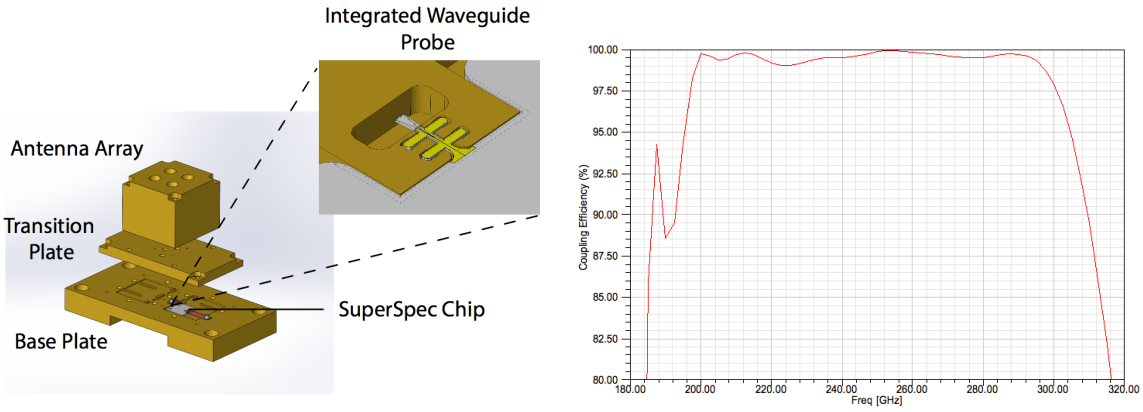

(a) (b)

Figure 3.8: a) CAD model of a 2x2 integrated horn array and packaging for SuperSpec b) Simulated performance of the waveguide-to-microstrip transition.

the full optical band with a slowly varying frequency dependence for these devices, which may be useful in characterising the response of the devices. The terminating absorber consists of several centimetres of meandered feedline surrounded by TiN with a 1 μm separation, designed to absorb any radiation which arrives at the end of the feed and reduce reflections to < 20 dB. Four long segments of the terminating absorber are used as the inductors for an additional set of broad-band absorber KIDs. Furthermore, these broad-band detectors will provide a quantitative measure of the power that is not absorbed by the spectrometer; a potentially valuable diagnostic tool when characterising the performance of the filter-bank.

3.6 Tolerances

The length difference between resonators is approaching the limit of the constraints set by photo-lithography. The ultimate performance of a real device will be determined by the dimensional uncertainty limited by the fabrication capabilities. The deep UV lithographic stepper at JPL can reproducibly achieve 0.1 μm tolerances for features with a minimum reliable line width and gap size of 1 μm. To determine how fabrication tolerances would affect the spectrometer performance, a set of simulations were carried out varying a single dimension over a typical range of values, while keeping all other dimensions at their nominal values. The simulation layout used for the tolerance analysis is shown in Fig. 3.10. Table 1 summarises the results of the tolerance analysis for a range of values that are considered to be achievable using the JPL fabrication facilities. The analysis included both the 'U' resonator and mm-wave absorber to accurately model the contributions from all of the main mm-wave components.

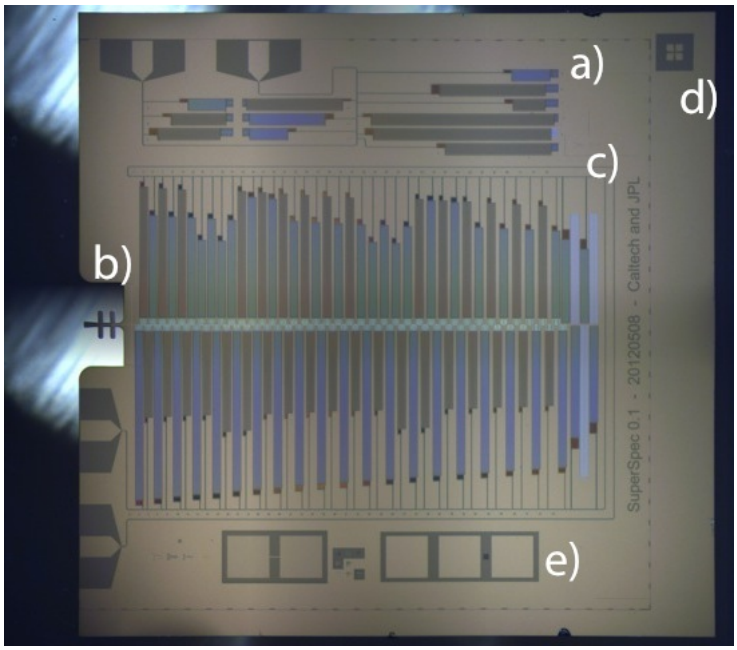

Figure 3.9: Optical micrograph of a full optical SuperSpec device. a) The 12 element sparse array b) The waveguide to microstrip transition probe. **c)** The full 81 element spectrometer array, **d)** Alignment mark for backside processing and **e)** Structures to measure the DC superconducting transition temperature for both the Nb and the TiN.

Table 3.1: Tolerances for an $\mathcal{R} = 700$ microstrip resonator on 0.5 μm silicon nitride

			Fractional change			
Variable	**Description**	**Change**	**Freq**	$Q_{\rm det}$	$Q_{\rm feed}$	$Q_{\rm filt}$
l	resonator length	$0.1\,\mu$m	1×10^{-3}	–	–	–
g	feed to res gap	$0.1\,\mu$m	8×10^{-5}	–	0.19	0.09
g_A	absorber to res gap	$0.1\,\mu$m	4×10^{-5}	0.05	–	0.03
w	Nb line width	$0.1\,\mu$m	3×10^{-3}	0.06	0.11	0.08
w_A	TiN line width	$0.1\,\mu$m	6×10^{-5}	0.06	–	0.03
dx	Nb/TiN offset in x	$0.1\,\mu$m	5×10^{-6}	0.006	–	0.003
$R_{\rm TiN}$	Resistivity	20%	6×10^{-5}	0.03	-	0.02
ϵ_N	SiN permittivity	2.5%	8×10^{-3}	0.05	0.004	0.02
T_N	SiN thickness	2.5%	5×10^{-4}	0.07	0.09	0.08
$\tan\delta$	SiN loss	$+10^{-4}$	–	0.04	–	0.02

The main dimension that requires strict control is the feedline to filter coupling gap (g) which determines the coupling quality factor and ultimately the spectrometer resolution. A ±0.1 μm variation in gap translates to a 20% variation in $Q_{\rm feed}$, so tight control over the etching process during fabrication is essential. Variations in the width

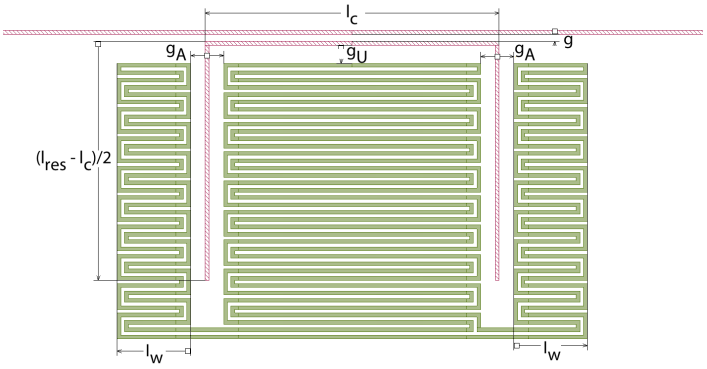

Figure 3.10: Parametric simulation layout for the tolerance analysis.

of the feedline and resonator line have a similar effect on Q_{feed}.

The dielectric properties of the SiN layer also require fine control. The variation in permittivity affects only the detector quality factor, Q_{det}, of the KIDs as the filters are inductively coupled to the feedline and have a resulting immunity to the dielectric constant, whereas the coupling between the filter and mm-wave absorber is predominantly capacitive. The dielectric thickness on the other hand, effects both the feedline and filter impedance resulting in a modification of both Q_{feed} and the coupling to the mm-wave absorber. Control of this dimension on the $< 3\%$ level is required to ensure that it is not the dominant cause of scatter in the filter Q.

Preliminary simulations suggest several approaches which can relax these tolerances even further, including designs in which multiple mm-wave resonators are coupled to a single KID absorber, and designs which make use of a second intermediate $n\lambda/2$ resonator between the filter channel and KID (Kovacs et al. 2012). These will be investigated in future design iterations.

3.7 Twelve-Element Test Array Description

Also included on the test device is a twelve-element test array that has a number of slightly different KID designs based around the baseline spectrometer design. Design variations include a range of inductor sizes along with the two capacitor geometries used in the spectrometer array. Contrary to the spectrometer resonators, all but one of the test resonators have the dielectric/ground plane layer removed and replaced with a dedicated parallel plate capacitor to provide the current return to ground. This was intended to diagnose and quantify any additional TLS contribution that might originate from the SiN dielectric layer. The range of Q_c values are designed to span a wide range and provide the opportunity to drive the resonators with significantly

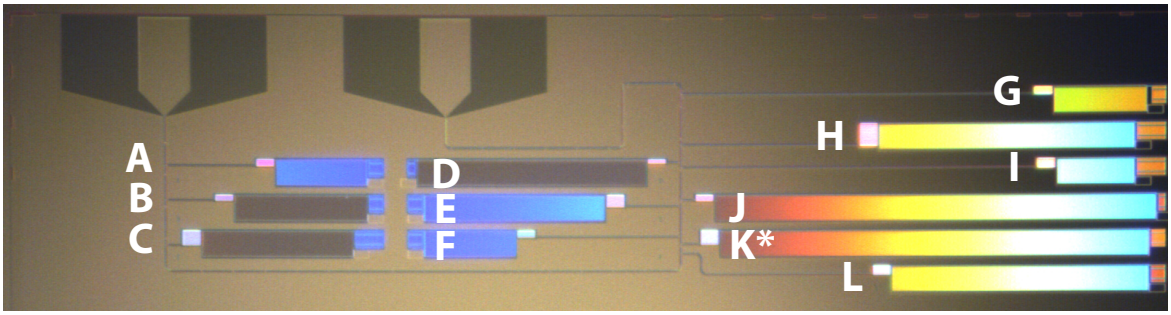

Figure 3.11: a) Photograph of the sparse 12 element test array along with its designated pixel reference.

Table 3.2: Design parameters for the 12 element test array. $L_0 = 137\,\mu\text{m}^3$

KID ID	f_r [MHz]	$Q_c(\times 10^3)$	L/L_0	$1 \vee 2\,\mu$m
H	100	4.52	2	2
K*	110	48.3	1	2
E	120	11.1	1	1
C	132	3.0	2	2
L	145	10.6	1	2
J	159	35.6	0.5	2
G	173.5	9.1	1	1
F	174	9.1	1	1
A	175	8.9	1	1
I	191	2.1	2	2
B	210	7.3	1	2
D	230	27.2	0.5	2

more power than the spectrometer resonators, which is useful when investigating the effects of the TLS contributions to resonator performance. A summary of the main design parameters for each resonator is given in Table 3.2 along with a photograph illustrating the identification scheme.

In Chapter 4, the test array is used to provide detailed measurement and characterisation of the TiN film.

3.8 Fabrication Steps

In this section an overview of the various fabrication steps undertaken to manufacture the initial test devices is presented. All of the device processing was carried out by Dr. H. G. LeDuc at Microdevices Laboratory at JPL, and the steps are repeated here with permission.

All front-side patterning is performed using the DUV projection lithography tool (Canon FPA3000-EX3 / KrF with a 248nm exposure) capable of fabricating line-widths down to 0.5 μm. Here we list each fabrication step in the order that it was carried out.

a) TiN deposition: DC sputter deposited film to a nominal thickness of 20 nm. Calibration of the deposition rate is performed periodically by depositing and patterning test structures using a lift-off process and measuring with a scanning profilometer (Dektak).

b) The TiN films are plasma etched using an inductively coupled plasma - reactive ion etcher (ICP-RIE) using a gas mixture of BCl_3 and Cl_2. Post-etch, the wafers are rinsed thoroughly in deionized water to remove any chlorine residue left as a bi-product of the etch. A protective layer of a 120 nm SiO_2 is grown and patterned over the TiN. The SiO_2 is grown using RF-magnetron PVD from a synthetic fused silica target, and is patterned using the TiN mask and a plasma etch consisting of a mixture of CHF_3 and O_2.

c) Sputter deposition of Nb feature layer with thickness 150 nm by DC-magnetron PVD.

d) Pattern and etch of the Nb layer to define the mm-wave circuit and the centre line of the CPW readout line. A plasma etch in an ICP-RIE using a mixture of BCl_3 and Cl_2, which is stops at the silicon and SiO_2 layer. Alignment of this layer to the TiN layer is critical. The JPL stepper system typically achieves alignment accuracy of ± 0.1 μm (cf. Section 3.6).

e) Deposition of the 0.5 μm Si_3N_x dielectric layer using an inductively-coupled plasma-enhanced system (ICP-PECVD) using SiH_4 and N_2O_2 and 350 nm Nb ground-plane layer. The thickness of the Nb ground-plane layer is chosen to ensure good step coverage over the entire wafer.

f) Pattern both Nb and Si_3N_x to expose the IDCs and define the CPW ground-plane. The Nb/SiNx stack is etched in a ICP-RIE using a multi-step plasma etch process. The Nb is etched using a mixture of CCl_2F_2, CF_4, and O_2. The

Si_3N_x is etched using the same gas mixture used to etch the SiO_2. Nb has a relatively slow etch rate in the latter gas mixture so that a short over etch does not damage the exposed Nb features as the Si_3N_x clears. The thin TiN layer is protected by the SiO_2, which is thick enough to accommodate the over etch of the Si_3N_x layer.

For the non-optical devices (SS03), the removal of the protective oxide is etched in a buffered oxide etch (BOE)[1] as the last step. The following steps are relevant to defining the horn probe for the optical devices.

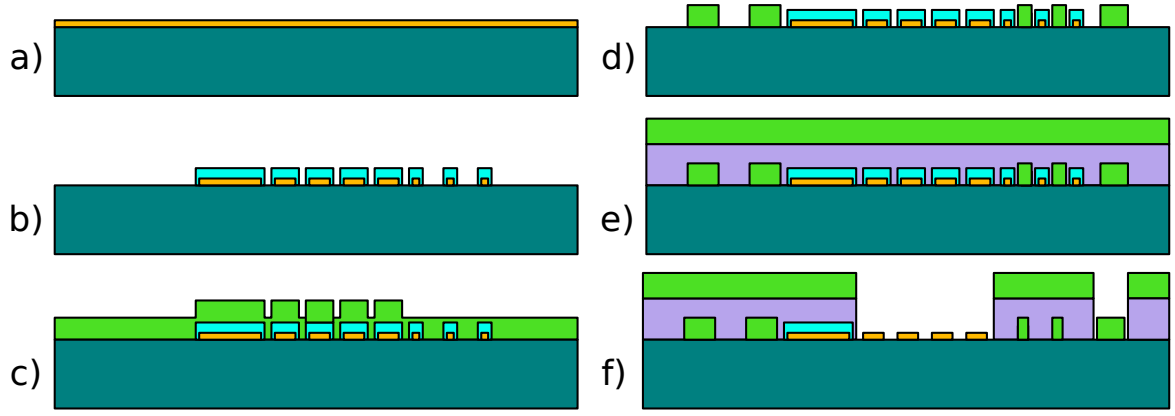

Figure 3.12: Fabrication steps. See text for details. Key: Teal - silicon wafer, Orange - TiN, Green- Nb, Light blue - SiO_2, Purple - Si_3N_x.

g) Pattern probe from front side of wafer using a thick resist and DRIE trench etch down to the BOX layer of the SOI. Included in this step is a set of alignment marks for front to backside alignment.

h) Backside pattern to include the device alignment features. The frontside features are covered in a protective layer of photoresist and then bonded to a handle wafer using a water soluble wax. The backside features are aligned and then patterned using a contact mask.

i) The silicon is etched using DRIE through the handle wafer, stopping on the BOX. Post resist strip, the BOX layer is etched using buffered oxide etch BOE. The water soluble wax works fine for thin BOX layers (0.5 micron) but for thicker layers the longer BOE etch dissolves the wax and the Si_3N_x and Nb are attacked.

[1] A mixture of a buffering agent, such as ammonium fluoride (NH_4F), and hydrofluoric acid (HF).

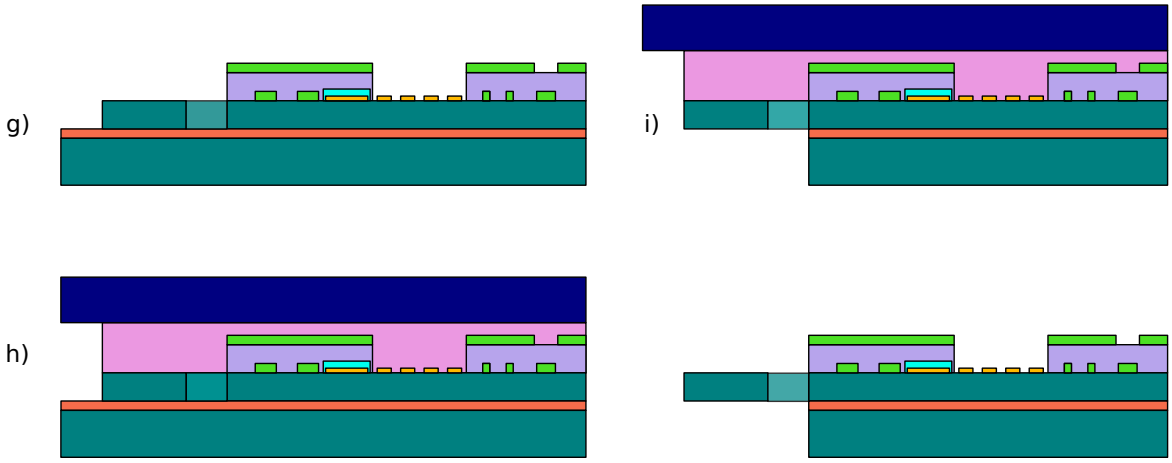

Figure 3.13: Final fabrication steps for the optical devices. See text for details. Key: As above, Red - BOX layer, Pink - bonding wax, Dark blue - handle wafer.

Chapter 4

Characterisation of the SuperSpec Detectors

In this Chapter we present a dark characterisation of the TiN resonators on one of the devices from the fifth fabrication run (SS05). An understanding of the resonator performance is critical to understanding the spectrometer operation, as any issues with the detectors will have a significant impact of the spectrometer performance. Results are presented on general resonator properties as well as the noise performance from a number of measurements on both the spectrometer array and from the diagnostic test array.

4.1 Measurement Setup

A CAD model of the device holder is shown in Fig. 4.1b. It is made of a single piece gold-plated copper to ensure good thermal contact to the chip. The device is bolted to the cold plate of the cryostat using brass screws along with a spring washer. The RF connection is made through a commercial SMA to microstrip transition. The microstrip pin is soldered onto a custom made four-channel, 50 Ω microstrip connector board manufactured from gold plated copper layer on a TMM10[1] substrate. The microstrip is terminated in wirebond pads which are used to connect to the CPW line on the device. Also included in the holder is a simple four-wire connector for connections to the DC structures on the device.

All of the high-frequency measurements in this thesis are obtained using either a vector network analyser (VNA), used to perform frequency sweeps of the resonators,

[1] http://www.rogerscorp.com/acm/index.aspx

or using a single pixel, homodyne readout scheme (Day et al. 2003) to measure noise. A schematic of the homodyne measurement configuration is shown in Fig. 4.1a. A tone generated from a low noise synthesizer is split with half the power half going directly to the LO port of an in-phase/quadrature (IQ) mixer, and the other half going to the cryostat. The power of the synthesized tone is determined by the recommended mixer LO input power and is typically +5 dBm. Before the tone reaches the cryostat it is passed through a variable attenuator that is used to fine tune the resonator readout power. There is further fixed attenuation inside the cryostat located at both 4 K and 300 mK intended to minimise the amount of thermal power generated at room temperature reaching the device. After the tone passes the resonators it is amplified by a high-gain (typ. 35 dB) low-noise cryogenic amplifier that is mounted on the 4 K stage. A low pass filter with cut-off at 200 MHz placed at the output of the cryostat is required to limit the amount of noise power from saturating subsequent amplifier stages. Due to the resonator design, the readout power of the SuperSpec resonators is extremely low (typ. -120 dBm) and requires multiple room temperature amplifiers to boost the signal to the operating level of the IQ mixer (typ. -20 dBm min.). With the tone at an appropriate power it is then mixed with the original copy of itself and the IQ mixer produces voltages that are proportional to the real (I) and imaginary (Q) parts of S_{21}. The signals $I(t)$ and $Q(t)$ are then low-pass filtered to prevent aliasing and then digitized and saved to disk for further processing.

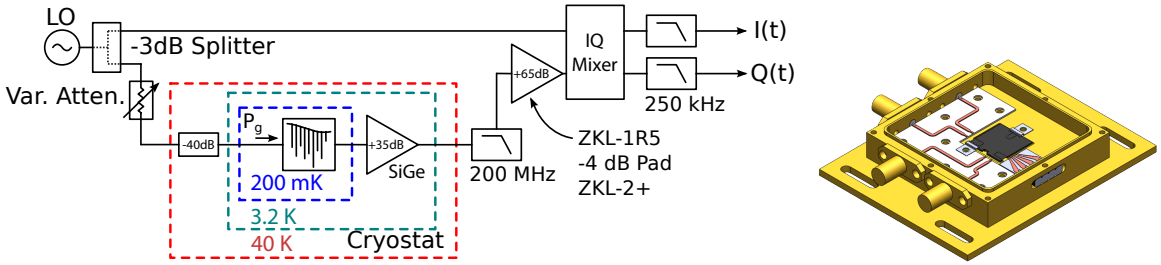

(a) (b)

Figure 4.1: a) Schematic circuit layout used for single-pixel homodyne measurements. b) CAD model used for dark device characterisation.

A typical noise measurement consists of an initial calibration sweep to find the resonant frequency and then fixing the tone at f_r and monitoring the output of $I(t)$ and $Q(t)$. For each point in the sweep consists of an average of a short sample of 5 kS sampled at the maximum rate of 500 kS/s. For the timestreams, both the sample length and rate are adjustable and would typically consist of taking a number of short timestreams sampled at the maximum rate along with longer sample lengths with a slower sample rate to minimise disk space.

4.2 Critical Temperature Measurement

The initial step in the characterisation of a superconducting film is generally to measure the film T_c and normal state resistivity σ_n. On each device there is a set of simple test structures to measure the T_c of the TiN and Nb and consist of two wirebond pads connected via a thin metal bridge (cf. inset of Fig. 4.2). The length and width of the bridge is $200 \times 20\,\mu\text{m}$ and has a measured room temperature sheet resistance of $R_s = 83\,\Omega/\text{sq}$.

Using a standard four-wire measurement the resistance of the TiN was monitored as a function of the fridge temperature using a Picowatt AVS-47B AC resistance bridge. The data in Fig. 4.2 indicates a film $T_c \approx 2.12$ K and residual resistance ratio (RRR) = $R(300\text{K})/R(4\text{K}) = 1.15$. The normal state conductivity can be calculated from

$$\sigma_n^{-1} = \rho_n = R_s t, \tag{4.1}$$

where $t = 20$ nm is the film thickness, which gives $\sigma_n \approx 6.8 \times 10^3\,\Omega^{-1}\text{cm}^{-1}$. This value can be used in the Mattis-Bardeen expressions to predict the properties of the TiN and compare to the measured data.

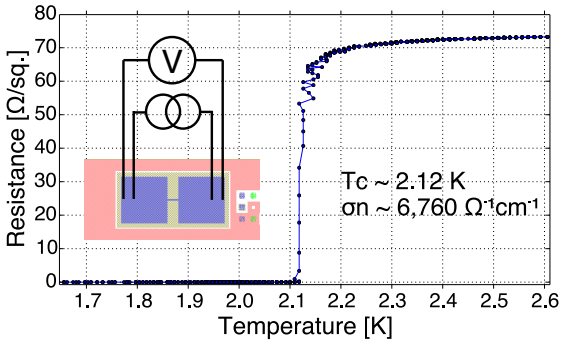

Figure 4.2: Measurement of resistance versus temperature to extract T_c of the titanium nitride film.

4.3 Spectrometer Array

As described in Chapter. 3, the spectrometer array consists of 77 spectrometer detectors and 4 low frequency detectors designed to absorb any power not accepted by the spectral channels. The results from a set of VNA sweeps of the spectrometer detectors at the base temperature of 230 mK are shown in Fig. 4.3. For this array, all 77 detectors were present allowing identification of each channel to its design value. Tests of

several devices measured both at Cardiff and at Caltech indicate an average detector yield close to 96% (Shirokoff et al. 2014).

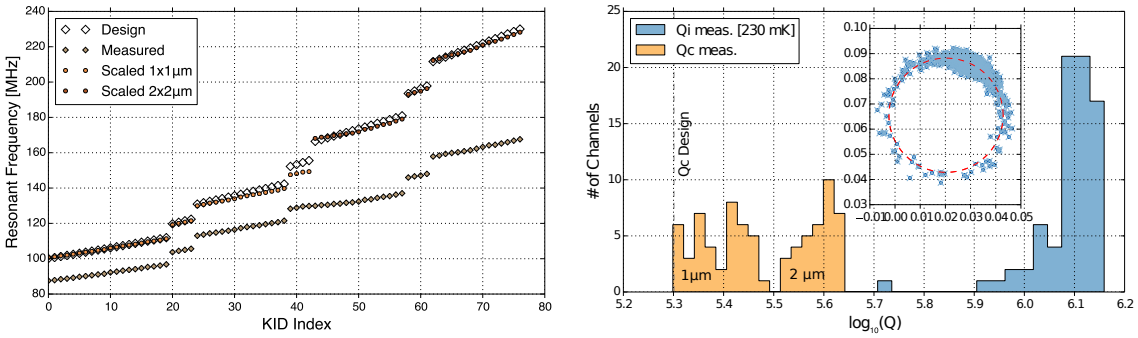

Figure 4.3: a) Comparison between design and measured resonant frequencies for the SS05-CDF02 device at 230 mK. b) Histogram of Q_c and Q_i values extracted from fits to the centred and rotated phase. The inset shows a typical fit to the complex data to determine the centre and radius of the resonance circle.

However, for the SS05 fabrication run, the frequencies are consistently observed to be between $70 - 80\%$ lower than expected. A linear scaling applied separately to the 1 μm and 2 μm capacitor geometries results in good agreement with the designed values, but the cause of the shift has not been identified. The most likely cause is a variation in the TiN film properties. For example, an increase in resistivity, decrease in film thickness or reduction in T_c all combine to increase the sheet inductance of the TiN. On the other hand, the difference in shift is clearly dependent on the capacitor geometry, which could point to a variation in the dielectric constant. However, if the linewidth was smaller than expected due to uncertainties in the photolithography, then the spacing of the capacitor electrodes would also be affected. While it is not ideal, the frequency shift is not a major issue and should be easily resolved with improved calibration of the film properties in future fabrication runs.

A histogram of measured values of Q_c and Q_i extracted from fits to the centred and rotated phase is shown in Fig. 4.3b. The inset shows a typical fit to the complex data used to determine the centre and radius of the resonance circle that is used to extract Q_i (Gao 2008). The average value of Q_i measured at 230 mK is well in excess of 10^6 indicating good quality material with no major unforeseen loss mechanisms. However, extremely high internal quality factors ($> 10^7$) have been observed in TiN resonators (Leduc et al. 2010; McKenney et al. 2012), which leads to the question of the loss mechanism that limits Q_i. One candidate is an excess quasiparticle density due to absorption of stray light. For this measurement the device was housed light-tight enclosure, the inside of which is blackened to absorb any stray photons. It has been shown (Baselmans et al. 2012) that at the lowest levels stray light leaks through

the coaxial cables can give rise to an excess quasiparticle density. However, as we show below, the most likely cause is due to a contribution from two-level systems (TLS).

The measured values of Q_c fall into a bimodal distribution that correspond to the different capacitor geometries. The mean value of both distributions is higher than designed value of 2×10^5. Recalling that $Q_c \propto f_r^{-1}$, and assuming that the resonator and coupling capacitor values are approximately as designed, then the value of design Q_c should be scaled by the ratio of the measured and designed resonant frequency. These are found to be approximately 1.2 and 1.9 for the 1 µm and 2 µm capacitor geometries respectively, and are in good agreement with the measured values. The

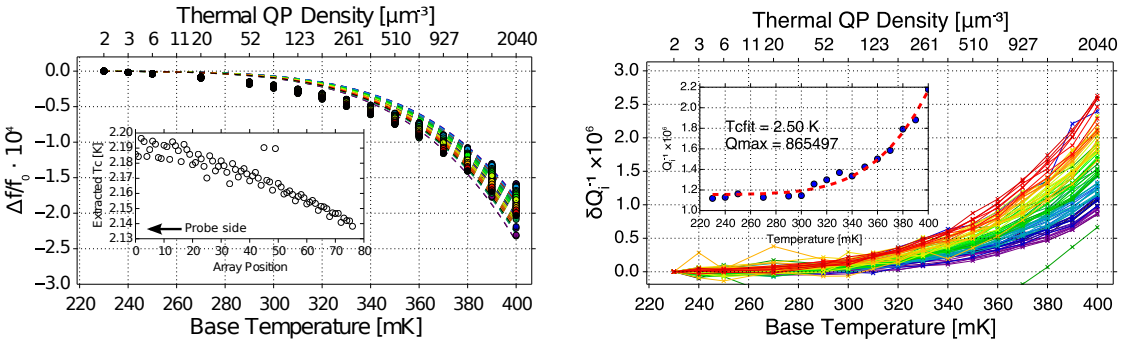

Figure 4.4: a) Measured fractional frequency shift for all 77 resonators as a function of fridge temperature. Inset shows the extracted values for T_c as a function of position on the array. b) Shift in extracted internal quality factor as a function of base temperature. See text for discussion.

measured fractional frequency and internal quality factor shift for all 77 resonators as a function of base temperature is shown in Fig. 4.4. The quasiparticle number has been calculated using the thermal approximation (Eq. 2.12). The dashed lines in the are a fit to Mattis-Bardeen theory (c.f. Eq. 2.61) to extract Δ_0 assuming $\alpha_k = 1$. The discrepancy between the fit and the data at low temperatures is seen in various devices from this wafer and indicates an increased responsivity to thermal quasiparticles at low temperatures that is not predicted by Mattis-Bardeen theory. This effect is discussed in more detail in the following section.

The inset of Fig. 4.4 shows values for $T_c = \Delta_0/1.76k_B$ extracted from the fit as a function of position on the array. The T_c values are in good agreement with the measured DC value but a clear variation in the film properties across the device is observed and is most likely due to a systematic variation in the film thickness across the wafer. Similar behaviour has been observed in experiments on TiN films (Gao et al. 2012; Diener et al. 2012; Vissers et al. 2013a) and is attributed to the sensitivity of the T_c on nitrogen content which is difficult to control over the extent of a typial

wafer size. An alternative approach of using Ti/TiN/Ti trilayers has been proposed by Vissers et al. (2013b) and has been shown to improve film uniformity whilst keeping the promising attributes of TiN, and may be worth investigating in the future.

A plot of the shift in internal quality factor as a function of base temperature is shown in Fig. 4.4b. The colour represents the resonant frequency of resonator with blue/purple denoting low frequency. It is evident that there is a significant change in the dissipation response as a function of resonant frequency. An estimate of the expected value of Q_i from thermal quasiparticles can be determined from

$$Q_{i,qp}^{-1} = \alpha_k \frac{S_1(\omega)}{\Delta_0} \sqrt{2\Delta_0 \pi k_B T} \exp\left(-\frac{\Delta_0}{k_B T}\right). \tag{4.2}$$

Inserting the appropriate measurement parameters results in $Q_{i,qp} \approx 150 \times 10^6$, about two orders of magnitude higher than what is observed. The inset of Fig 4.4 shows an example of the raw Q_i^{-1} data at various bath temperatures. This data was fit to a loss model that contained contributions Mattis-Bardeen (cf. Eq. 4.2) and a fixed loss term to account for the limiting Q_i.

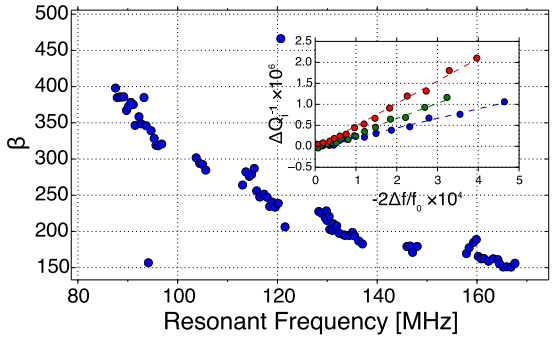

Figure 4.5: Plot of $\beta = \delta x / \delta Q_i^{-1}$ for each resonator of the spectrometer array as a function of resonant frequency. Inset shows examples of the response in frequency and dissipation used to calculate β for three typical resonators. Blue, green and red are from resonators at 57, 114 and 136 MHz, respectively.

The measured ratio β of the response in the two quadratures is shown in Fig. 4.5. The limiting Q_i diminishes the response in the dissipation direction leading to an increased β relative to the MB prediction. However, the frequency dependence does appear to follow the $\beta \propto \omega_r^{-1}$ predicted from the ratio of $S_2(\omega)/S_1(\omega)$ (Swenson et al. 2012).

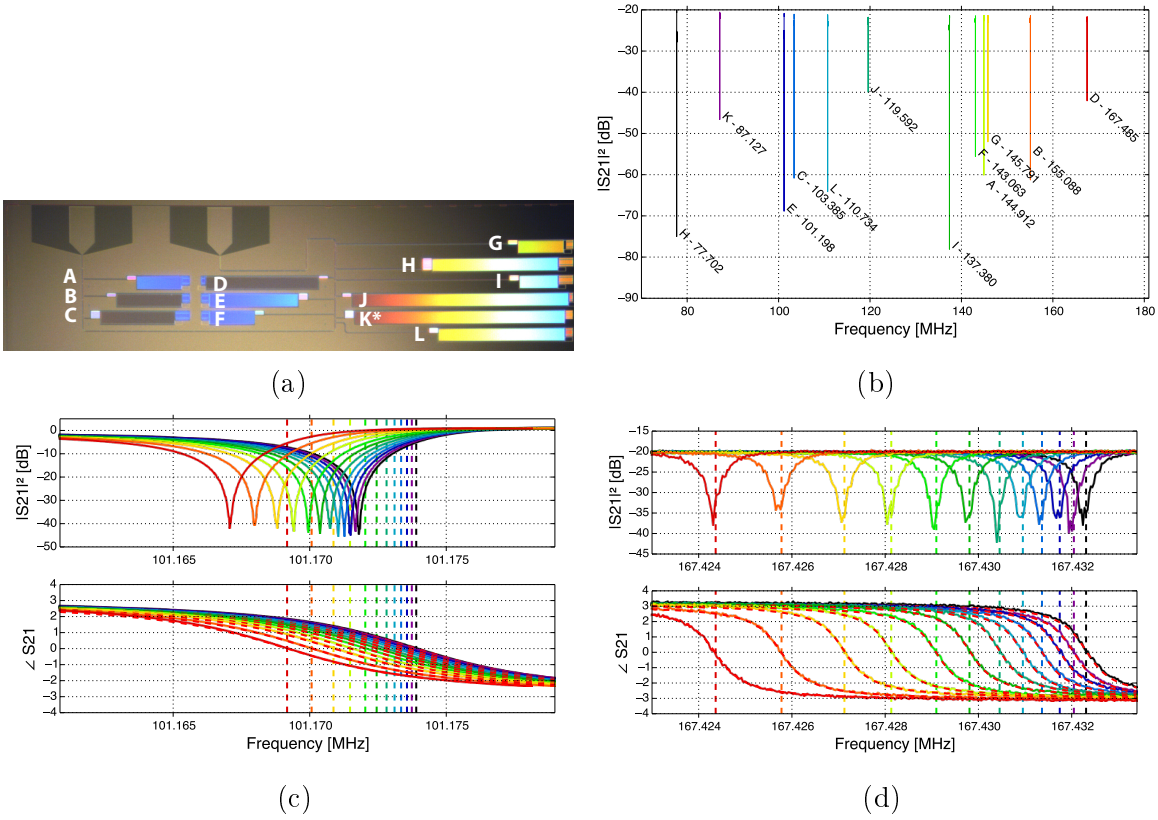

Figure 4.6: a) Optical micrograph of the sparse 12 element test array along with its designated pixel reference. b) $|S_{21}|^2$ for the test array. All 12 resonators were identified (see text for details) with the corresponding design values. c, d) Magnitude and phase of the transmission of a low-Q_r (13k) KID101 (E) (c) and high-Q_r (200k) KID167 (D) (d) as a function of temperature. Red dashed lines in the lower plots are the fits to phase viewed from the circle centre, while vertical dashed lined are resonant frequency extracted from the fit. Note that for KID-E, the fitted f_r is significantly different from $S_{21}^{\min}$, indicating a significant rotation of the complex transmission data.

4.4 Twelve Element Test Array

Next we present a detailed characterisation of the TiN using the small twelve element test array. The wide range of Q_c values along with various resonator designs makes the test array a useful diagnostic of the film properties. A full description of the test array can be found in Chapter 3, and a photograph of the test array illustrating the identification scheme is shown in Fig. 4.6a.

4.4.1 Pixel Identification

A VNA sweep of each resonator at the base temperature is shown in Fig. 4.6b. After fitting f_r and Q_r we can compare the measured parameters to the design values given

in Table 3.2 and identify a corresponding pixel to each resonance.

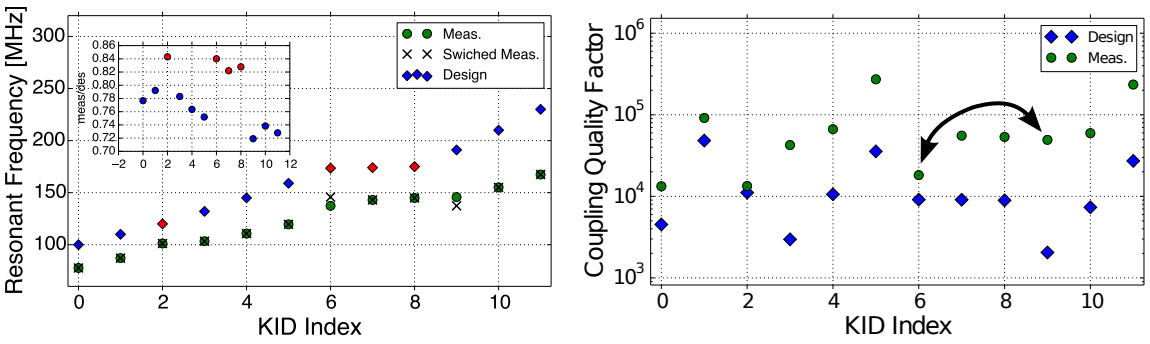

(a) (b)

Figure 4.7: Comparison of design and measured values of a) the resonant frequency and b) the coupling quality factor. The red points in the frequency plot denote the resonators that have 1 µm capacitor geometry.

A comparison of the design and measured values of f_r and Q_c is shown in Fig. 4.7. Similar to the spectrometer array, the resonant frequencies are between $70-85\%$ of the design value (c.f. inset of Fig. 4.7a). It can be seen that for the majority of the resonators there is a simple mapping between the design and measured frequencies. However, based on the Q_c distribution it is most likely that frequency of resonator I has moved below the group of three closely spaced resonators F, G, A. The inset of Fig. 4.7a shows the ratio of the measured to designed frequencies with the corrected indices, highlighting the dependence on the capacitor geometry.

4.4.2 Temperature Sweeps

The fractional frequency shift as a function of thermal quasiparticle density is shown in Fig 4.8a, with similar behaviour to spectrometer array is observed. The variation in T_c across the device splits the frequency response into two trajectories that corresponds to the two groups of six resonators $A-F$ and $G-L$. As mentioned above, there is an a apparent increase in responsivity to thermal quasiparticles at low temperature. This behaviour is seen on all the devices from the SS05 wafer, as well as other TiN films from different fabrication runs. As shown in Fig. 4.8b there appears to be no power dependence which suggests against it being either a TLS effect or non-linear feedback in the resonator from the bias tone. Similar behaviour has been observed elsewhere in TiN (Gao et al. 2012) and in experiments on NbTiN (Barends et al. 2008). The authors argue that the contribution of states that reside in the previously forbidden energy gap can give rise to an increased response at low temperature. An

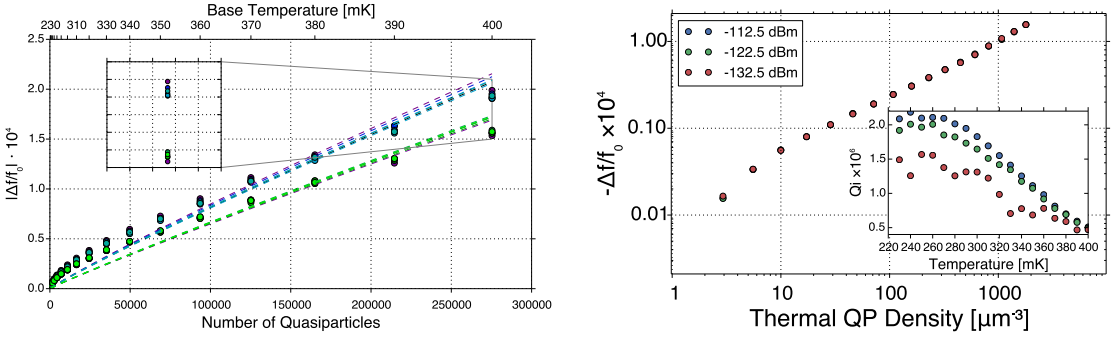

(a) (b)

Figure 4.8: a) Measured fractional frequency shift as a function of thermal quasiparticle number for the 12 element test array. The resonances fall into two groups of six (see inset) that, after switching pixels I and G, correspond to pixels $A - E$ and $G - L$. Dashed lines are fits to Eq. 2.61. b) Fractional frequency shift for a range of readout power for KID155. Inset shows the power dependence of Q_i. Note that the three powers lie on top of each other.

appropriate modification of the Mattis-Bardeen equations that include a density of states broadening term (Dynes et al. 1978) results in a good fit to their data. Physically the gap-broadening parameter smooths the singularity in the conventional density of states at $E = \Delta$ and introduces so-called sub-gap states, which gives rise to the enhanced responsivity at low temperature. To confirm if this is the case, additional measurements would be required. Ideally an independent measure of the form of the density of states could be determined through tunnelling experiments (Escoffier et al. 2004). Additional measurements of the existing device at lower base temperature would be interesting to determine the limiting form of this effect at extremely low quasiparticle densities.

4.4.3 Power Handling

One of the characteristic signs of the onset of non-linear effects in a resonator is a shift in frequency with readout power. As the power is increased further, the resonance distorts and eventually bifurcates resulting in a discontinuity in the transfer function (cf. Fig. 4.9a). Swenson et al. (2013) derive an expression that can be used to estimate the bifurcation power based on the second order effect of non-linear kinetic inductance on the resonator transmission and is given by (cf. Chapter 2),

$$P_{g,max} = \frac{a_c Q_c 2\pi f_r N_0 V_L \Delta_0^2}{4Q_r^3}. \tag{2.59}$$

For $Q_r \approx Q_c$ which is relevant for this discussion, then $P_{g,max} \propto f_r V_L Q_r^{-2}$. We can use this relation to compare the predicted readout power with the measured values given in Table 4.1. Here the optimum power was determined manaully by increasing the readout power until a clear disconinuty in the resonance appeared and then reducing the attenuation by 2/4 dB. The scaling relation is shown graphically in Fig. 4.9b for a selection of resonators with various design parameters.

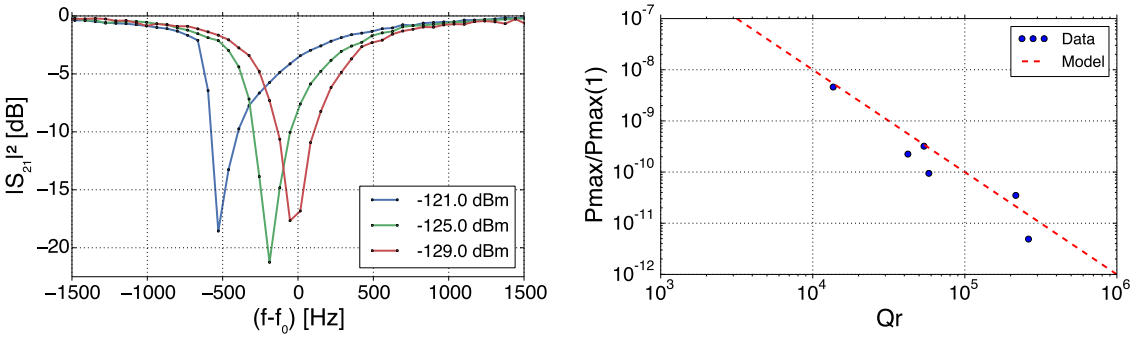

(a) (b)

Figure 4.9: a) Example $|S_{21}|^2$ of KID167 at different drive powers demonstrating the onset of bifurcation. b) Normalised maximum power as a function of Q_r for the resonators given in Table 4.1.

Assuming a constant T_c, and scaling with the volume and resonant frequency, we find that we are able to accurately predict the expected bifurcation power to within ± 2 dB. There are, however, a number of uncertainties involved in the estimate of the power on the feedline at chip-level. Potential mismatch loss between the coaxial to CPW transition are difficult to measure without a measurement of S_{11}. That being said, if there was a significant mismatch then we would expect to see the characteristic ripple in S_{21} due to standing waves, which is not evident in the data. Other effects such as the uncertainty of the cold cable attenuation could also affect the estimate of the power on the feedline. More fundamentally, accurately determining exactly when the resonator enters the bifurcation regime is not trivial, and requires very fine sweeps, ideally in both directions (Swenson et al. 2013). Therefore, while the estimate indicates that the non-linear kinetic inductance model is adequate to predict the bifurcation power, further work is required to rigorously test the validity of Eq. 2.59.

4.5 Noise Measurements

In this section we investigate the dark noise properties of a number of resonators from the test array. A detailed description of measurement setup can be found in Section

5.2.

4.5.1 Noise Calibration

We probe the resonator by monitoring the change in real and imaginary parts of the forward transmission coefficient of the scattering matrix and need to relate this to a change in the resonator parameters ω_0 and Q_i (cf. Chapter 2).

There are two methods that have been used to convert the raw output of the IQ mixer to an equivalent shift in the resonant frequency of the resonator. First a frequency sweep is made around the resonance to determine the resonant frequency, which is then used for the frequency of the bias tone. Once the source frequency is set, the $I(t)$ and $Q(t)$ signals are digitised at a sample rate for a specified sample time that is appropriate for a given measurement; a long sample time is required to attain the information at low modulation frequency, whereas the hardware limited sample rate determines the highest achievable frequency. In practise, the goal is to capture to the resonator roll-off along with an estimate of the in-band noise level. A sample time of 2 s results in a frequency resolution of 0.5 Hz, and is the longest sample time used here. The resonator roll-off occurs at $f_0/2Q_r$ resulting in resonator bandwidths in the range $0.2 - 2$ kHz, such that a sample time of 0.1 s is sufficient. To reduce the variance of the noise in the final PSD, multiple timestreams are taken, converted to a frequency shift and averaged in the Fourier domain.

The frequency sweep is used to convert $I(t)$ and $Q(t)$ to δf. Here two methods are presented and compared.

Multiplication Method

The first is a simple method that can be derived from the forward transmission of a resonator, which can be expressed generally as a complex number $S_{21} = I + jQ$. A perturbation in the resonant frequency $\delta f = f - f_r$, can be written as

$$\delta f(t) = \left.\frac{df}{dS_{21}}\right|_{f_r} \delta S_{21}(t), \tag{4.3}$$

where $\delta S_{21}(t) = \delta I(t) + j\delta Q(t)$. Furthermore, the derivative of S_{21} with respect to frequency can be written as

$$dS'_{21}|_{f_r} = dI'_r + jdQ'_r, \tag{4.4}$$

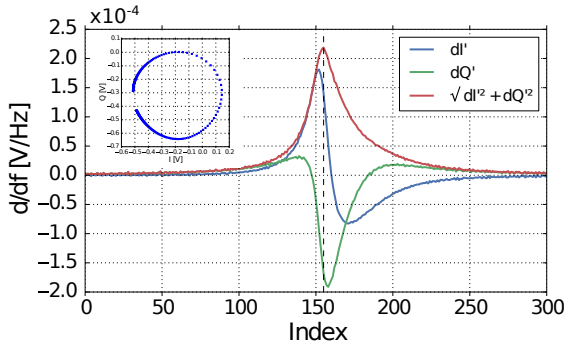

Figure 4.10: Example of sweep data analysis demonstrating the values of dI' and dQ'. The dashed black line corresponds to the maximum of $dI'^2 + dQ'^2$ and is taken as the value for f_0.

where primed quantities denote the differential with respect to frequency. An example of these quantities for a sweep of KID101 at 230 mK is shown in Fig. 4.10. The dashed black line is the maximum value of $dI'^2 + dQ'^2$ and determines the value of dI'_r and dQ'_r at the resonant frequency. Combining Eq.s 4.3 and 4.4 results in

$$\begin{aligned}\delta f(t) &= \frac{\delta I(t) + j\delta Q(t)}{dI'_r + jdQ'_r} = \frac{(\delta I(t) + j\delta Q(t))\,(dI'_r - jdQ'_r)}{dI'^2_r + dQ'^2_r} \\ &= \frac{\delta I(t)\cdot dI'_r + \delta Q(t)\cdot dQ'_r}{dI'^2_r + dQ'^2_r} - j\frac{\delta I(t)\cdot dQ'_r - \delta Q(t)\cdot dI'_r}{dI'^2_r + dQ'^2_r}\end{aligned} \tag{4.5}$$

where dI'_r and dQ'_r can be determined from the sweep data. The first term in Eq. 4.5 is the frequency perturbation and the second term corresponds to a perturbation in the orthogonal dissipation direction (Mauskopf et al. 2014). The major advantage of this method is that it is very fast computationally only requiring a multiplication of arrays. However, a major limitation of this method arises when analysing low signal-to-noise resonances. In that case, the computation of dI' and dQ' is noisy and an accurate determination of the conversion parameters is difficult. It is also implied that the values of dI' and dQ' are constant over the range that the noise extends, which is only true when the IQ circle is large with respect to the noise ellipse.

Phase Method

The second method has been well documented (Gao 2008) and is more general. Although more computationally intensive, it takes into account the shape of the resonant feature which is crucial when the signal causes the resonance to move a significant fraction of a linewidth. This is seen in the FTS data of Chapter 5 and this method was used to calculate the frequency shift.

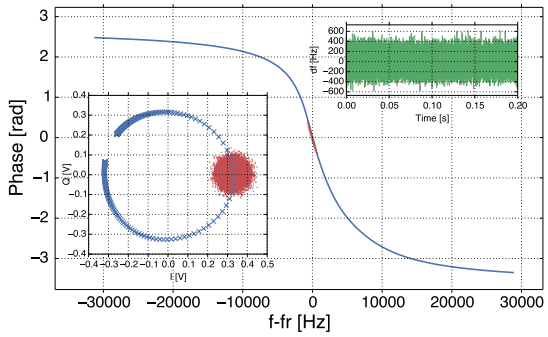

(a) KID101, $Q_r \approx 13,000$.

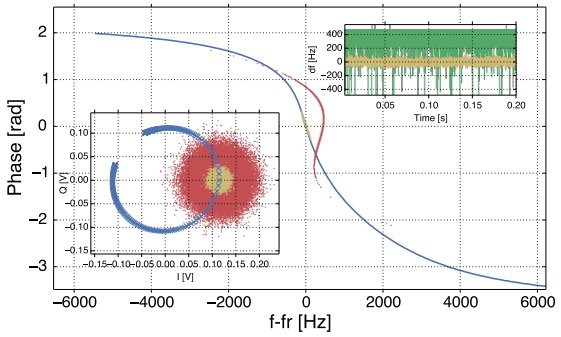

(b) KID103, $Q_r \approx 45,000$.

Figure 4.11: Examples of the phase conversion method for two resonators with different Q_r values. The reduction in Q_r permits a higher readout power, which reduces the equivalent amplifier noise level. In b) it is necessary to re-sample the timestream data (tan coloured lines) to obtain a valid fit to the phase slope. In this example, the sample rate has been reduced from 500 kS/s by a factor of 10.

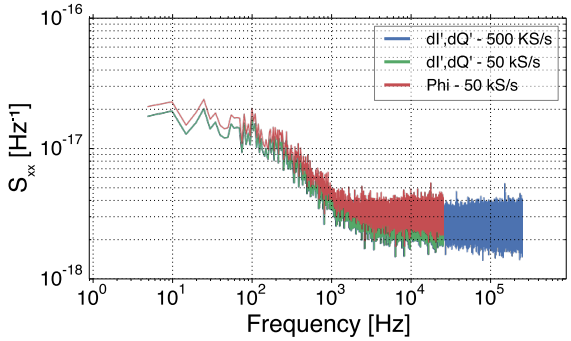

Figure 4.12: Example of fractional frequency noise of KID103. The blue and green traces are calculated using Eq. 4.5 for the fully sampled (blue) and re-sampled (green) timetrace, where the traces are identical for readout frequencies below the Nyquist frequency of the re-sampled data.

Using the same analysis algorithm that was used to estimate f_r and Q_r, the first step of the phase method of conversion is to calculate the phase from the centred and rotated complex sweep data. Applying the same translation and rotation to the timestream data, a phase for each point in the timestream can be calculated by

$$\phi(t) = \tan^{-1} \frac{Q(t)}{I(t)} \tag{4.6}$$

To convert to a frequency shift, the timestream phase points are interpolated onto the sweep data after fitting a low order polynomial to capture the shape of the sweep data. An example of the steps described above is shown in Fig. 4.11. Fig. 4.12 shows a comparison of the two algorithms for a measurement on KID103 at 230 mK. As long as there is a reasonable fit to the phase slope then the two methods are in

close agreement, with the phase method consistently returning slightly higher noise than the multiplication method. This is to be expected as the phase method accounts for the drop in response of the resonator away from the resonant frequency, whereas the multiplication method assumes a constant response, therefore underestimating the noise level. However, the discrepancy is less than a factor 1.5. For the data in the next section we use a comparison of both methods to ensure consistency in the data analysis.

4.5.2 Results and Discussion

Having a method to convert the raw timestreams of IQ data to an equivalent fluctuation in the resonant frequency, the power spectral density (PSD) of the fluctuations can now be estimated. Each PSD is an average of 50 timetraces sampled at two sample rates; 500 kHz for 0.1 s to capture the high frequency roll off, and 5 kHz for 2 s to probe the low (sub-1 Hz) frequency spectrum.

Fig. 4.13 shows a number of such measurements for a selection of resonators from the test array measured at a sample temperature of 230 mK. The shape of the spectra are all similar and consist of a low frequency level that rolls off with the resonator bandwidth to a level that is dominated by the noise of the first stage amplifier. Each spectrum is fit with a three parameter, single-pole Lorentzian of the form

$$S_x(f) = \frac{A}{1 + f^2/\Delta f^2} + B, \tag{4.7}$$

where A is an estimate of the device noise, B is an estimate of the amplifier noise and Δf is the half-width half-maximum bandwidth of the resonator. It is common to use the estimate of half-power bandwidth to infer a quasiparticle lifetime (Mauskopf et al. 2014). However, for these resonators the combination of high Q_r and low f_r obscures the roll-off of the quasiparticle response. The equivalent resonator ring down time is related to the resonator bandwidth by $\tau_{res} = 1/2\pi\Delta f_{res} = Q_r/\pi f_r$. The effect of reducing the readout frequency from the traditional GHz range reduces the resonator bandwidth, increasing the resonator ring down time.The shape of the noise is well described by a single-pole roll-off, it is reasonable to assume that the quasiparticle lifetime is at least half of the observed ring down time. As an example, KID101 is observed to have $\tau_{res} \approx 120\,\mu$s, and therefore a rough upper limit on the quasiparticle lifetime of $\approx 60\,\mu$s. For TiN quasiparticle lifetimes generally range between $10-100\,\mu$s depending on film quality (Leduc et al. 2010). The discrepancy between the values of Δf_{res} from the noise and sweep data is seen on all resonators on the device and in Table

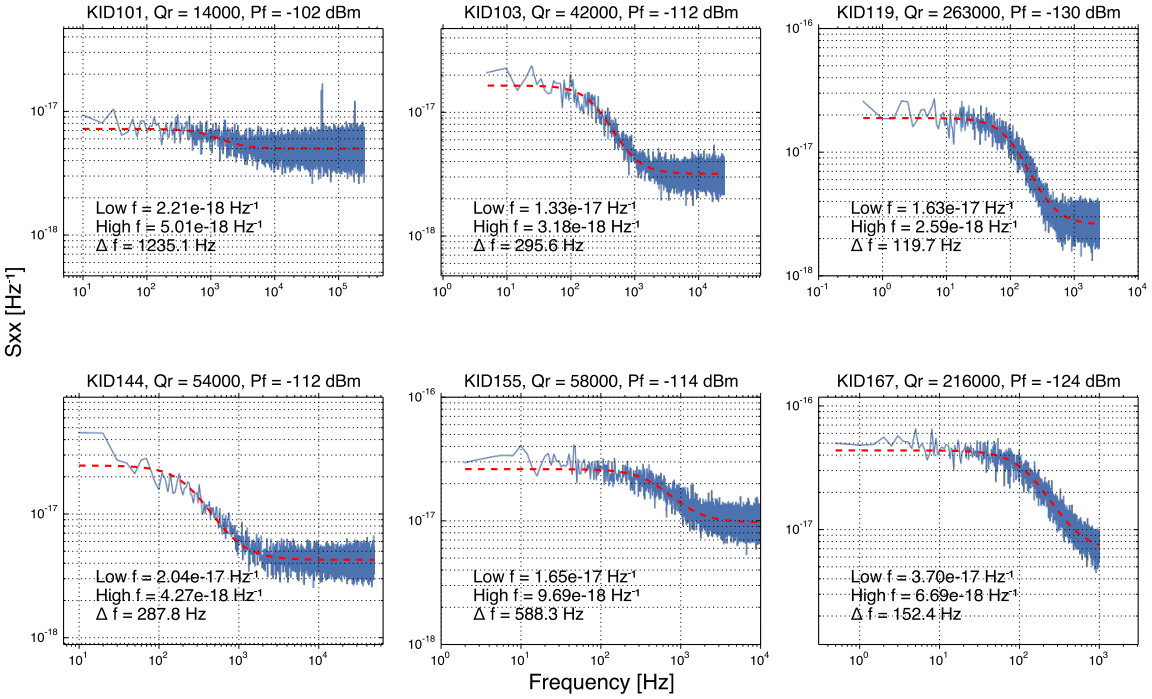

Figure 4.13: Fractional frequency noise, S_{xx} for a selection of resonators driven 2-4 dB below bifurcation at 230 mK. The values of Q_r are determined from a fit to the sweep data.

4.1, we compare the bandwidth from both measurements for a selection of resonators. It is seen that the bandwidth estimated from the noise is consistently lower than the corresponding values calculated from the sweep data by factors ranging between 2-5.

The discrepancy between the two values can be ruled out as a indication of the

Table 4.1: Comparison of resonator parameters for the data in Fig. 4.13. $L_0 = 137\,\mu\text{m}^3$

KID	$V_L[L_0]$	$Q_r[\times 10^3]$	f_r [MHz]	$-P_g$ [dBm]	Δf_{res} [kHz]	Δf_{meas} [kHz]
101	1	13.9	101.2	101	3.6	1.24
103	2	42.2	103.4	111	1.2	0.30
119	0.5	262.0	119.6	133	0.3	0.12
144	1	54.1	144.9	111	1.3	0.29
155	2	58.2	155.0	113	1.3	0.59
167	0.5	216.3	167.5	123	0.4	0.15

quasiparticle response as there doesn't appear to be a single limiting bandwidth that one would expect if it was inherent to the film. As the ratio between the values appears to be different for each resonator with no discernible relationship, it is conceivable that the origin lies in an aspect that is individual to each resonator. The most obvious candidate is the effect of the readout power used to probe each resonator. It is plausible that the non-linear feedback effects when resonators are driven close to bifurcation

power that can become important (Swenson et al. 2013).

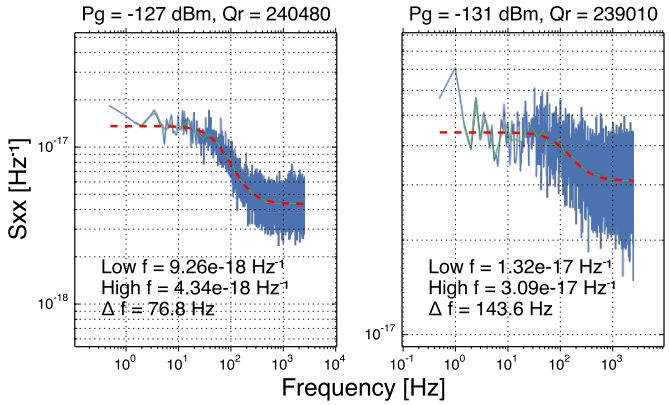

(a) KID119 - $f_r/2Q_r \approx 250$ Hz

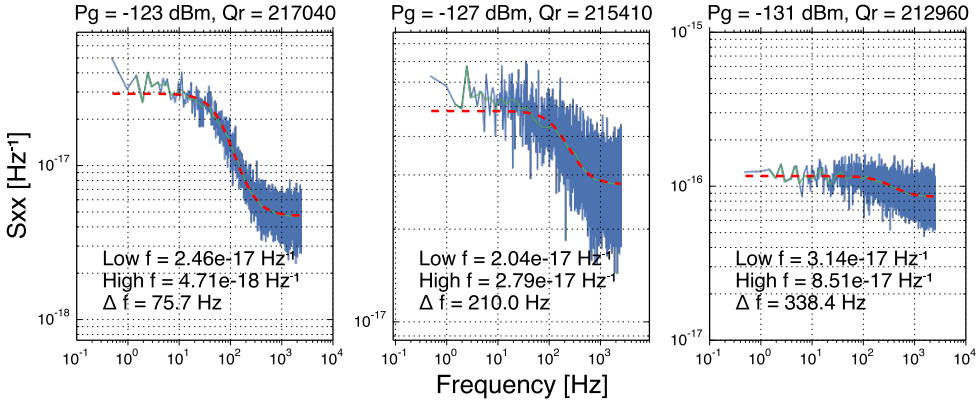

(b) KID167 - $f_r/2Q_r \approx 380$ Hz

Figure 4.14: Noise power spectral densities at different bias power.

To investigate whether or not this effect is a plausible reconciliation, Fig. 4.14 shows a set of noise for KID119 and KID167 at various drive powers. While the data is inevitably noisier, it is clear to see that as the drive power is decreased the noise bandwidth increases.

To estimate the expected GR contribution to the measured noise, the expressions developed in Chapter 2 can be applied. At low frequency, the spectral density of the number fluctuations is given by $S_{gr} = 4N_{qp}\tau_{qp}$. Multiplying this by the quasiparticle responsivity we obtain an expression for the power spectral density of frequency fluctuations;

$$S_{x,gr} = \frac{S_{gr}}{V_L^2}\left(\frac{dx}{dn_{qp}}\right)^2 = \frac{n_{qp}(T)\tau_{qp}}{V_L}\left(\alpha_k \frac{S_2(\omega,T)}{2N_0\Delta_0}\right)^2, \tag{4.8}$$

where the roll-off terms arising from the quasiparticle lifetime and resonator ring-down have been suppressed. Eq. 2.12 can be used to calculate n_{qp} and for the data in Fig. 4.13, $S_2(\omega, 0.23) \approx 4.15$. Inserting the upper limit of 60 µs placed on the

quasiparticle lifetime based on the noise bandwidth, results in an estimated value for $S_{x,gr} \approx 1 - 4 \times 10^{-20}$ depending on the choice of N_0. This is significantly lower than the noise levels measured in Fig. 4.13 and so it is most likely that the low frequency noise is limited by TLS noise. However, if a constant excess quasiparticle density of $n_{qp,min} \approx 300\,\mu\text{m}^{-3}$ is added, then the predicted nose level increases to $S_{x,gr} \approx 2.3{\times}10^{-18}$, similar to that observed in KID101. Corresponding to an equivalent temperature of about 0.3 K, it is hard to conceive the origin of such a considerable excess density. Moreover, calculation of the loss associated with this number of excess quasiparticle results in a limiting value of $Q_i \approx 0.8 \times 10^6$, for which higher values have been observed (cf. Fig. 4.4). That being said, it is not inconceivable that there is a smaller excess density and the enhanced responsivity due to the non-linear effects increase the observed noise level. To confirm whether or not this is the case, further investigation would require an alternative device. The design of the current device results in there being a small range of drive powers for which the resonator remains in the linear regime but is driven with enough power to overcome the amplifier noise.

Table 4.2: Comparison of measured noise levels with theoretical estimates. Errors in the fits are typically at the $1 - 2\%$ level for all parameters. Units for the spectral densities are in 10^{-18} Hz^{-1}.

KID [MHz]	$S_{x,HF}$	$S_{x,amp}$	$S_{x,LF}$	$S_{x,\text{TLS}}$	$S_{x,LF}/S_{x,\text{TLS}}$	NEP_{dark} [W Hz$^{-1/2}$]
101.2	5.0	4.6	2.2	2.2	1	6.8×10^{-18}
103.4	3.2	4.4	13.3	2.7	4.9	3.3×10^{-17}
119.6	5.8	18.1	16.3	13.0	1.3	9.2×10^{-18}
144.9	4.3	3.4	20.4	4.4	4.6	2.1×10^{-17}
155.0	9.7	4.3	16.5	3.1	5.3	3.7×10^{-17}
167.5	7.0	3.9	37.0	12.2	3.0	1.4×10^{-17}

4.5.3 Electrical NEP Estimate

The Noise Equivalent Power (NEP) is a common figure of merit used to characterise sub-mm detectors. The NEP is defined as the signal power required to achieve a unity signal-to-noise ratio measured in a 1 Hz post-detection bandwidth. The dark NEP refers to power absorbed referenced at the detector. The optical NEP is a measure of the optical response and is referenced at the input of the system and includes the overall system optical efficiency.

In this section we calculate an estimate of the dark NEP, which can be calculated from

the spectral density of the frequency fluctuations divided by the responsivity,

$$\mathrm{NEP}_{\mathrm{freq}} = \sqrt{S_x}\left(\frac{dx}{dP_{abs}}\right)^{-1} \tag{4.9}$$

$$= \sqrt{S_x}\left(\frac{dx}{dn_{qp}} \cdot \frac{dn_{qp}}{dP_{abs}}\right)^{-1}. \tag{4.10}$$

where S_x is the measured noise spectral density in units $\Delta f/f_r/\mathrm{Hz}^{1/2}$. Recalling the expression for the change in quasiparticle density for a given change in absorbed power,

$$\frac{dn_{qp}}{dP_{abs}} = \frac{\eta_o \tau_{qp}}{V_L \Delta_0}, \tag{4.11}$$

we obtain

$$\mathrm{NEP}_{\mathrm{freq}} = \sqrt{S_x}\left(\frac{dx}{dn_{qp}} \cdot \frac{\eta_o \tau_{qp}}{V_L \Delta_0}\right)^{-1}. \tag{4.12}$$

For the dark NEP a value measured value for dx/dn_{qp} can be determined from the sweep data as a function of the base temperature. Fig. 4.15 shows a plot of the fractional frequency shift as a function of thermal quasiparticle density. As discussed above, the measured thermal quasiparticle responsivity is a function of the base temperature, with two limiting values at the temperature extremes. Linear fits to the data in the two limits are shown in Fig. 4.15 and indicate a factor ≈ 7 decrease in responsivity at high quasiparticle density.

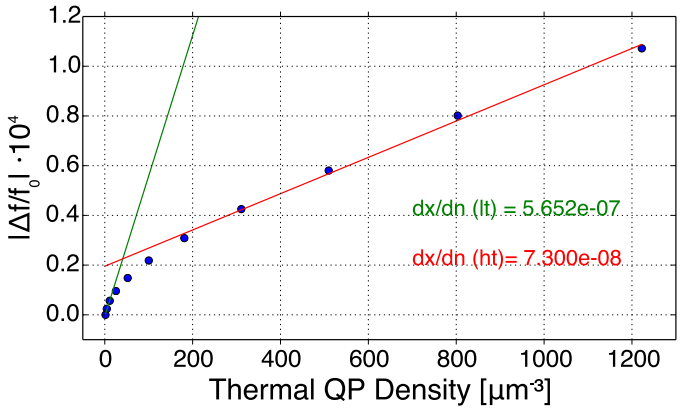

Figure 4.15: Fractional frequency shift due to a change in base temperature.

For $T_c = 2.1$ K, resonator volume $V_L = 137\,\mu\mathrm{m}^{-3}$ and assuming an upper limit for the quasiparticle lifetime of 60 µs the estimated measured dark NEP$\approx 7 \times 10^{-18}$ $\mathrm{WHz}^{-1/2}$. Estimated dark NEPs for the other resonators in Fig. 4.13 are calculated in the same way and are given in Table 4.2.

The dark NEP can be used as an estimate the performance of a detector relative to

the expected background noise level. However, care should be taken as the effect of optically loading a resonator can potentially significantly modify the resonator parameters.

4.5.4 Temperature Dependence

For the final part of the dark characterisation we investigate the noise as function of temperature. As noted before, the different contributions to the noise have differing temperature dependencies and can be used to diagnose the dominant source of the noise. Noise spectra for KID101 and KID167 for various base temperatures are shown in Figs. 4.16 and 4.17. The base temperature was regulated by a simple PID controller and kept the temperature constant to within ± 1 mK of the set point throughout each measurement. The drive power was kept constant for each resonator and set to -101, -124 dBm for KID101, KID167, respectively.

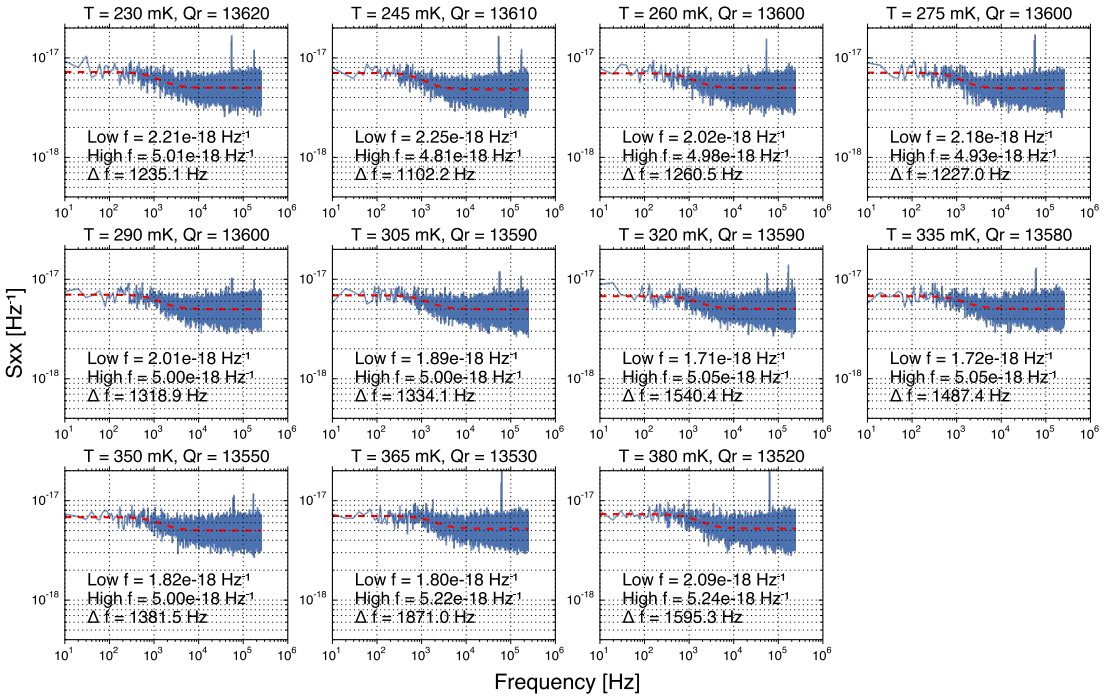

Figure 4.16: Fractional frequency noise, S_{xx} of KID101 as a function of base temperature ranging from 230 - 380 mK in 15 mK steps. The drive power was set to -124 dBm for each temperature. Errors in the parameters extracted from the fits are typically between $1-5\%$.

The shape and levels of the spectra for KID101 stay roughly constant as the temperature is increased. The high frequency level is accurately predicted by the calculation of the amplifier noise level and the slight increase at the highest temperatures is due

to the change in Q_r as Q_i decreases. To within experimental error there appears to be no evidence of a temperature dependence, expected to follow $S_{x,\mathrm{TLS}} \propto T^{(-1.5-2)}$ or the characteristic $f^{-0.5}$ frequency dependence, which although not shown here, remains flat down to below 1 Hz. Furthermore, the the spectra in Fig. 4.14a do not exhibit the expected power dependence of $P_{int}^{-0.5}$. At higher base temperatures the noise bandwidth begins to increase more than is suggested by the measured values of Q_r from the sweep data. Qualitatively this is consistent with the reduction in the effect of nonlinearities as the number of quasiparticles increase with temperature. As noted in the previous section, a constant noise level with temperature is one of the hallmarks of GR noise, and with the addition of a realistic excess quasiparticle distribution is in close agreement with the Mattis-Bardeen prediction. However, to conclusively determine whether the noise is dominated by a GR contribution a measure of the quasiparticle lifetime limited bandwidth is needed, requiring further investigation.

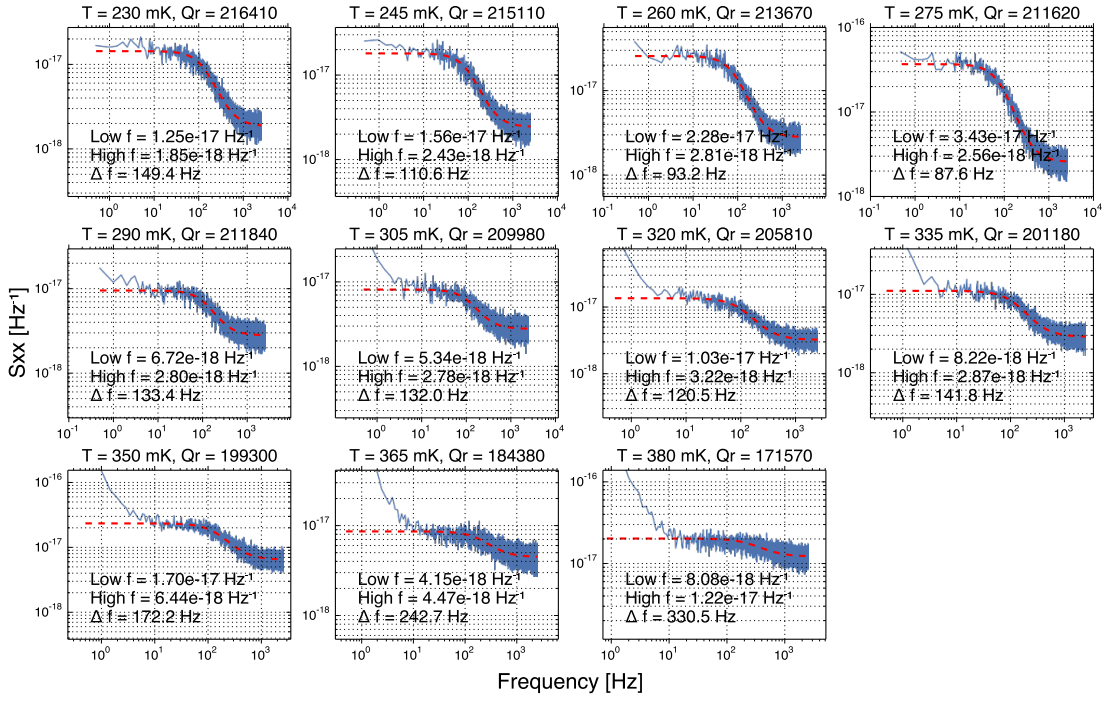

Figure 4.17: Fractional frequency noise, S_{xx} of KID167 as a function of base temperature ranging from 230 - 380 mK in 15 mK steps. The drive power was set to -124 dBm for each temperature. Errors in the parameters extracted from the fits are typically between $5-10\%$.

The spectra for KID167 are shown in Fig. 4.17 and somewhat different. The high Q_r limits the maximum drive power resulting in a low signal-to-noise measurement and can cause a significant uncertainty in the frequency conversion. A useful check can be made by comparing the measured amplifier noise level to the expected level given Q_r from the sweep for each temperature. The expected amplifier noise for $Q_r = 216$k

at $P_g = -124$ dBm is $(3.3 \pm 1) \times 10^{-18}\,\mathrm{Hz}^{-1}$, which isn't too far from the measured values. The error is estimated assuming a ± 1 dB uncertainty on the input power, and is likely to be an underestimate.

It is reasonable to assume that the device noise in this case is dominated by TLS in spite of the lack of conventional TLS signatures. At low temperature, the low frequency noise level remains flat to below 1 Hz. Above 270 mK, a clear 1/f component appears in the spectra with a knee frequency that appears to be temperature dependent. Unfortunately the resolution of the PSD is limited by the length of the timestream but it seems reasonable that at low temperature, the 1/f knee falls below the resolution limit of the PSD.

4.6 Chapter Summary

This chapter presents a dark characterisation of the SuperSpec titanium nitride resonators. The design and measured values of the spectrometer array are in close agreement yielding consistent values of the resonant frequency and coupling quality factors, as well as measured values of Q_i consistently above 10^6. A systematic variation in the film properties has been identified by comparing the frequency shift and change in quasiparticle dissipation as a function of temperature to a prediction based on a first order approximation of the Mattis-Bardeen equations. Using this prediction we also measure an anomalously low response in the dissipation direction. Based on the observed power dependence we attribute this to a limiting loss that is most likely due to a contribution from TLS fluctuations.

Utilising the range of resonator designs available on the test array, we investigate the noise properties of the film. It is most likely that TLS noise is the dominant source of noise for the majority of the detectors, despite the form of the spectra not reflecting the conventional form commonly measured at microwave frequencies. Resonators that can be driven at higher power such that the TLS contribution is suppressed show behaviour that is consistent with a measurement of GR noise. However, a definitive conclusion can't be made without a measure of the quasiparticle lifetime, which for we can only obtain an upper limit due to the resonator ring down time. From spectra on a selection of resonators driven just below bifurcation, estimates of the dark NEP using the measured responsivity to quasiparticles are made and yield an average value of $\approx 3 \times 10^{-17}\,\mathrm{WHz}^{-1/2}$.

Chapter 5

Optical Demonstration of SuperSpec

In this Chapter we present preliminary optical measurements and a spectral characterisation of a prototype SuperSpec device. The specific device is a different die from the same wafer as the device characterised in Chapter 4. We begin with the characterisation of the detectors following the methodology outlined in the previous chapter, followed by a description of the measurement setup used to characterise the spectral response of the spectrometer. Finally we make a comparative estimate between the expected response to a change in blackbody load and based on the observed detector responsivity, calculate an estimate of the system noise equivalent power (NEP).

5.1 Array Characterisation

Initially a characterisation of the array from an RF perspective is necessary to ascertain the resonant frequencies of the resonators and confirm that the array is working as expected. The main results are shown in Fig. 5.1 and are quantitatively similar to the device presented in Chapter 4. After applying a linear scaling as before, the distribution in frequency is in good agreement with the design values, and allows identification of specific detectors and the corresponding mm-wave channel. The resonator yield is again high with only a single resonator absent. Upon inspection of the device, it was found that there was a break in the interdigital capacitor which would cause the resonant frequency to shift out of the readout band.

The distribution of the resonator quality factor is again similar to the previous chapter showing values of Q_i consistently above 10^6. As before, the observed bimodal

distribution of Q_c is related to the difference in the capacitor geometry, with the 1 µm geometry having systematically larger Q_c than the 2 µm capacitors.

Extracted T_c values from the temperature dependence of $\Delta f/f_0$ show a similar gradient across the spatial extent of the device. The average value of T_c matches with the lower end of the previous device indicating that the spatial distribution of T_c is most likely due to a gradient in the film thickness across the initial wafer.

Although not plotted here, the anomalous diminished response in the dissipation direction is similar to that of the previous devices with values of $\beta \approx 400$.

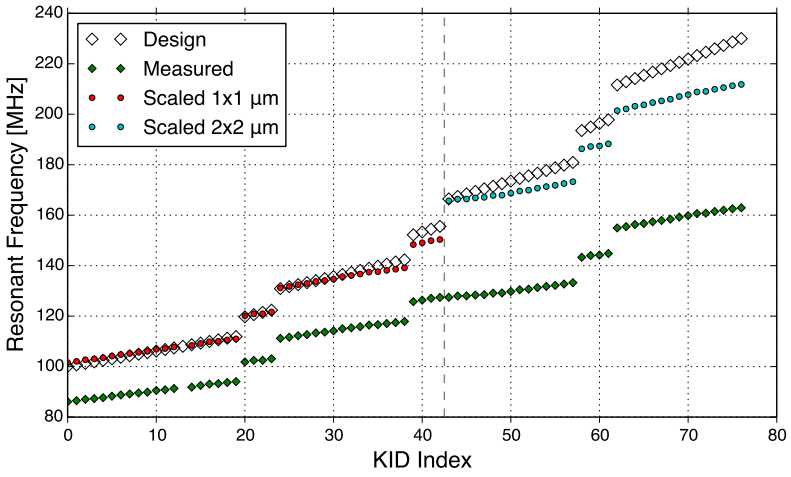

(a)

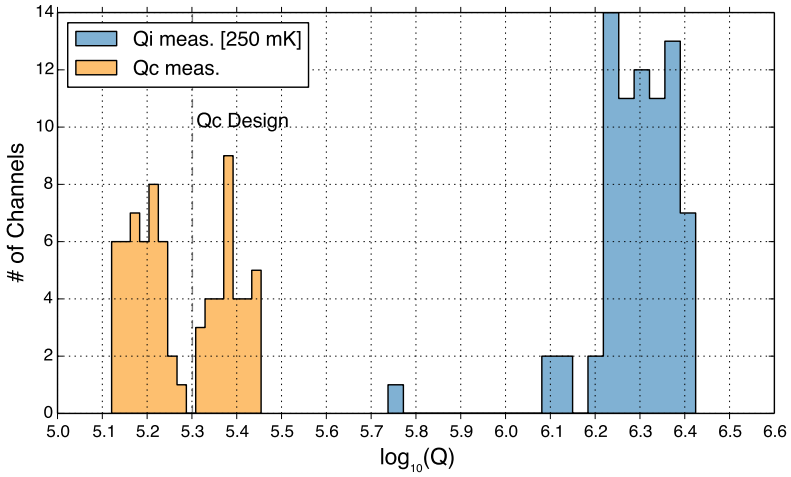

(b)

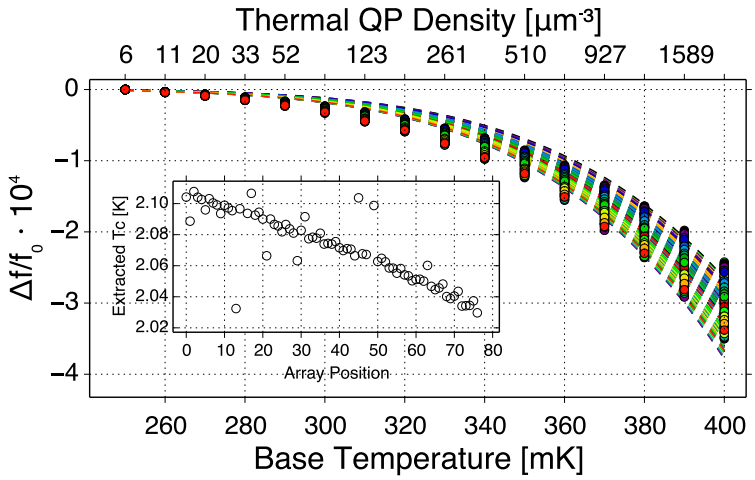

(c)

Figure 5.1: Characterisation of the resonators on the SS05-CDF03 device. a) Comparison of design versus measured resonant frequencies. b) Distribution of measured Q_i and Q_c. **c)** Measured shift in resonant frequency as a function of base temperature (points) along with fits (dashed lines) to Mattis-Bardeen prediction to extract T_c. Inset shows the distribution of extracted T_c values as a function of spatial position on the device.

5.2 Measurement Setup

5.2.1 Cryostat Configuration

A CAD model of the optics configuration used to carry out the characterisation of the filter-bank is shown in Fig. 5.3. The low pass filters on the 50 K and 4 K reduce the infrared load on the fridge, while being transparent at 1 mm. The filter profiles are plotted in Fig. 5.2. The solid line is the combined filter transmission that is seen at the horn aperture and, after including the efficiencies of the three high temperature filters, indicates a total combined filter efficiency of approximately 70%.

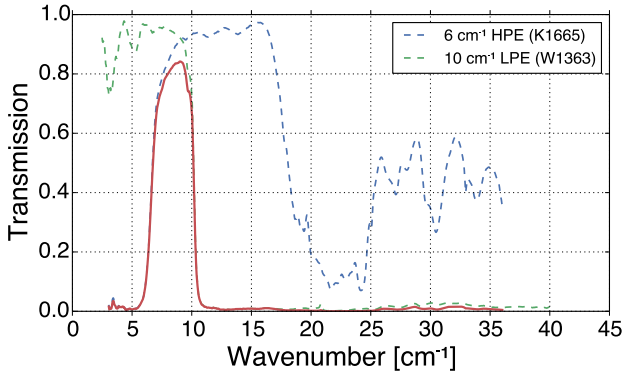

Figure 5.2: Transmission of the optical filter stack used to define the bandpass for the detector. The position of each filter is shown in Fig. 5.3.

The system throughput is limited by the aperture at 50 K. The solid angle of a cone with vertex angle 2θ is given by

$$\Omega = 2\pi(1 - \cos\theta) \approx \pi\theta^2. \tag{5.1}$$

where θ can be determined from the geometry shown in Fig. 5.3a. The width of the limiting aperture is 13 mm and is at a distance of 99 mm from the horn aperture of radius 3.3 mm. The geometric throughput can be calculated as

$$A\Omega = \pi^2 3.3^2 \left(\frac{13}{99}\right)^2 \approx 1.85\,\mathrm{mm^2 sr}. \tag{5.2}$$

For a single mode, the diffraction limited throughput is given by $A\Omega = \lambda^2$, which ranges from 1 - 2.8 mm^2 sr across the 180-310 GHz band. Above about 220 GHz, the throughput is diffraction limited such that a blackbody source at the window should fill the beam. At lower frequency, only a fraction of the beam will be filled by the window with the other fraction terminating on the blackened 4 K radiation shields.

The fraction of the beam leaving the cryostat reduces to about 70% at 180 GHz.

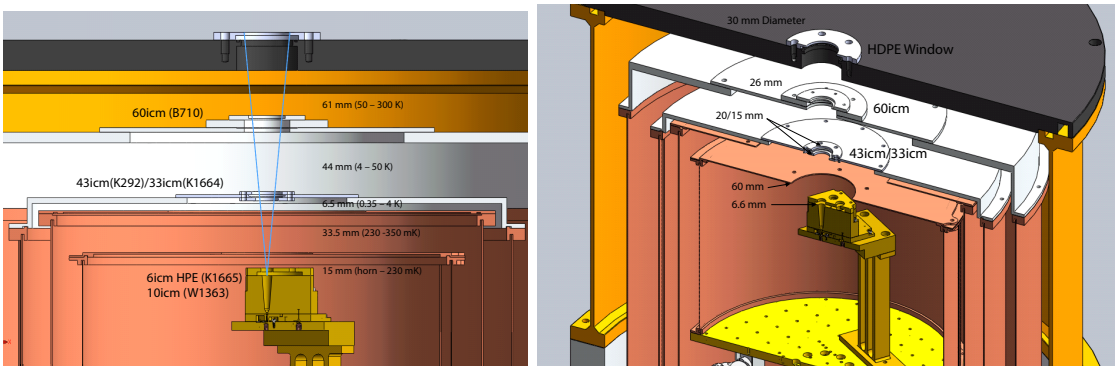

(a) Front view (b) Isometric view

Figure 5.3: CAD model of the configuration used for the optical characterisation of the filter-bank. In a) the black labels are the filter IDs at each temperature stage. All filters are low pass edges except for $6\,\mathrm{cm}^{-1}$ high-pass to form a bandpass at the horn aperture.

5.2.2 Measurement Algorithm

A similar measurement algorithm used to obtain noise data is carried out when obtaining data with the Fourier transform spectrometer (FTS); for each resonator a sweep about the resonant frequency is performed to lock on to the resonance and timestream data can be taken.

However, instead of taking a continuously sampled timestream, for the FTS measurements it is necessary to synchronise the data acquisition (DAQ) with the movement of the mirror. As the movement of the mirror is not necessarily uniform, the mirror encoder is connected to custom-built circuitry that provides a 5 V square wave pulse with every mirror step, and is used as a clock signal to trigger the DAQ. Therefore on every increment of the mirror position a DAQ sample is taken resulting in a regularly gridded interferogram as a function of mirror position. The external circuit also provides signals of the mirror direction as well as a fixed reference point, from which the interferograms can be aligned.

5.3 Filter-Bank Analysis

In this section we present spectral measurements and a characterisation of the spectral response of the filter-bank and compare to the design values given in Chapter 3. A

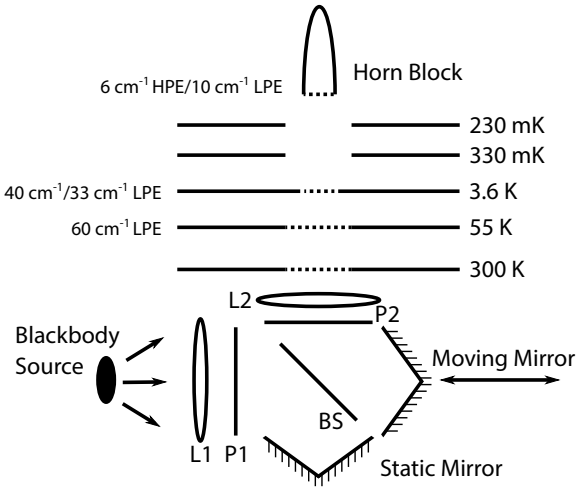

Figure 5.4: Schematic configuration for FTS measurement and characterisation.

schematic of the measurement configuration is shown in Fig. 5.4. A Martin-Puplett interferometer was used to provide a frequency sweep. A variable aperture mercury (Hg) vapour lamp ($T_{BB} \approx 1500$ K) source was placed at the focus of an HDPE lens with a focal length of 120 mm and provides a collimated beam at the input of the interferometer. A second identical lens placed at the output focuses the beam at the horn aperture. To account for possible misalignment of the cryostat radiation shields and/or uncertainty in the array height, the position of the second lens was adjustable to fine-tune the position of the focus. The FTS was mounted on a portable optics bench and could be raised with a set of lab jacks. To align the optics to the detector, we used a chopped source with the FTS mirror set to zero-path difference, and manually positioned each component in order to maximise the signal at the chopping frequency on one of the broadband detectors.

To characterise the full spectrometer an automatic measurement system was to developed to control the FTS and data acquisition into a fully integrated control program. Unfortunately a multiplexed readout system was not available that with sufficient frequency resolution to read out the high-Q_r, low frequency SuperSpec resonators. Therefore software was developed to implement single tone readout and measure each KID sequentially.

We begin by outlining the operating principle of the Martin-Puplett interferometer and then present results of from a set of spectral measurements of the full array.

5.3.1 Principles of the Martin-Puplett Interferometer

The Martin-Puplett interferometer (MPI) has a rich history in sub-mm astronomical observations (Lambert and Richards 1978; Martin and Puplett 1970). The operation of the MPI is similar to the well-known Michelson interferometer in that an input beam is split and recombined with a modulated phase shift to produce an interferogram. However, the MPI exploits and manipulates the polarisation properties of light and at sub-mm wavelengths has a number of advantages. Most notably, a wire grid polariser replaces the typical dielectric beam-splitter, and has a high and uniform modulation efficiency over a wide spectral range, with near 100% transmission/reflection for wavelengths ranging across the entire THz band (Naylor et al. 1994).

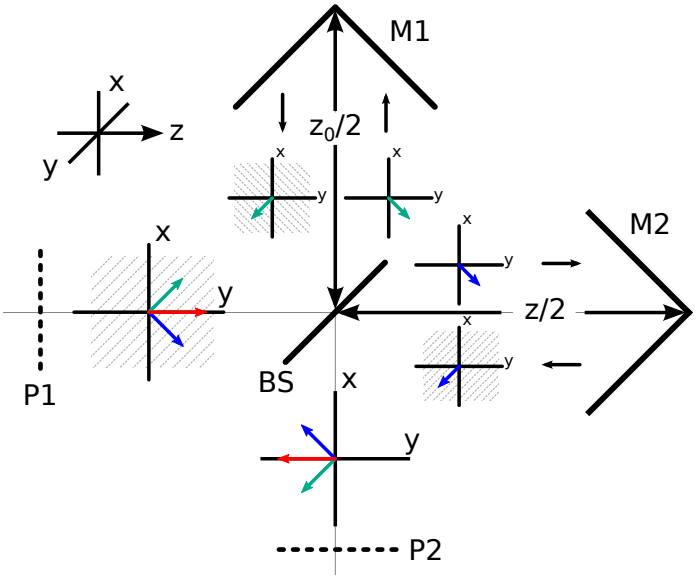

Figure 5.5: Schematic of the Martin-Puplett interferometer. The vectors are drawn from the perspective looking through the input and output polarisers along the optical axis.

The main components of the MPI are shown schematically in Fig. 5.5, and consist of and input and output polariser (P1 and P2), the polrising beamsplitter (BS) and two rooftop mirrors (M1 and M2), one of which is mounted on a translational stage (M2). The operation of the MPI can be understood by referring to Fig. 5.5. Assuming an incoherent unpolarised source such as a blackbody, P1 selects the input polarisation according to the orientation of the polarising grid lines. Subsequently, half the power is admitted into the interferometer while the other half reflects back to the source. If P1 is orientated such that the polarisation axis is along the y-axis, the electric field

vector of the input wave has the form,

$$E = \hat{y} E_0 \sin\left(\frac{2\pi ct}{\lambda}\right). \tag{5.3}$$

The wire-grid beam splitter consists of another polariser that is orientated at an angle $\theta = 45\,\text{deg}$ relative to the input polariser. Decomposing the incident electric field into orthogonal components relative to the BS orientation, the component perpendicular to the grid lines will be transmitted by the beam splitter, whereas the parallel component is able to induce currents along the direction of metallic grid and will be reflected, gaining the usual π phase shift. The electric fields of the reflected and transmitted waves are then given by

$$E_t = (\hat{y} - \hat{x})\frac{E_0}{\sqrt{2}} \sin\left(\frac{2\pi ct}{\lambda}\right) \tag{5.4}$$

$$E_r = (\hat{x} + \hat{y})\frac{E_0}{\sqrt{2}} \sin\left(\frac{2\pi ct}{\lambda} + \pi\right). \tag{5.5}$$

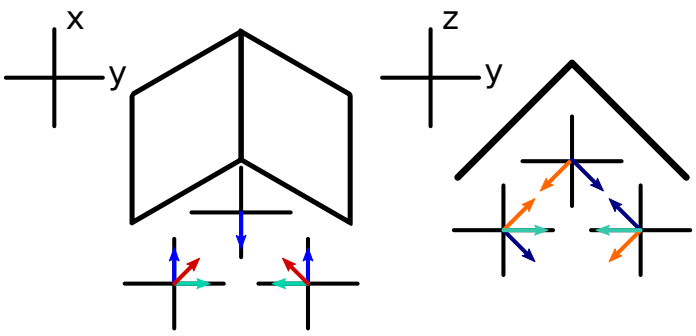

Figure 5.6: Schematic demonstrating the effect of the rooftop mirror on the polarisation.

Each rooftop mirror consists of two flat mirrors aligned at right angles such that radiation incident in the plane normal to the mirror surface is reflected back along the direction from which it came. The effect of the rooftop mirrors on the polarisation is best understood by decomposing the incident electric field into components that are parallel and normal to the mirror line and is shown schematically in Fig. 5.6. For the parallel component, reflection from the two mirrors results in a 2π phase shift and the polarisation is unaffected (blue vectors). The normal component (green) can be further decomposed into components normal (navy) and tangential (orange) to the mirror surface. Upon reflection of the first mirror, only the tangential component of the polarisation is reversed. At the second mirror, the previous normal and tangential

components are interchanged and again, only the tangential component experiences a phase shift. The net effect of the two reflections is that, relative to input, the polarisation direction is now reversed (red). Putting this together for an incident beam with polarisation vector orientated at an angle θ to the mirror line, only the horizontal component is reversed resulting in a net change of 2θ about the mirror line. Therefore, upon reflection from rooftop mirrors, the polarisation of the beams in the two arms is switched and the component originally reflected by the beam splitter is now transmitted, and vice versa. Including the additional phase shift due to the optical path lengths along each arm, z_0 for the fixed path, and z for the variable path, the electric field vector incident on the beam splitter becomes

$$E_t' = (\hat{x} + \hat{y})\frac{E_0}{\sqrt{2}} \sin\left(\frac{2\pi(ct - z)}{\lambda}\right) \tag{5.6}$$

$$E_r' = (\hat{x} - \hat{y})\frac{E_0}{\sqrt{2}} \sin\left(\frac{2\pi(ct - z_0)}{\lambda} + \pi\right). \tag{5.7}$$

The total electric field incident on the output polariser is the sum of the two electric fields emerging from the beamsplitter and after including the π phase shift for the reflected component becomes,

$$E_{tr} + E_{rt} = (\hat{x} + \hat{y})\frac{E_0}{\sqrt{2}} \sin\left(\frac{2\pi(ct - z)}{\lambda} + \pi\right) \tag{5.8}$$

$$+ (\hat{x} - \hat{y})\frac{E_0}{\sqrt{2}} \sin\left(\frac{2\pi(ct - z_0)}{\lambda} + \pi\right) \tag{5.9}$$

Rearranging and grouping terms for each polarisation direction we obtain an expression for the total electric field incident on the output polariser,

$$\begin{aligned} E_{\text{tot}} = \hat{x}\frac{2E_0}{\sqrt{2}} \sin\left(\frac{\pi(2ct - z - z_0)}{\lambda} + \pi\right) \cos\left(\frac{\pi(z - z_0)}{\lambda}\right) \\ + \hat{y}\frac{2E_0}{\sqrt{2}} \cos\left(\frac{\pi(2ct - z - z_0)}{\lambda} + \pi\right) \sin\left(\frac{\pi(z - z_0)}{\lambda}\right). \end{aligned} \tag{5.10}$$

Note that this is in general a circularly polarised wave. The effect of output polariser is to select one component of the total field which results in a modulation of the measured electric field as a function of the mirror position.

5.3.2 Spectral Analysis

The half-wavelength single pole filter is expected to result in a Lorenztian profile in the frequency domain. It is well known that mathematically, the Fourier transform

of a Lorenztian is given by an exponentially damped sinusoid. As the maximum of the interferogram is at ZPD, the expected form of the interferogram can be written as

$$f(x) \sim e^{-x/\tau} \cos(2\pi\nu_0 x). \tag{5.11}$$

The definition of the Fourier transform can be written as

$$F(\nu) = \int_{-\infty}^{\infty} f(x) e^{-j2\pi\nu x} dx, \tag{5.12}$$

and for a cosinusoidal signal $f(x) \sim \cos(2\pi\nu_0 x)$ the Fourier transform can be calculated to give

$$\begin{aligned} F(\nu) &= \frac{1}{2}\int_{-\infty}^{\infty} e^{-j2\pi(\nu-\nu_0)x} dx + \frac{1}{2}\int_{-\infty}^{\infty} e^{-j2\pi(\nu+\nu_0)x} dx \\ &= \frac{1}{2}\left[\delta(\nu-\nu_0) + \delta(\nu+\nu_0)\right], \end{aligned} \tag{5.13}$$

which is a pair of delta functions at $\pm\nu_0$ as expected. A similar analysis can be carried out for an exponential decay $f(x) \sim e^{-x/\tau}$ resulting in the expected Lorentzian lineshape;

$$F(\nu) = \frac{\tau}{1 + j2\pi\nu\tau}. \tag{5.14}$$

Using these results, and making use of the convolution theorem, the Fourier transform of the exponentially damped cosine signal is then given by

$$F(\nu) = \frac{2\tau}{1 + j2\pi(\nu-\nu_0)\tau} \rightarrow |F(\nu)|^2 = \frac{4\tau^2}{1 + (\nu - \nu_0/\Delta\nu)^2}, \tag{5.15}$$

where $\Delta\nu = 1/2\pi\tau$ is the half-width half-maximum bandwidth, and the factor 2 of arises from taking only positive frequencies. Therefore the filter resonant frequency is given by ν_0, and the quality factor can be calculated from the decay of the fringe visibility by

$$Q_{\text{filt}} = \nu_0/2\Delta\nu = \nu_0\pi\tau, \tag{5.16}$$

where both ν_0 and τ can be obtained from a fit to Eq. 5.11 to the interferogram data.

The maximum operating frequency of an FTS is governed by Nyquist sampling theorem and determined by the minimum step size of the mirror translation stage. For the MPI used in this thesis the physical step size of the motor is specified as 5 μm, which corresponds to

$$\nu_{\max} = \frac{c}{2 \times (2 \times 5\,\mu\text{m})} \approx 15\,\text{THz}, \tag{5.17}$$

well above the requirements for characterisation of the device described in this thesis.

The maximum spectral resolution is determined by the maximum available phase retardation and is set by the travel length of the mirror. For our system, the maximum optical path difference is 48 cm resulting in a maximum resolution of (Bin et al. 1999)

$$\Delta\nu = \frac{c}{2 \times \mathrm{OPD}_{\mathrm{max}}} \approx 310\mathrm{MHz}, \tag{5.18}$$

which is close to the expected bandwidth for high-Q filter channels. For example, an $\mathcal{R} = 700$ channel at 200 GHz has a filter bandwidth of ≈ 300 MHz. Therefore, it is expected that the measurements of filter channels with high-Q will be limited by the FTS resolution.

5.3.3 Data Analysis and Discussion

Analysis of the data taken with the FTS is similar to the analysis of the noise data. An equivalent frequency shift is calculated from the complex timestream data by using the sweep data as a calibration to convert from phase to frequency. Fig. 5.7 shows a representative example of this process along with the resulting interferogram expressed in units of equivalent shift in the KID resonant frequency.

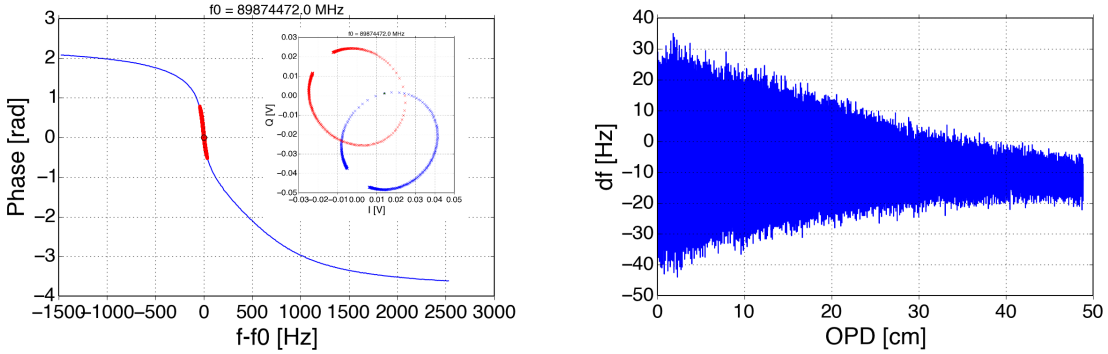

(a) (b)

Figure 5.7: a) Calibration data used to convert the raw IQ data to an equivalent frequency shift. Blue curve is the phase relative to the centre of the IQ circle, red points are the interpolated timestream data. b) Example of the raw interferogram data taken for a single scan of the mirror. Note that the oscillations are not visible at this zoom level.

It can be seen that there is a shift in the baseline level with increasing optical path difference. This is most likely due to a misalignment of the FTS optics and a simple

baseline removal consisting of a high-pass filter was applied to each interferogram before continuing. Care was taken to ensure that the cut-on frequency of the high-pass was well below the frequencies corresponding to the optical bandwidth of the spectrometer.

For the narrow-band filter channels, the interferogram was cut at zero path and fit to a modified version of Eq. 5.11 to account for an arbitrary signal level and phase offset. The results of four representative filter channels are shown in Fig. 5.8. The resulting spectra are obtained by taking the magnitude of the Fourier transform at positive frequencies of the interferogram data.

The form of the interferogram and spectra are as expected. The interferogram data are well fit to the damped harmonic wave model. The apparent discrepancy between the model and fit for the zoomed out plots is partially a graphical artefact, and partially an increase in noise due to the reduced detector response at large signal power. The insets show the data zoomed in around zero-path difference and highlight the quality of the fit.

Each spectrum consists of a single peak that is well characterised by a spectral Lorentzian profile. The out of band band response is consistently measured at the 1% level with high spectral purity within our optical band. There are however a number of channels that show a small amount out of band response (e.g. first plot in Fig. 5.8), and indicate that a certain level of parasitic power is coupling into the detector. The cause of this has not yet been identified, but on further analysis it is found that the filter channels on which this effect is most pronounced are located close to the probe, suggesting a non-negligible amount of power transfer through substrate modes. However, the effect is not seen by all channels near the probe and it is hard to imagine substrate leakage would discriminate between different resonators.

The normalised spectra of a broadband power channel along with the first termination channel is shown in Fig 5.9. The broadband channel is located at the input of the spectrometer before any of the filter channels and so provides an estimate of the total power that enters the filterbank. The bandpass frequencies of the measured spectral band are in good agreement with the expected filter response, which serves as confirmation that there are no major issues in the analysis algorithm.

The shape of the in-band response however is not well understood, and is difficult to identify the cause as it could arise from a number of factors. The most likely cause is an effect introduced by the waveguide to microstrip transition, which has not been independently verified at cryogenic temperatures.

The spectra of the terminator channel is shown in Fig. 5.9b alongside all the measured

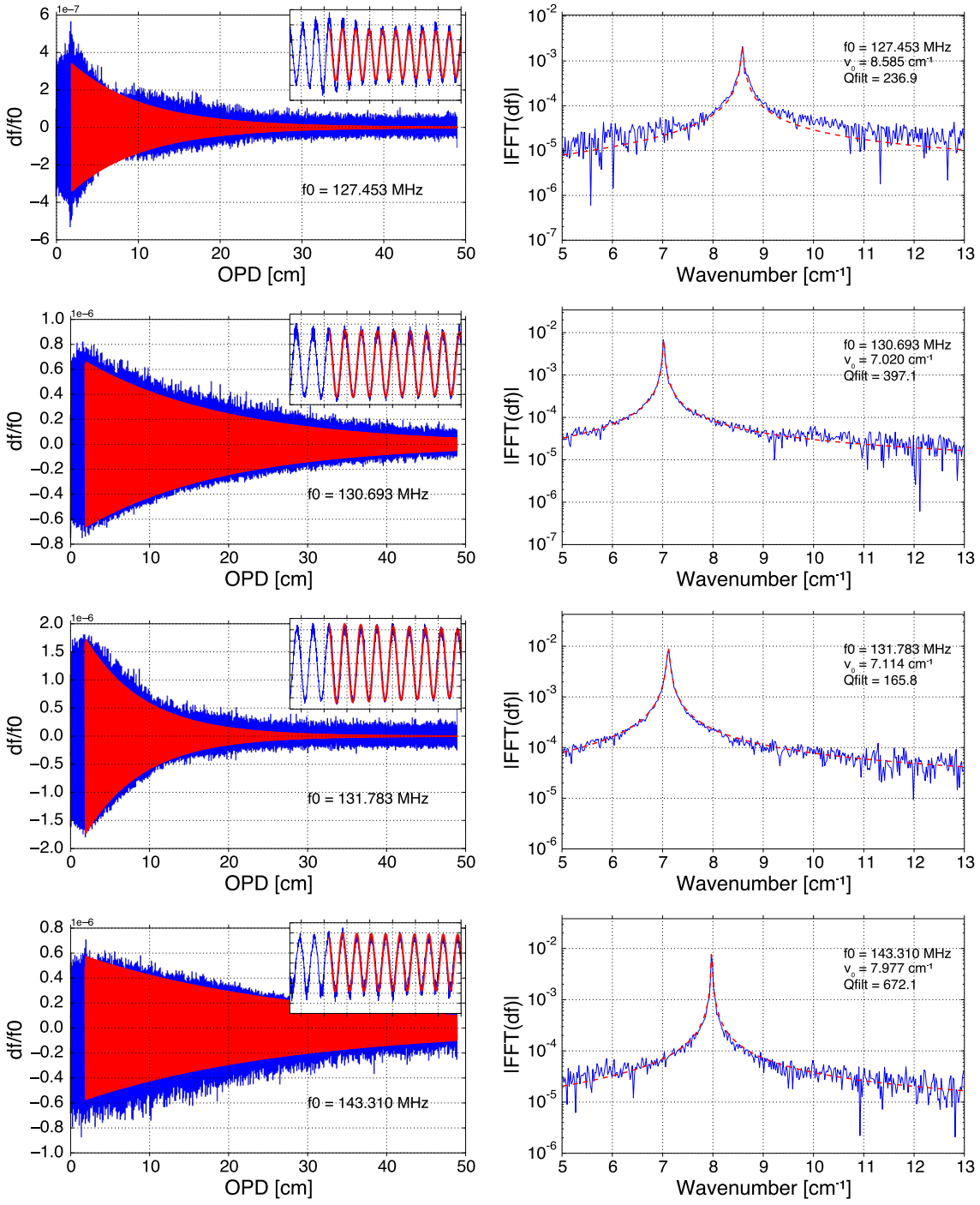

Figure 5.8: Interferogram data (left) and the resulting spectra (right) for four narrow band filter channels that are representative for the rest of the channels. Fits to the interferograms are shown in red and show good agreement for all the channels (see insets). Values extracted from the fit are given in the plot of the spectral data.

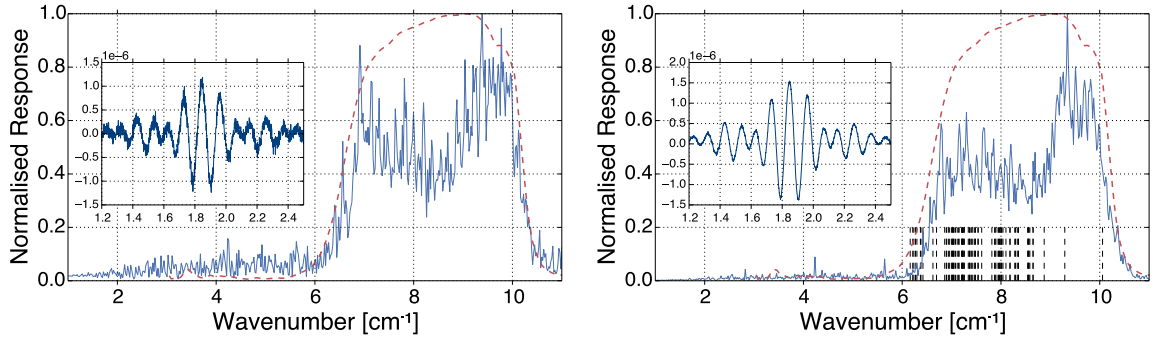

(a) (b)

Figure 5.9: Comparison of the spectrum of two of the broadband channels. The channel shown in a) corresponds to the broadband absorber located at the input of the filter-bank, i.e. before any filter channels. In b), the channel corresponds to the first of the four termination absorbers located at the end of the feedline.

filter frequencies (black dashed lines). The difference between the broadband and termination channel would ideally be a measure of the absorption due to the filterbank. The shape of the two broadband spectra are similar except for a reduced response at the low end. There is no discernible reduction of power in the spectrum at the measured filter frequencies. However, this is expected to be a small effect that would require a high-resolution frequency sweep to measure accurately. Unfortunately, we did not have access to a reliable high-frequency LO source at the time to conduct a high resolution characterisation. However, this will be done in future measurement and should provide a measure of the power absorbed by the detector which is valuable for placing limits on the accuracy of the filter placement and bandwidth.

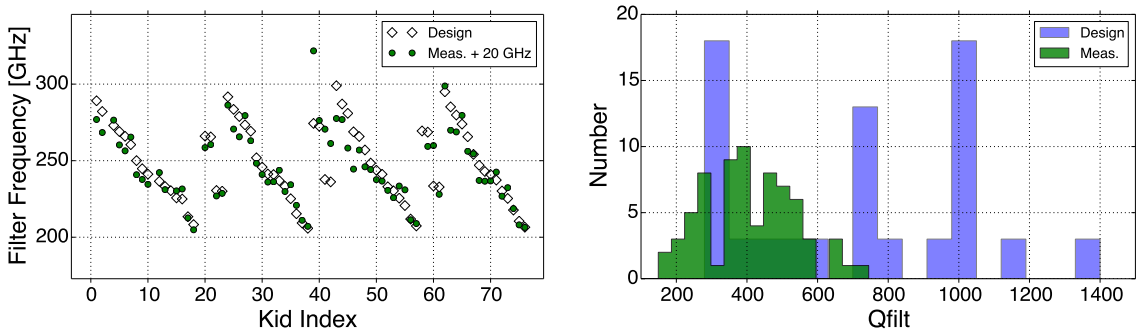

(a) (b)

Figure 5.10: Comparison of the measured and design filter values for a) ν_0 and b) Q_{filt}.

A comparison of the measured to designed distribution of filter quality factors for the entire array is shown in Fig. 5.10b. We see that the measured values are distributed about a mean value of about $Q_{\text{filt}} \approx 400$ with a maximum measured $Q_{\text{filt}} \approx 700$. The low mean value of Q_{filt} indicates an internal loss mechanism that restricts the

bandwidth of the filters. Assuming the design values for $Q_{\rm det}$ and $Q_{\rm feed}$, a fit to Eq. 3.2 yields an estimate of the measured Q_i for this device. This assumption is supported by the fact we achieve the target values for many filters with $Q_{\rm filt} < 500$. A comparison of the measured and designed values of $Q_{\rm filt}$ for the first 20 readout channels along with the fit is shown in Fig. 5.11.

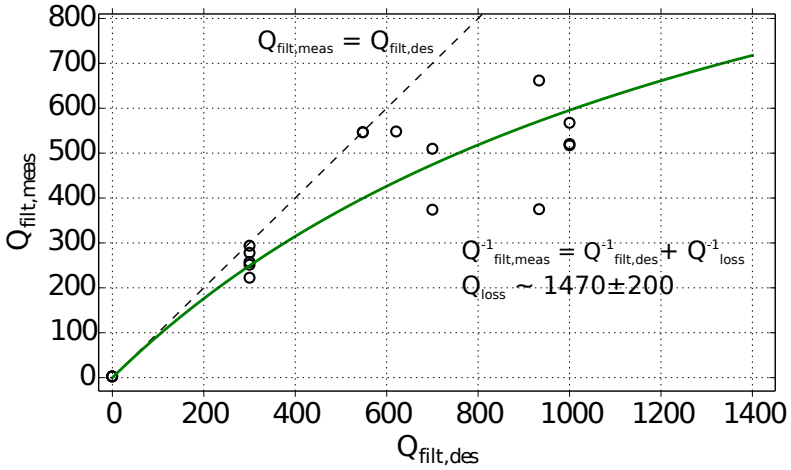

Figure 5.11: Comparison of the measured and designed $Q_{\rm filt}$ for the first 20 readout channels.

It is expected that the dominant loss in the filter arises from the silicon nitride microstrip dielectric layer (Hailey-Dunsheath et al. 2014). From the best fit estimate of $Q_i \approx 1470$ we infer a $\tan\delta = Q_i^{-1} \approx 7 \times 10^{-4}$ which is in good agreement with independently published measurements (O'Connell et al. 2008).

Alternatively, it is plausible that the frequency resolution is limited by the spectrometer. As calculated before, the maximum achievable resolution for our MPI corresponds to a maximum filter $Q \approx 700$. However, misalignments in the focusing optics, or within the interferometer act to reduce the spectrometer resolution. An independent measurement with a high frequency resolution LO source would determine which effect is dominant.

5.4 Blackbody Response

The response to a change in static loading between a room temperature and liquid nitrogen load (77 K) provides a measure of the response of all of the channels on the spectrometer that can be measured simultaneously. By sweeping each resonator, once while viewing a liquid nitrogen load, and again with a room temperature load, the shift in resonant frequency due to the change in absorbed power can be determined. This

response can be then compared with the expected response from the Mattis-Bardeen expressions derived in Chapter 2, and with a few assumptions, an estimate for the system efficiency can be obtained.

Generally, an estimate of the power absorbed in the detector requires knowledge of a number of factors; the spectral emission of the source, the filter transmission efficiency as well as various efficiency factors inherent to the filterbank design. However, we can make an estimate of the expected power that reaches the horn aperture, and assuming negligible loss originating from the horn and waveguide transition, the power entering the filterbank.

The spectral emission from a blackbody in the Rayleigh-Jeans limit ($h\nu \ll k_{\mathrm{B}}T$) is given by

$$B_\nu(T) = \frac{2k_{\mathrm{B}}T}{\lambda^2}, \tag{5.19}$$

in units of W m^{-2} sr^{-1} Hz^{-1}. For a single spatial mode, single polarisation where $A\Omega = \lambda^2$, the power emitted by an area A into solid angle Ω is then given by

$$P_o = \frac{2k_{\mathrm{B}}T\Delta\nu}{\lambda^2} \cdot A\Omega = k_{\mathrm{B}}T\Delta\nu, \tag{5.20}$$

i.e. the optical power is proportional to the source temperature and the optical bandwidth. In our case, the optical bandwidth will depend on the specific filter channel. For the broadband absorbers situated along the length of the feedline as well as the termination channels, the bandwidth will be determined by primarily by the bandpass at the input of the horn, which from Fig. 5.2 is approximately 120 GHz.

For the filter channels, the situation is less simple and depends on both the matching of the filter and the proximity of adjacent filters in frequency space. From a simple circuit model, the fraction of the power on the feedline that is terminated in the detector is given by (Hailey-Dunsheath and Shirokoff 2014)

$$\eta_{\mathrm{det}} = 2\frac{Q_{\mathrm{filt}}}{Q_{\mathrm{feed}}}\left[1 - \frac{Q_{\mathrm{filt}}}{Q_{\mathrm{feed}}} - \frac{Q_{\mathrm{filt}}}{Q_{\mathrm{loss}}}\right]. \tag{5.21}$$

Assuming that $Q_{\mathrm{loss}}^{-1} = 0$, $Q_{\mathrm{filt}}^{-1} = Q_{\mathrm{det}}^{-1} + Q_{\mathrm{feed}}^{-1}$, where the terms are defined in Sec. 3.2. For a matched filter isolated in frequency, $Q_{\mathrm{det}} = Q_{\mathrm{feed}} = 2Q_{\mathrm{filt}}$ and the expected filter bandwidth is given by $\Delta\nu = \nu_0 Q_{\mathrm{filt}}^{-1}$. In this case $\eta_{\mathrm{det}} = 50\%$, as expected, but can be significantly less for a mismatched filter.

In Table 5.2 we calculate the expected change in in-band power on the feedline due to a 300 - 77 K chop for a number of filter design parameters. We assume a negligible contribution to the in-band power originating from the thermal emission of the optical

filters. Therefore the power estimate will likely be an underestimate of the total loading. We have also assumed, following the discussion in Section 5.2, that the blackbody fills the beam, which is likely only true at higher frequencies. As mentioned before, it is also assumed that there is no additional loss between the horn aperture and the mm-wave terminations.

Table 5.1: Estimated in-band power on the feedline for various filter parameters, taking into account the filter transmission efficiency of 70%.

ν [GHz]	$\mathcal{R}$	P_{300K} [pW]	$\Delta P_{300-77K}$ [pW]
250	200	3.62	2.69
250	400	1.81	1.35
250	700	1.04	0.77
240	2	347.76	258.50

5.4.1 Termination Channels

The four resonators proximately coupled to the end of the mm-wave feedline are designed to act as a matched termination to minimize any reflections from the open end of the feedline, absorbing any radiation that is not accepted by the spectrometer channels. The volume of the inductor of the termination resonators is 3.58 times the spectrometer KID inductors, resulting in a reduction in the fractional frequency responsivity by the same factor.

Labelling the resonators in terms of the readout frequency, the elements that make up the termination section of the spectrometer, as viewed from the spectrometer input, are ordered as KID3, additional absorber, KID4, KID1, absorber, KID2. The additional absorber lengths are isolated and not coupled to a detector.

Fig. 5.12 shows results from a simulation of the fraction of absorbed power as a function of frequency relative to the power at the first detector in each terminator KID. An estimate for the total expected absorption ratios can by obtained by integrating over the 180-300 GHz band (dashed lines). However, an accurate estimate requires knowledge of the shape of optical passband. As a first order approximation, a flat-top passband can be assumed which results in simulated ratios of 0.16, 0.09, 0.06 and 0.02 in the order that the resonators are located along the feedline, respectively.

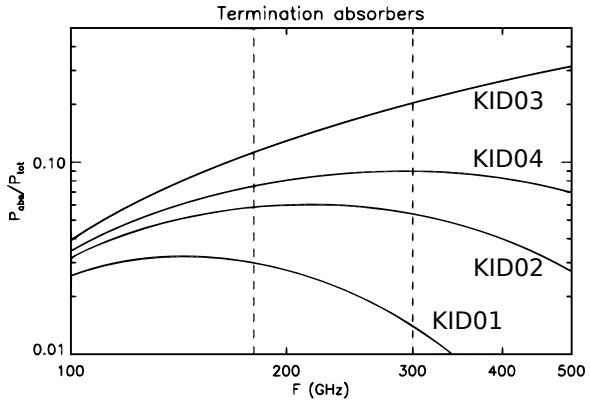

Figure 5.12: Simulation of the expected fraction of absorbed power in each of the four termination channels.

5.4.2 Measured Response

The measured response to a change in optical load for each resonator is shown in Fig. 5.13a. The four lowest frequency points are the termination resonators and show consistent response according to the position on the feedline. A comparison of the measured to simulated response is shown in Fig 5.13b. The simulated values are calculated using the integrated absorption estimate from Fig. 5.12, for both a constant power dependence corresponding to the low-power region of the responsivity curve, as well as the $P^{1/2}$ dependence at high powers (cf. Fig. 5.14). While it is observed that the data agree with the low power responsivity estimate pretty well, we must be mindful of the various assumptions implicit in the simulation data.

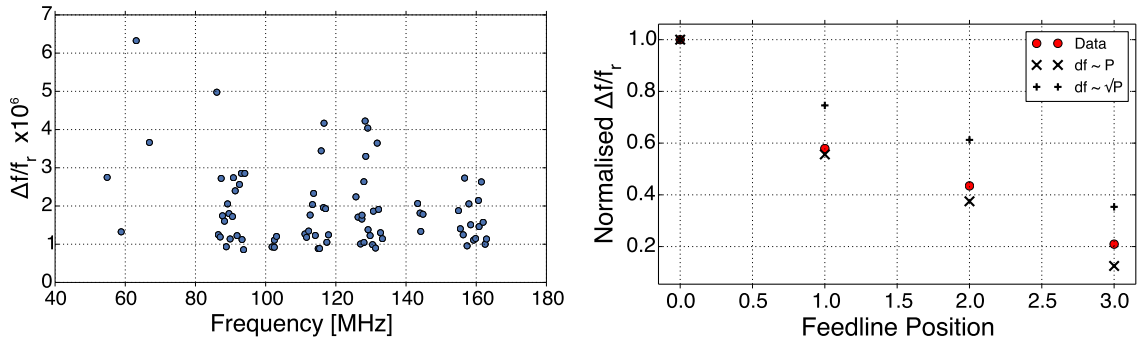

(a) (b)

Figure 5.13: a) Measured shift in resonant frequency between 300 K and 77 K blackbody loads. The four points at low resonant frequency are the termination absorbers. **b** Comparison of the measured to simulated normalised response of the four termination KIDs.

The response of the remaining spectrometer channels ranges between $(1-5)\times 10^{-6}$. The variation in response is consistent with the spectral bandwidth of each filter. The

apparent lower limit could be an indication of a common response between filter channels. On the other hand, such a feature could also suggest a limiting loss mechanism that limits the bandwidth of the filter, which was confirmed in the spectral data.

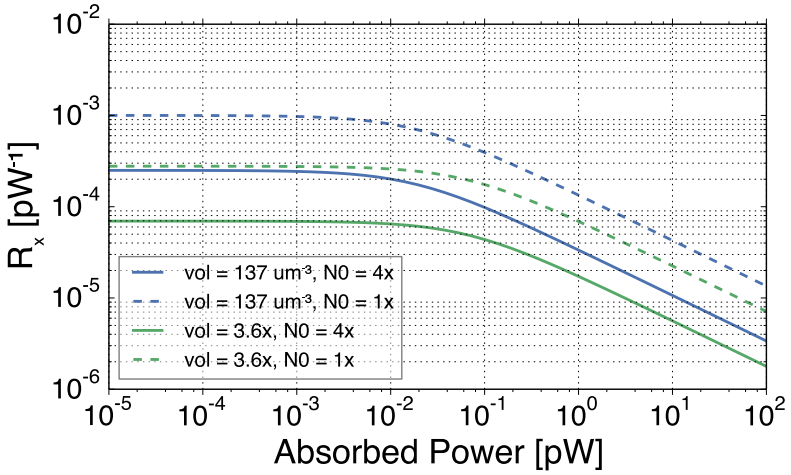

Figure 5.14: Expected responsivity prediction from the Mattis-Bardeen equations for both the spectrometer ($V_L = V_0 = 137\,\mu\text{m}$) and terminator resonators ($V_L = 3.85V_0$)

We now compare the measured response with a calculated expected response. A plot of the calculated responsivity derived assuming a Mattis-Bardeen conductivity is shown in Fig. 5.14. The two colours correspond to the different inductor volumes; $V_L = 137$ μm for the spectrometer resonators, and $V_L = 490$ μm for the terminator resonators. The solid lines are estimates using an experimentally determined value for the single-spin density of states, $N_0 = 3.5 \times 10^8\,\text{eV}^{-1}\mu\text{m}^{-3}$ (Gao et al. 2012), that is approximately a factor of 4 larger than the theoretical value (Dridi et al. 2002).

An estimate of the power incident on the feedline may be made using Eq. 5.20. The filter bandwidth is estimated using measured values of Q_{filt} and ν_0 the spectral measurements presented in Sec. 5.3.2. The response is then calculated from Fig. 5.14 and compared with the measured response. Estimates for a number of resonators that are confidently identified with their design value are given in Table 5.2. Again, we assume a correction for the absorption efficiency of a mismatched filter channel based on the design values of Q_{filt}. The main result is that we consistently measure a diminished response relative to the Mattis-Bardeen prediction.

This reduced response has been observed over a number of devices measured at both Caltech and Cardiff. A large number of assumptions have been made in the calculations in Table 5.2 and so the absolute value of the ratio could be off by a significant fraction. For example we have assumed the larger value of N_0 measured by (Gao et al. 2012). If instead the we use the value originally quoted (Leduc et al. 2010) then the responsivity

Table 5.2: Comparison of observed and expected response to a change in blackbody load.

f_r (MHz)	ν_0 (GHz)	$Q_{\mathrm{filt,meas}}$	$Q_{\mathrm{filt,des}}$	$\eta_{A\Omega}$	ΔP_{est} (pW)	$\Delta f_{\mathrm{meas}}/f_r$ ($\times 10^{-6}$)	$\Delta f_{\mathrm{calc}}/f_r$ ($\times 10^{-6}$)	$\Delta f_{\mathrm{calc}}/\Delta f_{\mathrm{meas}}$
87.7	256.5	300.0	293.8	1.0	0.941	1.744	32.432	18.60
91.3	222.2	300.0	278.1	1.0	0.861	2.397	31.006	12.94
93.3	192.6	547.8	546.9	0.8	0.289	1.122	17.618	15.71
86.5	256.9	547.8	546.3	1.0	0.507	1.249	23.613	18.90
102.5	240.5	1000.0	650.3	1.0	0.399	0.921	20.844	22.64
116.6	214.3	300.0	287.1	0.9	0.759	4.166	29.072	6.98

prediction is given by the dashed curves in Fig. 5.14 and results in an increase in responsivity, increasing the discrepancy.

It is possible that the diminished response is some combination of the untested horn coupling scheme and the anomalous response of TiN. An independent measurement to rule out any potential issues with the optical coupling onto the spectrometer feedline should be straightforward and enlightening. In fact, recent experiments carried out by the SuperSpec collaboration on a new set of devices that have exchanged the horn coupling scheme for a planar twin-slot antenna still show a diminished response relative to the prediction, possibly vindicating the waveguide coupling design. To further test the anomalous response of the TiN will require a systematic material study that is beyond the scope of this thesis.

As a final step, we use the measured responsivity to estimate a value for the optical NEP, which may be calculated from

$$\mathrm{NEP} = \frac{\sqrt{S_x}}{R_x} = \sqrt{S_x}\frac{\Delta P}{\Delta f/f_r}, \tag{5.22}$$

where S_x is the power spectral density of the fractional frequency fluctuations. For the $Q_{\mathrm{filt}} = 300$ channels given in Table 5.2, the $\Delta f/f_r/\Delta P \approx 1 - 3 \times 10^{-6}\,\mathrm{W}^{-1}$. From Chapter 4 typical noise at low frequency values for a detector driven just below bifurcation are around $S_x \approx 2 \times 10^{-17}$. Therefore we estimate a full system optical NEP of between $(1-3) \times 10^{-15}\,\mathrm{WHz}^{-1/2}$.

5.5 Conclusion

We have demonstrated the concept of a planar superconducting filterbank operating at 250 GHz through spectral characterisation using an FTS. The filter profiles are well

described by a Lorentzian lineshape and indicate excellent spectral purity with out of band response suppressed down to the 1% level. A comparison of the measured parameters extracted from fits to the interferogram to the design parameters indicate a limiting internal loss that is mostly like due to the SiN microstrip dielectric layer. The loss we measure is in close agreement with independent measurements of the loss tangent of SiN under similar operating conditions. Furthermore, we observe a significant amount of scatter in the filter positions when compared to the design, which is likely due to uncertainties in the lithography. This is an issue that needs to be solved as for a working instrument, it is imperative to be able to predict and set the filter positions accurately. To that end, in order to determine whether this filter-bank design is a viable option for future on-chip spectrometer instruments, further investigation is required to determine whether the lithographic uncertainties can be controlled to the required level.

Chapter 6

Summary and Future Work

In collaboration with the California Institute of Technology and the Jet Propulsion Laboratory, we have designed, fabricated and characterised a novel prototype on-chip spectrometer intended for mm-wave astronomy. Whilst the emphasis of this thesis has been placed on astronomical applications, the dramatic reduction in size and cost of such a spectrometer will have a significant impact on any application that requires low-medium resolution spectroscopy.

We have successfully demonstrated a superconducting filter-bank operating at 300 GHz, which employs an inverted superconducting niobium/silicon nitride thin-film microstrip architecture to simultaneously provide both low loss transmission whilst retaining a high level of stray light control. The filter-bank itself comprises a number of narrowband, resonant filters, ordered in decreasing frequency along the main feedline. The output of each filter couples into a kinetic inductance detector that provides a measure of the total power contained in each channel. The spectral resolution and corresponding detector count of such a spectrometer is determined by the quality factor of each resonant filter, which ultimately will be limited by the losses in the microstrip dielectric layer

Characterisation of the filter-bank was carried out using a polarising FTS coupled to a smooth-walled multi-angle horn at the spectrometer input. We measure a number of filter profiles with excellent spectral purity with -20 dB out of band rejection (cf. Fig. 6.1a). A number of filters with quality factors above 600 have also been measured placing a lower limit on the dielectric loss, which already fulfils the requirement for medium-resolution spectroscopic applications. The right panel of Fig. 6.1b compares the measured and designed quality factor for a selection of filters, demonstrating a clear limiting loss mechanism expected from the dielectric layer. To determine whether the source of this loss is due to the mm-wave loss of the SiN layer or the limited frequency

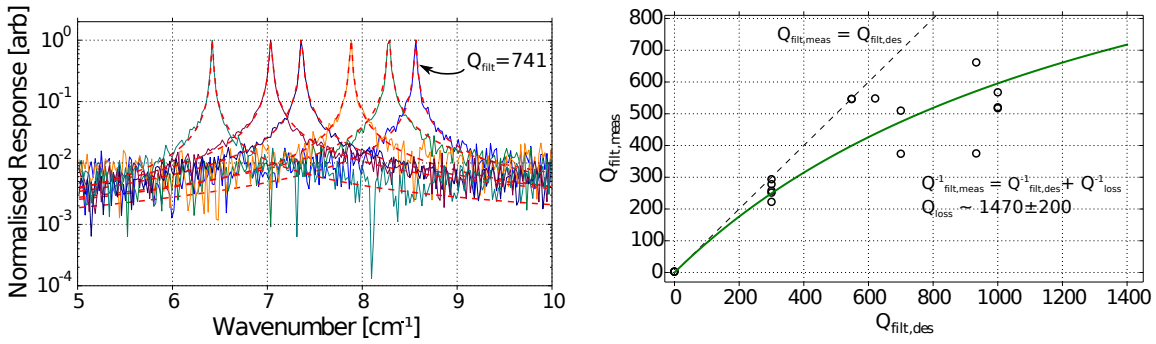

(a) (b)

Figure 6.1: a) A selection of filter profiles. b) Comparison of measured and design filter quality factors.

resolution the FTS, further work will be required using either a longer travel FTS, or a mm-wave frequency controllable swept source.

A number of open questions that need to be addressed in future design iterations. Arguably, the most important is whether the fabrication tolerances can be controlled to a level in the filter locations can be placed with a high level accuracy and reproducibility. As demonstrated in Chapter 5 in the current device there is significant scatter in the extracted placement of the measured filter positions. To be realistically viable as a future instrument, the filter positions have to be predictable to a level commensurate with the inverse of the spectrometer resolution. Therefore for $\mathcal{R} = 1000$, tolerances on the filter placement are at least on the order of 0.1% of the filter central frequency. To achieve this for a filter length of 200 μm, corresponds to a physical length change of ≈ 20 nm from the designed value. This is an extremely tight tolerance requirement for the photolithography and based on the evidence from Chapter 5, further work is required. Assuming that the current limiting maximum resolution of the spectrometer of approximately 700 is due to the SiN layer, this value is sufficient for low resolution work, but to extend the technology to operate at $\mathcal{R} = 1000$, alternative materials might have to be investigated. There are a number options that we plan to explore in future design iterations, such as using the device layer of a SOI wafer as a replacement for the amorphous dielectric layer. This thin crystalline Si layer should be very low loss, and with a few modifications of the fabrication process flow, could potentially provide significant performance improvements.

We also presented a thorough characterisation of the TiN resonators. From the data presented in Chapter 4, as well as from a number of groups measurements on TiN, it is clear that the Mattis-Bardeen theory that successfully predicts the performance of aluminium resonators, is insufficient for TiN. To investigate this further, a full

systematic study of TiN for a range of device parameters is required. Work is planned to investigate these properties at lower base temperatures once our cryostat undergoes the planned upgrades. If a theory is devised that is able to accurately predict the detector performance, then TiN resonators have an extremely bright future for use in KIDs.

Bibliography

Abbosh, A M (2009). "Analytical closed-form solutions for different configurations of parallel-coupled microstrip lines". English. *IET Microwaves, Antennas & Propagation* 3.1, p. 137. DOI: 10.1049/iet-map:20070308 (p. 46).

Ade, PAR et al. (1999). "An absolute dual beam emission spectrometer". *Optical Society of America* (p. 12).

Bardeen, J. et al. (1957). "Theory of Superconductivity". *Physical Review* 108.5, pp. 1175–1204. DOI: 10.1103/PhysRev.108.1175 (pp. 17, 19).

Barends, R et al. (2008). "Contribution of dielectrics to frequency and noise of NbTiN superconducting resonators". English. *Applied Physics Letters* 92.22, p. 223502. DOI: 10.1063/1.2937837 (p. 65).

Barends, R et al. (2009). "Enhancement of quasiparticle recombination in Ta and Al superconductors by implantation of magnetic and nonmagnetic atoms". *Physical Review B* 79.2, p. 020509 (p. 39).

Barends, R et al. (2011). "Minimizing quasiparticle generation from stray infrared light in superconducting quantum circuits". *Applied Physics Letters* 99.11, pp. 113507–113507–3 (p. 25).

Barends, Rami (2009). "Photon-detecting superconducting resonators". PhD thesis. TU Delft (p. 20).

Barry, P. S. et al. (2012). "Electromagnetic design for SuperSpec: a lithographically-patterned millimetre-wave spectrograph". *Proceedings of SPIE* 8452. DOI: 10.1117/12.927089 (p. 13).

Baselmans, Jochem et al. (2012). "Ultra Low Background Cryogenic Test Facility for Far-Infrared Radiation Detectors". English. *Journal of Low Temperature Physics* 167.3-4, pp. 360–366. DOI: 10.1007/s10909-012-0511-0 (pp. 25, 61).

Bin, M. et al. (1999). "A large throughput high resolution Fourier transform spectrometer for submillimeter applications". *International Journal of Infrared and Millimeter Waves* 20.3, pp. 383–400 (p. 89).

Boyd, Robert W (1982). "Photon bunching and the photon-noise-limited performance of infrared detectors". English. *Infrared Physics* 22.3, pp. 157–162. DOI: 10.1016/0020-0891(82)90034-3 (p. 27).

Bradford, C. M. et al. (2004). "Z-Spec: a broadband millimeter-wave grating spectrometer: design, construction, and first cryogenic measurements". *Proceedings of SPIE* 5498, pp. 257–267 (p. 12).

Bradford, C. M. et al. (2009). "Survey Spectroscopy in the Submillimeter and Millimeter, from the CSO to CCAT". *Submillimeter Astrophysics and Technology: a Symposium Honoring Thomas G. Phillips ASP Conference Series* 417, p. 341 (p. 12).

Bradford, C. Matt et al. (2002). "WaFIRS, a Waveguide Far-IR Spectrometer for Space-Borne Astrophysics". English. *Far-IR, Sub-mm & MM Detector Technology Workshop* -1, p. 60 (p. 12).

Bueno, J et al. (2014). "Anomalous response of superconducting titanium nitride resonators to terahertz radiation". *arXiv.org*, p. 270. arXiv: 1408.0270 [cond-mat.supr-con] (p. 24).

Chambers, R G (1952). "The Anomalous Skin Effect". English. *Proceedings of the Royal Society A: Mathematical, Physical and Engineering Sciences* 215.1123, pp. 481–497. DOI: 10.1098/rspa.1952.0226 (p. 18).

Day, Peter K et al. (2003). "A broadband superconducting detector suitable for use in large arrays". *Nature* 425.6, pp. 817–821. DOI: 10.1038/nature02037 (pp. 5, 59).

Devlin, Mark J et al. (2004). "The balloon-borne large aperture submillimeter telescope (BLAST)", pp. 42–54 (p. 4).

Diener, P et al. (2012). "Design and Testing of Kinetic Inductance Detectors Made of Titanium Nitride". *Journal of Low Temperature Physics* 167, pp. 305–310. DOI: 10.1007/s10909-012-0484-z (pp. 18, 62).

Doyle, S et al. (2008). "Lumped Element Kinetic Inductance Detectors". English. *Journal of Low Temperature Physics* 151.1-2, pp. 530–536. DOI: 10.1007/s10909-007-9685-2 (p. 16).

Doyle, Simon (2008). "Lumped Element Kinetic Inductance Detectors". PhD thesis. Cardiff University (p. 16).

Doyle, Simon et al. (2007). "Lumped Element Kinetic Inductance Detectors". *Proceedings of the Eighteenth International Symposium on Space Terahertz Technology*, p. 170 (p. 41).

Dridi, Z et al. (2002). "First-principles calculations of vacancy effects on structural and electronic properties of TiC xand TiN x". English. *Journal of Physics: Condensed Matter* 14.43, pp. 10237–10249. DOI: 10.1088/0953-8984/14/43/320 (p. 97).

Dynes, RC et al. (1978). "Direct measurement of quasiparticle-lifetime broadening in a strong-coupled superconductor". *Physical Review Letters* 41.21, pp. 1509–1512 (p. 66).

Eales, S et al. (2009). "The Herschel ATLAS". *arXiv.org*. arXiv: 0910.4279v1 [astro-ph.CO] (p. 4).

Eom, B.H. et al. (2012). "A Wideband, Low-Noise Superconducting Amplifier with High Dynamic Range". *Arxiv preprint arXiv:1201.2392* (p. 5).

Escoffier, W et al. (2004). "Anomalous proximity effect in an inhomogeneous disordered superconductor". *Physical Review Letters* 93.21, p. 217005 (p. 66).

Faber, T E and A B Pippard (1955). "The penetration depth and high-frequency resistance of superconducting aluminium". *Proceedings of the Royal Society of London. Series A. Mathematical and Physical Sciences* 231.1186, pp. 336–353 (p. 19).

Ferkinhoff, Carl et al. (2010). "ZEUS-2: a second generation submillimeter grating spectrometer for exploring distant galaxies". *Arxiv preprint arXiv:1010.1439* astro-ph.IM. DOI: 10.1117/12.857018 (p. 12).

Gao, J et al. (2008a). "Equivalence of the Effects on the Complex Conductivity of Superconductor due to Temperature Change and External Pair Breaking". English. *Journal of Low Temperature Physics* 151.1-2, pp. 557–563. DOI: 10.1007/s10909-007-9688-z (p. 20).

Gao, J et al. (2012). "A titanium-nitride near-infrared kinetic inductance photon-counting detector and its anomalous electrodynamics". *arXiv.org*. arXiv: 1208.0871v1 [cond-mat.supr-con] (pp. 62, 65, 97).

Gao, Jiansong (2008). "The Physics of Superconducting Microwave Resonators". PhD thesis. California Institute of Technology (pp. 16, 20, 25, 26, 34, 38, 61, 69).

Gao, Jiansong et al. (2008b). "A semiempirical model for two-level system noise in superconducting microresonators". English. *Applied Physics Letters* 92.21, p. 212504. DOI: 10.1063/1.2937855 (pp. 37, 38).

Gao, Jiansong et al. (2009). "Measurement of loss in superconducting microstrip at millimeter-wave frequencies". *The Thirteenth International Workshop on Low Temperature Detectors*. California Institute of Technology, pp. 164–167. DOI: 10.1063/1.3292306 (p. 5).

Göppl, M et al. (2008). "Coplanar Waveguide Resonators for Circuit Quantum Electrodynamics". *arXiv.org*. DOI: 10.1063/1.3010859. arXiv: 0807.4094v1 [cond-mat.supr-con] (p. 5).

Graaf, S E de (2014). "Fractal superconducting resonators for the interrogation of two-level systems". PhD thesis. Chalmers University of Technology (p. 5).

Griffin, M. et al. (2006). "Herschel-SPIRE: design, performance, and scientific capabilities". *Space Telescopes and Instrumentation I: Optical, Infrared, and Millimeter (this volume)* 6265 (p. 4).

Gundlach, K H and M Schicke (2000). "SIS and bolometer mixers for terahertz frequencies". *Superconductor Science and Technology* 13.1, p. 171. DOI: 10.1088/0953-2048/13/12/202 (p. 8).

Hailey-Dunsheath, S. and E. Shirokoff (2014). "Status of SuperSpec: a broadband, on-chip millimeter-wave spectrometer". *SPIE ...* (P. 94).

Hailey-Dunsheath, S. et al. (2008). "Detection of the 13CO $J = 6 \rightarrow 5$ transition in the Starburst Galaxy NGC 253". English. *The Astrophysical Journal* 689.2, pp. L109–L112. DOI: 10.1086/595840 (p. 11).

Hailey-Dunsheath, S. et al. (2014). "Optical Measurements of SuperSpec: A Millimeter-Wave On-Chip Spectrometer". *Journal of Low Temperature Physics*, p. 80. DOI: 10.1007/s10909-013-1068-2 (pp. 14, 93).

Hailey-Dunsheath, Steven (2009). "Probing star formation at low and high redshift with ZEUS, a new submillimeter grating spectrometer". PhD thesis. Cornell University (p. 11).

Harrison, George (1949). "The Production of Diffraction Gratings: II The Design of Echelle Gratings and Spectrographs". English. *Journal of the Optical Society of America* 39.7, pp. 522–527. DOI: 10.1364/JOSA.39.000522 (p. 11).

Isaak, K et al. (1998). "WASP: A Wideband Analogue Autocorrelation SPectrometer". 30, p. 756 (p. 9).

Janssen, R M J et al. (2013). "High optical efficiency and photon noise limited sensitivity of microwave kinetic inductance detectors using phase readout". *Applied Physics Letters* 103.2, p. 3503. DOI: 10.1063/1.4829657 (p. 24).

Kaplan, S et al. (1976). "Quasiparticle and phonon lifetimes in superconductors". English. *Physical Review B* 14.11, pp. 4854–4873. DOI: 10.1103/PhysRevB.14.4854 (p. 23).

Kooi, JW et al. (2003). "A full-height waveguide to thin-film microstrip transition with exceptional RF bandwidth and coupling efficiency". *International Journal of Infrared and Millimeter Waves* 24.3, pp. 261–284 (p. 50).

Kovacs, Attila et al. (2012). "SuperSpec: design concept and circuit simulations". *Proceedings of SPIE* 8452. DOI: 10.1117/12.927160 (p. 53).

Lambert, D K and P L Richards (1978). "Martin-Puplett interferometer: an analysis". English. *Applied Optics* 17.10, p. 1595. DOI: 10.1364/AO.17.001595 (p. 85).

Leduc, Henry G. et al. (2010). "Titanium nitride films for ultrasensitive microresonator detectors". *Applied Physics Letters* 97.1, p. 2509. DOI: 10.1063/1.3480420 (pp. 47, 61, 71, 97).

Leech, J. et al. (2011). "Multiple flare-angle horn feeds for sub-mm astronomy and cosmic microwave background experiments". *Astronomy and Astrophysics* 532, A61. DOI: 10.1051/0004-6361/201117124 (p. 49).

Lupu, R E et al. (2012). "Measurements of CO redshifts with Z-Spec for lensed submillimeter galaxies discovered in the H-ATLAS survey". *The Astrophysical Journal* 757.2, p. 135 (p. 12).

Martin, D. H. and E Puplett (1970). "Polarised interferometric spectrometry for the millimetre and submillimetre spectrum". English. *Infrared Physics* 10.2, pp. 105–109. DOI: 10.1016/0020-0891(70)90006-0 (p. 85).

Matick, Richard E (2000). *Transmission Lines and Communication Networks*. English. An Introduction to Transmission Lines, High-frequency and High-speed Pulse Characteristics and Applications. Wiley-IEEE Press. ISBN: 9780780360433 (p. 22).

Mattis, D.C. and J. Bardeen (1958). "Theory of the anomalous skin effect in normal and superconducting metals". *Physical Review* 111.2, p. 412 (p. 19).

Mauskopf, P. D. et al. (2014). "Photon-Noise Limited Performance in Aluminum LEKIDs". *Journal of Low Temperature Physics*, p. 29. DOI: 10.1007/s10909-013-1069-1 (pp. 24, 39, 69, 71).

Mauskopf, PD et al. (1997). "Composite infrared bolometers with Si_3N_4 micromesh absorbers". *Applied Optics* 36.4, pp. 765–771 (p. 7).

Mazin, Benjamin A (2004). "Microwave kinetic inductance detectors". PhD thesis. California Institute of Technology. ISBN: 0496944924 (p. 16).

Mazin, Benjamin A et al. (2002). "Superconducting Kinetic Inductance Photon Detectors". *SPIE ...* California Institute of Technology, USA, pp. 283–293. DOI: 10.1117/12.460456 (p. 5).

McKenney, Christopher M et al. (2012). "Design considerations for a background limited 350 micron pixel array using lumped element superconducting microresonators", 84520S–84520S–10 (pp. 16, 48, 61).

Monfardini, A. et al. (2010). "NIKA: A millimeter-wave kinetic inductance camera". *arXiv.org*. DOI: 10.1051/0004-6361/201014727. arXiv: 1004.2209v2 [astro-ph.IM] (p. 16).

Mutus, J Y et al. (2013). "Design and characterization of a lumped element single-ended superconducting microwave parametric amplifier with on-chip flux bias line". *Applied Physics Letters* 103.1, p. 2602. DOI: 10.1063/1.4821136 (p. 5).

Naylor, Bret J (2008). "Broadband millimeter-wave spectroscopy with Z-Spec: an unbiased molecular-line survey of the starburst galaxy M82". PhD thesis. Pasadena: California Institute of Technology (p. 12).

Naylor, David A et al. (1994). "A polarizing Fourier transform spectrometer for astronomical spectroscopy at submillimeter and mid-infrared wavelengths". English. *Instrumentation in Astronomy VIII* 2198, pp. 703–714 (p. 85).

Neill, C et al. (2013). "Fluctuations from edge defects in superconducting resonators". *Applied Physics Letters* 103.7, p. 2601. DOI: 10.1063/1.4818710 (p. 38).

Nikola, Tomas et al. (2003). "ZEUS: A Submillimeter Grating Spectrometer for Exploring Distant Galaxies". *Astronomical Telescopes and Instrumentation*. Ed. by Thomas G. Phillips and Jonas Zmuidzinas. SPIE, pp. 88–99. DOI: 10.1117/12.459371 (p. 11).

Noroozian, O. et al. (2012). "Crosstalk reduction for superconducting microwave resonator arrays". *IEEE Transactions ...* (Pp. 16, 48).

O'Connell, Aaron D et al. (2008). "Microwave dielectric loss at single photon energies and millikelvin temperatures". English. *Applied Physics Letters* 92.11, p. 112903. DOI: 10.1063/1.2898887 (p. 93).

Pascale, E et al. (2008). "The Balloon-borne large aperture submillimeter telescope: BLAST". *The Astrophysical Journal* 681, p. 400 (p. 4).

Pauw, LJ Van der (1977). "The radiation of electromagnetic power by microstrip configurations". *Microwave Theory and Techniques, IEEE Transactions on* 25.9, pp. 719–725 (p. 45).

Pippard, A B (1953). "An Experimental and Theoretical Study of the Relation between Magnetic Field and Current in a Superconductor". English. *Proceedings of the Royal Society A: Mathematical, Physical and Engineering Sciences* 216.1127, pp. 547–568. DOI: 10.1098/rspa.1953.0040 (p. 18).

Porch, A et al. (2005). "Calculation of the Characteristics of Coplanar Resonators for Kinetic Inductance Detectors". English. *Applied Superconductivity, IEEE Transactions on* 15.2, pp. 552–555. DOI: 10.1109/TASC.2005.849916 (p. 33).

Potter, PD (1963). "A new horn antenna with suppressed sidelobes and equal beamwidths" (p. 50).

Pozar, David M (2011). *Microwave Engineering*. English. John Wiley & Sons. ISBN: 1118213637 (pp. 28–30).

Reuter, GEH and E H Sondheimer (1948). "The theory of the anomalous skin effect in metals". *Proceedings of the Royal Society of London. Series A. Mathematical and Physical Sciences* 195.1042, pp. 336–364 (p. 18).

Rothwarf, Allen and BN Taylor (1967). "Measurement of recombination lifetimes in superconductors". *Physical Review Letters* 19, pp. 27–30 (p. 27).

Shirokoff, E. et al. (2012). "MKID development for SuperSpec: an on-chip, mm-wave, filter-bank spectrometer". *Proceedings of SPIE* 8452. DOI: 10.1117/12.927070 (p. 13).

Shirokoff, E. et al. (2014). "Design and Performance of SuperSpec: An On-Chip, KID-Based, mm-Wavelength Spectrometer". *Journal of Low Temperature Physics*, p. 96. DOI: 10.1007/s10909-014-1122-8 (pp. 14, 61).

Stacey, G. J. et al. (2007). "ZEUS: the Redshift (z) and Early Universe Spectrometer". *From Z-Machines to ALMA: (Sub)Millimeter Spectroscopy of Galaxies ASP Conference Series* 375, p. 52 (p. 11).

Swenson, L. J. et al. (2013). "Operation of a titanium nitride superconducting microresonator detector in the nonlinear regime". English. *Journal of Applied Physics* 113.10, p. 104501. DOI: 10.1063/1.4794808 (pp. 32, 66, 67, 73).

Swenson, Loren J et al. (2012). "MAKO: a pathfinder instrument for on-sky demonstration of low-cost 350 micron imaging arrays". *Millimeter* 8452. DOI: 10.1117/12.926223 (pp. 16, 48, 63).

Tauber, Jan A and Neal R Erickson (1991). "A low-cost filterbank spectrometer for submm observations in radio astronomy". English. *Review of Scientific Instruments* 62.5, p. 1288. DOI: 10.1063/1.1142487 (p. 9).

Tinkham, Michael (2012). *Introduction to Superconductivity*. English. Second Edition. Courier Dover Publications. ISBN: 9780486134727 (p. 32).

Visser, P J de (2014). "Quasiparticle dynamics in aluminium superconducting microwave resonators". PhD thesis. Kavli Institute of Nanoscience Delft (p. 21).

Visser, P J de et al. (2010). "Readout-power heating and hysteretic switching between thermal quasiparticle states in kinetic inductance detectors". English. *Journal of Applied Physics* 108.11, p. 114504. DOI: 10.1063/1.3517152 (p. 32).

Visser, P J de et al. (2012a). "Generation-Recombination Noise: The Fundamental Sensitivity Limit for Kinetic Inductance Detectors". English. *Journal of Low Temperature Physics* 167.3-4, pp. 335–340. DOI: 10.1007/s10909-012-0519-5 (p. 39).

Visser, P J de et al. (2012b). "Microwave-induced excess quasiparticles in superconducting resonators measured through correlated conductivity fluctuations". English. *Applied Physics Letters* 100.16, p. 162601. DOI: 10.1063/1.4704151 (p. 27).

Visser, P J de et al. (2013). "Nonlinear electrodynamics of a superconductor due to the redistribution of quasiparticles". *arXiv.org*. arXiv: 1306.4992v1 [cond-mat.supr-con] (p. 24).

Vissers, Michael R. et al. (2013a). "Characterization and in-situ monitoring of substoichiometric adjustable superconducting critical temperature titanium nitride growth". *Thin Solid Films* 548, pp. 485–488 (p. 62).

Vissers, Michael R. et al. (2013b). "Proximity-coupled Ti/TiN multilayers for use in kinetic inductance detectors". *Applied Physics Letters* 102.2, p. 2603. DOI: 10.1063/1.4804286 (p. 63).

Wilson, CM and DE Prober (2004). "Quasiparticle number fluctuations in superconductors". *Physical Review B* 69.9, p. 094524 (pp. 24, 26, 27).

Wylde, R. J. (1984). "Millimetre-wave Gaussian beam-mode optics and corrugated feed horns". *IEE Proceedings*. Queen Mary College, London, England, pp. 258–262 (p. 49).

Zmuidzinas, J. (2012). "Superconducting Microresonators: Physics and Applications". *Annual Review of Condensed Matter Physics* (pp. 16, 22, 25, 26, 34, 36, 40, 48).

Zmuidzinas, J. and P L Richards (2004). "Superconducting detectors and mixers for millimeter and submillimeter astrophysics". *Proceedings of the IEEE* 92.10, pp. 1597–1616 (pp. 9, 12).

Zmuidzinas, Jonas (2011). *MKIDs for Superspec: Design Considerations*. Tech. rep. (pp. 46, 48).

Zmuidzinas, Jonas et al. (1998). "Development of SIS mixers for 1 THz". *Proc. SPIE Vol. 3357* 3357, pp. 53–62. DOI: 10.1117/12.317386 (p. 7).